The role of fibroblast growth factor receptor 2b signalling on distal epithelium during embryonic and pseudoglandular stage murine lung development

Inaugural Dissertation

submitted to the

Faculty of Medicine

in partial fulfillment of the requirements

for the PhD-Degree

of the Faculties of Veterinary Medicine and Medicine

of the Justus Liebig University Giessen

by

Matthew Robert Jones

of

Wolfville, Nova Scotia, Canada

Giessen 2023

From the Department of Internal Medicine and the Cardio-Pulmonary Institute (CPI)

Director: Prof. Dr. Werner Seeger

Faculty of Medicine of the Justus Liebig University Giessen

First Supervisor and Committee Member: Prof. Dr. Saverio Bellusci

Co-Supervisor and Committee Member: Prof. Dr. Reinhard Dammann

Committee Member: Prof. Dr. Dagmar Iber

Date of Doctoral Defense: 27.06.2023

Declaration

"I declare that I have completed this dissertation single-handedly without the unauthorized help of a second party and only with the assistance acknowledged therein. I have appropriately acknowledged and referenced all text passages that are derived literally from or are based on the content of published or unpublished work of others, and all information that relates to verbal communications. I have abided by the principles of good scientific conduct laid down in the charter of the Justus Liebig University of Giessen in carrying out the investigations described in the dissertation."

_____

Matthew Robert Jones

For Mom and Dad

Table of contents

List of figures

List of figures

List of tables

List of abbreviations and acronyms

AB	Acidic box
ADI	Airway differentiation intermediate cell
AEC	Alveolar epithelial cell
AER	Apical ectodermal ridge
Ager	Advanced glycosylation end-product specific receptor
AKT (PKB)	Protein kinase B
APC	Allophycocyanin
Aqp5	Aquaporin 5
aRNA	Antisense RNA
ASMC	Airway smooth muscle cell
AT1	Alveolar cell type 1
AT2	Alveolar cell type 2
BADJ	Bronchioalveolar duct junction
BASC	Bronchioalveolar stem cell
BLAST	Basic Local Alignment Search Tool
Bmp (member)	Bone morphogenic protein (member)
BP	Bipotential progenitor cell
BSA	Bovine serum albumin
caFgfr1	Constitutively active fibroblast growth factor receptor 1
cAMP	Cyclic adenosine monophosphate
CD (member)	Cluster of differentiation (member)
Cdc6	Cell division control 6
Cdh1	Cadherin-1
Cdk2	Cyclin dependent kinase
cDNA	Complementary DNA
C/EBP	CCAAT enhancer binding protein
Cgrp	Calcitonin gene-related peptide
CREB	cAMP response element binding protein

CreERT2	Cre recombinase (aka Causes recombination) fused to a triple mutant form of the human estrogen receptor
Ct	Threshold cycle
Ctnnb1	Beta-catenin
Cym	Chymosin
DAPI	4’,6-diamidino-2-phenylindole
DNA	Deoxyribonucleic acid
Dox	Doxycycline
E	Embryonic day
ECM	Extracellular matrix
EdU	5-ethynyl-2´-deoxyuridine
Egf	Epidermal growth factor
Ep300	E1A binding protein P300
EpCAM	Epithelial cell adhesion molecule
Etv (member)	E twenty-six variant transcription factor (member)
FACS	Fluorescence-activated cell sorting
FCS	Fetal calf serum
Fgf (member)	Fibroblast growth factor (member)
Fgfr (member)	Fibroblast growth factor receptor (member)
Fgfr2b	Fibroblast growth factor receptor 2b
FIJI	(Fiji) is just ImageJ
FITC	Fluorescein isothiocyanate
Flox	Flanked by loxp
Fox (member)	Forkhead box protein (member)
GA	Glutaraldehyde
GEO	Gene Expression Omnibus
Gli1	Glioma-associated oncogene
GS	Goat serum
GTP	Guanosine triphosphate
GTPase	GTP-binding protein

Abbreviations and acronyms

HBSS	Hank's Balanced Salt Solution
Hhip	Hedgehog interacting protein
Hopx	Homeodomain-only protein
Hprt	Hypoxanthine-guanine phosphoribosyltransferase
HS	Heparan sulfate
HSBS	Heparan sulfate binding site
HSPG	Heparan sulfate proteoglycan
IAAP	Injury-activated alveolar progenitor
Id2	Inhibitor of DNA binding 2
IF	Immunofluorescence
Ig	Immunoglobulin
Il1r1	Interleukin 1 receptor type 1
IP	Intraperitoneal
KEGG	Kyoto Encyclopedia of Genes and Genomes
Ki67	Marker of proliferation Ki-67
knn graph	Nearest neighbour graph
Kras	Kirsten rat sarcoma
Krt8	Keratin 8
Lama1	Laminin subunit alpha-1
Lamp3	Lysosome-associated membrane glycoprotein 3
LogFC	Logarithmically transformed fold change
Loxp	Locus of X-over P1
MAPK	Mitogen-activated protein kinase
miR (member)	Micro ribonucleic acid (member)
mRNA	Messenger ribonucleic acid
n	Number of biological replicates
NE	Neuroendocrine cell
NECB	Neuroendocrine cell body
Nkx2-1	NK2 homeobox 1
p63	Tumor protein 63

Abbreviations and acronyms

PBS	Phosphate-buffered saline
PBST	Phosphate-buffered saline with Tween
PCA	Principal component analysis
PCR	Polymerase chain reaction
Pd-l1	Programmed death-ligand 1
Pdpn (T1α)	Podoplanin
PFA	Paraformaldehyde
pH	Potential of hydrogen
PI3K	Phosphoinositide 3-kinase
PIPES	Piperazin-N,N'-bis-(2-ethansulfonsäure)
PKC	Protein kinase C
PLCY	Phospholipase C Gamma
PN	Postnatal day
preAT1	Alveolar cell type 1 precursor
preAT2	Alveolar cell type 2 precursor
Ptch2	Patched 2
RAS	Rat sarcoma
rFGF10	Recombinant fibroblast growth factor 10
RFP	Red fluorescent protein
RNA	Ribonucleic acid
Rosa26	Reverse orientation splice acceptor 26
rpm	Revolutions per minute
RT-qPCR	Reverse transcription quantitative real-time polymerase chain reaction
RTK	Receptor tyrosine kinase
rtTA	Reverse tetracycline transactivator
SCANPY	Single-Cell Analysis in Python
Scgb1a1	Secretoglobin Family 1A Member 1
scRNA-seq	Single-cell RNA-sequencing
SEM	Standard error of the mean
sFGFR2b	Soluble fibroblast growth factor receptor 2b

Sftp (member)	Surfactant protein (member)
Shh	Sonic hedgehog
SMM	Submesothelial mesenchyme
Smo	Smoothened
Sox2	Sex determining region Y-box transcription factor 2
Sox9	Sex determining region Y-box transcription factor 9
SPF	Specific-pathogen-free
Tam	Tamoxifen
Tcf21	Transcription factor 21
tdTomato	Tandem dimer tomato
TEM	Transmission electron microscopy
Tet(o)	Tet-operator
Tg	Transgene
Tgf-β	Transforming growth factor beta
TK	Tyrosine kinase domain
TM	Transmembrane domain
tRNA	Transfer RNA
tSNE	t-distributed stochastic neighbor embedding
TUNEL	TdT-mediated dUTP Nick-End Labeling
UMAP	Uniform Manifold Approximation and Projection
Vegf	Vascular endothelial growth factor
Wnt (member)	Wingless-related integration site (member)
WT	Wildtype

1 Introduction

1.1 The mammalian lung: a marvel of form and function

Life must balance the exchange of resources and waste with the environment. As organisms arose of increasing size and complexity, most species evolved highly specialized organs as solutions to the common problem of efficient resource exchange and distribution. Kidneys, salivary and lacrimal glands, nerve networks, vasculature, mammary glands, pancreases, and lungs are prime examples of organs which form by a common principle of branching morphogenesis to maximize their surface area to volume ratio. Here, cells and organ tissues undergo multiple iterations of branch specification, elongation and bifurcation to form arborized scaffolds supporting the functional units of resource exchange (Ochoa-Espinosa and Affolter, 2012; Spurlin and Nelson, 2017).

In biological evolution, form follows function, and the mammalian lung is a prime example. In humans, the adult lung is composed of around 17 million airway branches supporting in the range of half a billion alveoli, each of which is highly partitioned and lined with extremely thin gas exchange cells. The delicacy of these structures would consign them to destruction during normal respiration if it weren't for surfactant, which is produced from another specialized alveolar cell, and which serves as a lubricant to decrease the surface tension of the alveolus. Finally, blood circulation and gas exchange are facilitated by a network of arterial and venous trees composed of over 250 000 arterioles and an intricate network of capillaries surrounding each alveolus. This entire structure has a surface area estimated in the range of 70 m^2 to 130 m^2, yet occupies a volume of roughly 5-6 litres, which is equivalent to packing a standard piece of paper into a thimble (Liem, 1988; Glenny, 2011).

Remarkably, the intricate development of the lung appears to be controlled by a relatively small set of molecular and biophysical mechanisms. These mechanisms include evolutionarily conserved molecular signalling pathways, functioning, albeit with species and organ-specific modifications, in a similar fashion throughout the living world. These pathways operate in conjunction with biophysical principles which can be mathematically modelled and computationally investigated. Integrating the biophysical rules to our biological understanding

of lung development has been a goal of recent research in the field (Iber and Menshykau, 2013; Lang et al., 2018). Take, for example, the regulation of branching morphogenesis on the differentiation of epithelial cells, and *vice versa*. On the one hand, morphogenesis establishes the geographic context regulating a multipotent progenitor's differentiation status and fate, while, on the other hand, the status of the different epithelial cell types partly drives the branching process. For instance, the transmural pressure exerted on airway epithelial cells from peristaltic airway smooth muscle contractions directs branch elongation, but only when coordinated with the signalling cross-talk between the distal epithelial cells and mesenchyme at the correct stage of embryonic development (Schittny et al., 2000; Bokka et al., 2015b; Nelson et al., 2017). If one of these factors is missing, misplaced, or mistimed, branching and subsequent cellular differentiation might be irreparably impacted.

1.2 Overview of murine lung development

Lung development in mice begins around embryonic day I 9.5. At this time, the anlage of the lower respiratory system evaginates from a region of foregut endoderm marked by *NK2 Homeobox 1* (*Nkx2-1*) expression. Two epithelial buds soon emerge, elongating and growing into the surrounding mesenchyme, which is bounded by a layer of mesothelium. These buds are composed of multipotent epithelial cells, which, through elaborate crosstalk with the mesenchyme, undergo airway branching morphogenesis and give rise to the different epithelial cell types of the mature lung (Fig. 1).

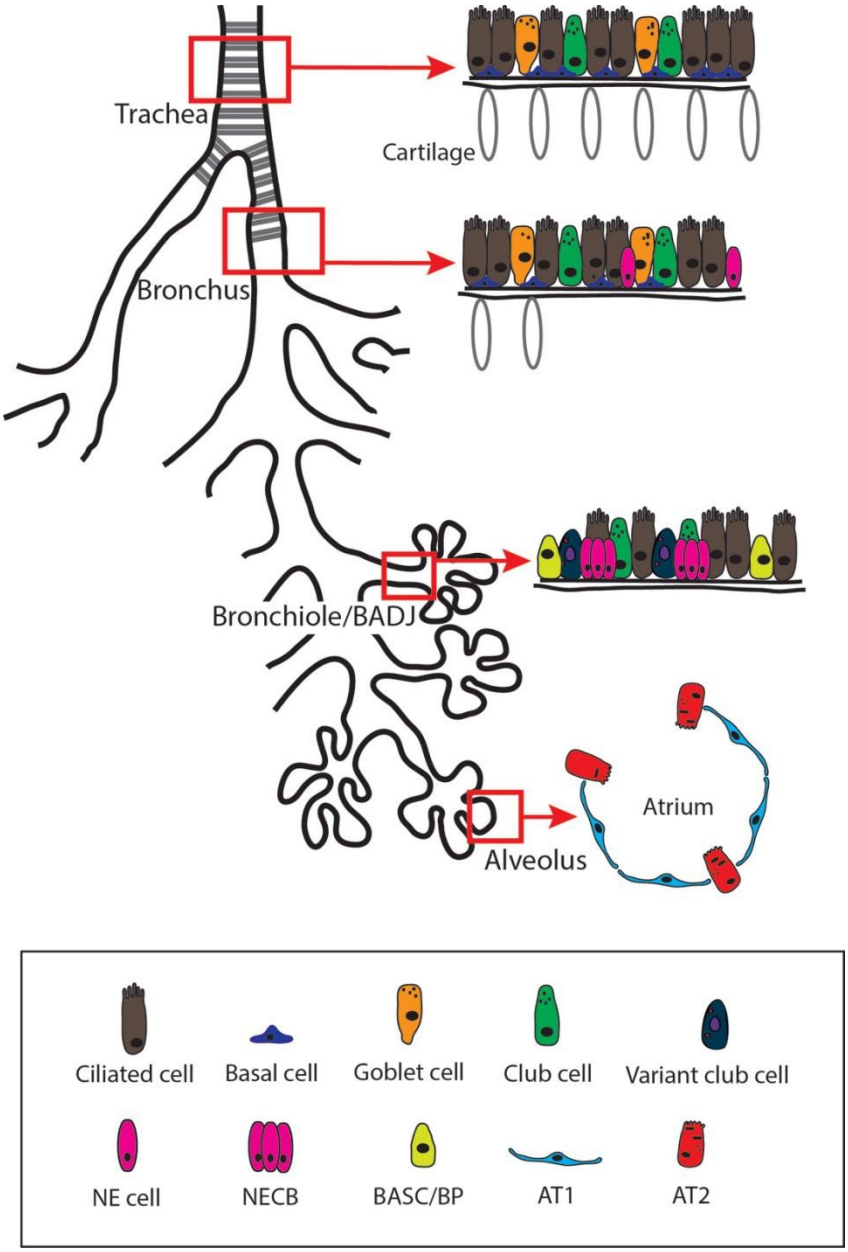

Figure 1 – Major epithelial cell types of a mature mouse lung. The simplified airway shows one of the two main bronchi stemming from the trachea. These upper airways are ringed with cartilage and are populated primarily by ciliated cells and basal cells, along with a smaller proportion of the secretory goblet and club cells. Bronchus epithelium also has a scattering of neuroendocrine (NE) cells. As airways narrow to the bronchioles, which join the distal-most alveolar sacs at the bronchioalveolar duct junction (BADJ), NE cells cluster together to form NE cell bodies (NECB). Here, variant club cells are found, as well as bronchioalveolar stem cells (BASC) and alveolar bipotential cells (BP). The terminal alveolar sacs contain the alveoli, which are predominantly composed of the thin gas exchange alveolar type 1 (AT1) and surfactant producing cuboidal alveolar type 2 (AT2) cells.

Lung organogenesis proceeds through a series of overlapping morphological stages: the embryonic stage (E9.5-E10.5), marked by the establishment of the primary conducting airways; the pseudoglandular stage (E10.5-E16.5), distinguished by airway branching morphogenesis; the canalicular stage (E16.5-E17.5), where distal acini emerge from differentiating alveolar cells and the production of surfactant begins; the saccular stage (E17.5-postnatal day (PN) 4), characterized by the expansion of the distal immature alveoli; and two stages of alveolarization (P4-young adulthood), wherein secondary septa develop during alveolar maturation (Schittny, 2017) (Fig. 2A).

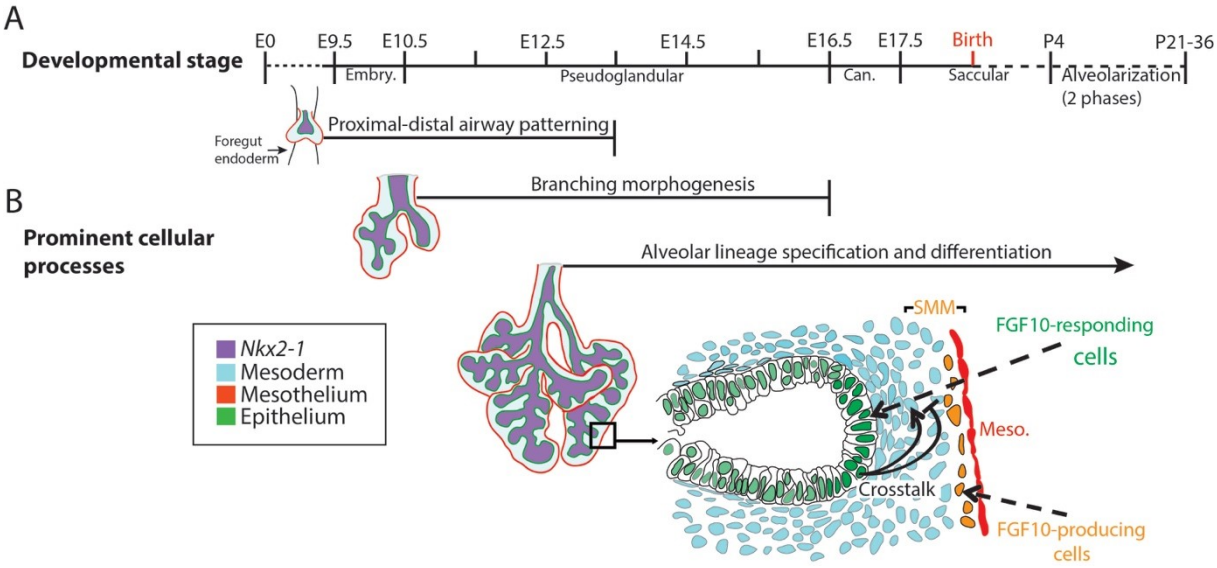

Figure 2 – Overview of early lung development (E9.5-E12.5). (A) The stages of mouse lung development, beginning with the embryonic (E9.5-E10.5), pseudoglandular (E10.5-E16.5), canalicular (E16.5-E17.5), saccular (E17.5-P4), and ending with two phases of alveolarization (P4-P36). **(B)** Prominent epithelial processes include proximal-distal airway patterning (E9.5-E13.5), branching morphogenesis (E10.5-E16.5), and alveolar lineage specification and differentiation (E12.5-onward). As illustrated, these processes are regulated in large part by mesenchymal-epithelial crosstalk, including FGF10 signalling. FGF10 ligands are produced by the submesothelial mesenchyme (SMM) and signal to the distal epithelium, whereupon other ligands are produced in response, and which are secreted back to the mesenchyme to either promote or inhibit FGF10 signalling in a regulatory feedback loop.

Several evolutionarily conserved signalling pathways control lung development. These include bone morphogenic protein (BMP), epidermal growth factor (EGF), sonic hedgehog (SHH),

transforming growth factor beta (TGF-β), vascular endothelial growth factor (VEGF), Wnt, and fibroblast growth factor (FGF) signalling pathways. Each of these is involved in the intricate epithelial-mesodermal crosstalk necessary to initiate and coordinate branching morphogenesis and cellular differentiation. Crosstalk involves a diffusible ligand secreted either from the surrounding mesoderm or the epithelium signalling to a cognate receptor located in the adjacent cellular compartment. Upon activation of the receptor, signals are transduced to the nucleus, where target genes are regulated. Responding cells may produce additional ligands, which are then secreted, signalling in turn to the neighbouring cellular compartment (Fig. 2B). This crosstalk produces positive and negative feedback loops, which are necessary to coordinate axis and branching patterns during development, to ensure proper spatial-temporal expression of morphogens in the mesenchyme, and to maintain a distal tip progenitor and organizing center (for reviews see Warburton et al., 2005; Morrisey and Hogan, 2010; Swarr and Morrisey, 2015; Zepp and Morrisey, 2019). The work presented in this thesis focuses on the role of FGF signalling.

1.3 Overview of FGF/FGFR signalling

Fibroblast growth factors (FGFs) were first identified in the 1970s, when researchers discovered that extracts from bovine brains and pituitary glands could stimulate the proliferation of mouse fibroblast cell lines (Armelin, 1973; Gospodarowicz, 1975; Gospodarowicz et al., 1978). The mitogenic ligands from these extracts were isolated and called FGF1 and FGF2, becoming the founding members of the largest family of growth factors to date, which includes 22 different members (FGFs 1-23; FGF15, absent in humans but present in mice, is likely the mouse ortholog of human FGF19, which is absent in mice) (Ornitz and Itoh, 2001).

FGFs are broadly grouped into three categories depending on their mode of action: secreted endocrine and paracrine proteins, or intracellular proteins. These three groups are further divided into seven subfamilies based on biochemical function, sequence similarities, and phylogenetic analysis (Fig. 3A). Paracrine FGFs are considered canonical (subfamilies 1, 4, and 7-9), and they regulate many different developmentally relevant biological processes,

including proliferation, differentiation, and morphogenesis. These ligands bind with varying levels of specificity to ligand-dependent cell-surface fibroblast growth factor receptors (FGFRs), which are a class of receptor tyrosine kinases (RTKs). There are four main FGFRs (FGFRs 1-4), each composed of an extracellular region of three immunoglobulin (Ig)-like domains (Ig-I-III), a single transmembrane helix, and two intracellular tyrosine kinase domains. Furthermore, there are two alternative exons which code for the second half of the Ig-III domain of FGFRs 1-3, producing either a 'IIIb' or a 'IIIc' splice variant (Fig. 3B). The first variant primarily presents on epithelial cells, whereas the latter exists on mesenchymal cells. These spliced variants increase the number of FGFRs to seven (FGFR1-3 IIIb or IIIc, and FGFR4).

Control of FGF/FGFR-dependent biological processes requires tight spatiotemporal regulation of ligand-receptor interactions. Inactive FGFRs exist as monomers on the cell surface. It has been suggested that autoinhibition of FGFR activity depends on the Ig-like domain I (Ig-I) and an acidic amino acid sequence (acidic box) positioned in the domain I-II linker region (Kalinina et al., 2012) (Fig. 3B). Ligand binding specificity is determined by the Ig-like domains and linker region of DII and DIII. Canonical FGF binding affinity is greatly increased by heparan sulfate (HS) in the extracellular matrix or bound to transmembrane proteoglycans located on the cell surface to form heparan sulfate proteoglycan complexes (HSPG). HS independently interacts with both FGF ligands and receptors through HS binding sites (HSBS). These regulatory mechanisms ensure that FGFR activation only occurs in the presence of a cognate FGF ligand bound to HS/HSPGs. FGF/HS/FGFR form 1:1:1 monomers which then can form stable 2:2:2 dimers. Dimerization brings the cytoplasmic tyrosine kinase domains together, resulting in the autophosphorylation of tyrosine residues, which thereby triggers specific signalling cascades. Common transduction cascades include RAS/MAPK, PI3K/AKT, and PLCY/PKC, all of which can be activated by each FGFR (Ornitz and Itoh, 2015, 2022) (Fig. 3C).

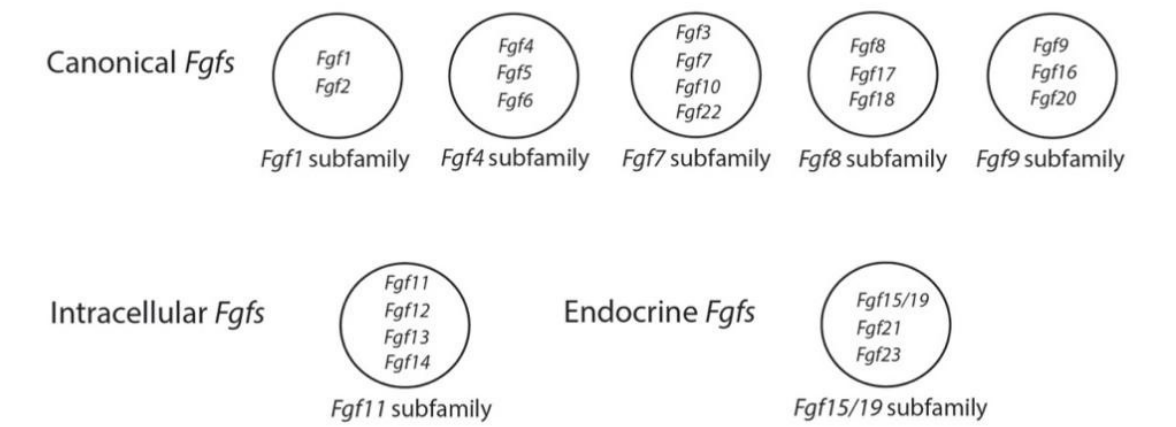
A Fgf gene subfamilies
Canonical Fgfs
Fgf1
Fgf2
Fgf1 subfamily
Fgf4
Fgf5
Fgf6
Fgf4 subfamily
Fgf3
Fgf7
Fgf10
Fgf22
Fgf7 subfamily
Fgf8
Fgf17
Fgf18
Fgf8 subfamily
Fgf9
Fgf16
Fgf20
Fgf9 subfamily
Intracellular Fgfs
Fgf11
Fgf12
Fgf13
Fgf14
Fgf11 subfamily
Endocrine Fgfs
Fgf15/19
Fgf21
Fgf23
Fgf15/19 subfamily

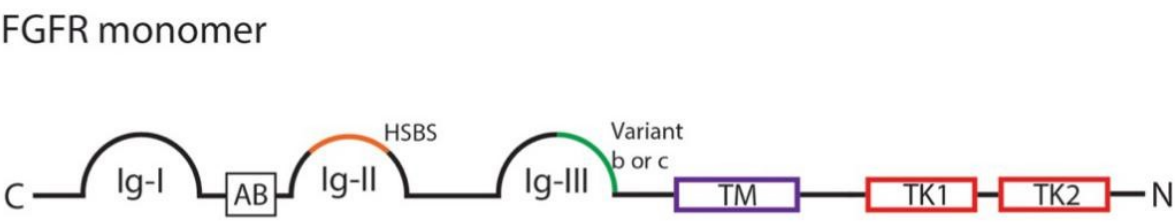
B FGFR monomer
C
Ig-I
AB
Ig-II
HSBS
Ig-III
Variant
b or c
TM
TK1
TK2
N

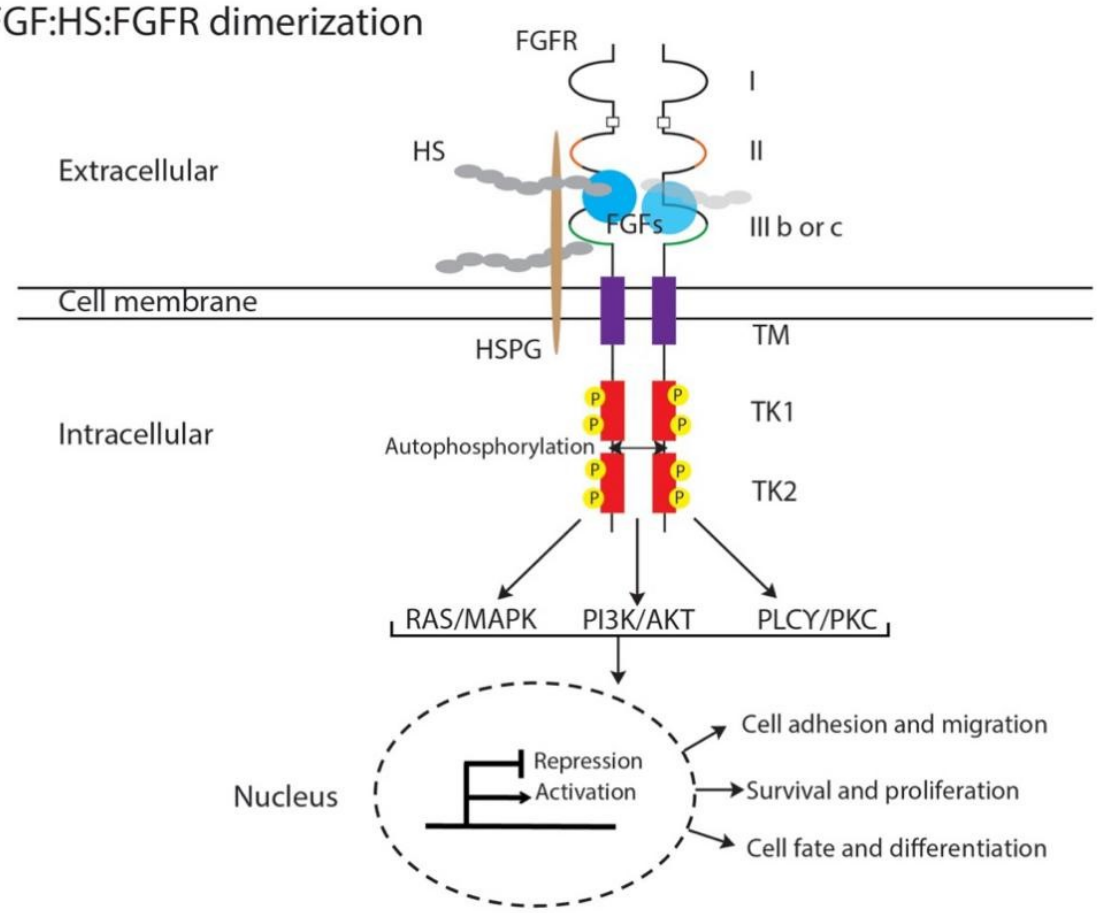
C FGF:HS:FGFR dimerization
FGFR
I
II
III b or c
HS
FGFs
Extracellular
Cell membrane
HSPG
TM
Intracellular
Autophosphorylation
TK1
TK2
RAS/MAPK
PI3K/AKT
PLCY/PKC
Nucleus
Repression
Activation
Cell adhesion and migration
Survival and proliferation
Cell fate and differentiation

Figure 3 – Fibroblast growth factor families, receptor, and mechanism of action. (A) *Fgf* genes cluster into seven subfamilies, five of which include canonical paracrine *Fgfs*, one of which includes the intracellular *Fgfs*, and one including the endocrine *Fgfs*. **(B)** An FGF receptor monomer includes three extracellular immunoglobulin-like domains (Ig-I–III), a transmembrane I domain, and two intracellular tyrosine kinase (TK1–2) domains. FGFR1-3 each has two splice variants in the second portion of the Ig-III domain (IIIb or c; green). Autoinhibition of FGFR monomers is achieved through an acidic box (AB) in the linker region between Ig-I and Ig-II. Heparan sulfate binding sites (HSBS) are present in Ig-II (orange). **(C)** FGF ligands, in association with heparan sulfate proteoglycans (HSPG), promote FGFR dimerization. Once activated, specific tyrosine residues are autophosphorylated in the intracellular TK domains, and specific signalling cascades are initiated (see text for more details).

1.4 Branching morphogenesis in the mouse lung

After the two epithelial buds of the mouse lung form at E9.5, they elongate and grow into the surrounding mesenchyme, becoming the primary bronchi. Branching morphogenesis begins around E10.5, at the beginning of the pseudoglandular stage, as the primary bronchi commence ordered iterations of bud initiation, elongation, and, for dichotomous branches, bifurcation. After 13-17 generations, branching concludes during the canalicular stage between E16.5-E17.5. The resulting arborized scaffold of bronchioles and distal airways supports the acinar buds, which will eventually form the mature alveoli (Cardoso and Lü, 2006).

It has been hypothesized that mouse lung branching is controlled by genetically-encoded subroutines, which operate reiteratively during morphogenesis (Metzger et al., 2008b). It was demonstrated via detailed *in vivo* mapping of branching over embryonic development that a precise and predictable spatiotemporal order of branches could be identified. Three modes of branching were observed and are generally accepted in the literature: monopodial domain branching, where buds branch from the periphery of existing branches; and dichotomous planar bifurcation and orthogonal bifurcation, which are distinguished according to their orientation relative to the parent branch.

Other researchers have questioned the idea of genetically encoded subroutines, especially after the first generation of branching, when both spatial and temporal variations become common. Instead, it has been suggested that ordered branching can be fully explained by airway epithelial-mesenchymal crosstalk, resulting in the space-filling expansion of the airways, which adopts its precise local geometry based on the shape of the surrounding mesoderm, and ultimately by the shape of the thoracic cavity (Blanc et al., 2012; Clément et al., 2012). In other words, there does not seem to be a need for genetically encoded subroutines to explain branching. Despite this open question, the appearing stereotypy of lung branching, and the nomenclature employed to describe it, are overwhelmingly appreciated in the literature.

1.4.1 The role of FGFR2b signalling on branching morphogenesis

It is well established that FGF10/FGFR2b signalling is necessary to initiate and regulate branching morphogenesis *in vivo*, as both *Fgf10*- and *Fgfr2b*-null embryos display lung agenesis after the primary bronchi are established (Sekine et al., 1999; De Moerlooze et al., 2000), while *Fgf10* hypomorphic lungs exhibit decreased branching overall (Ramasamy et al., 2007). Initially, it was hypothesized that localized FGF10 expression was required to initiate bud formation, perhaps through the concentrated proliferation of epithelial cells, and to serve as chemotaxic signalling centers, guiding actively elongating epithelium. Early *in vitro* experiments using recombinant FGF10-soaked (rFGF10) beads positioned adjacent to mesenchyme-free epithelium isolated from developing lungs, which were then cultured three-dimensionally in reconstituted basement membrane (Matrigel), showed that the epithelium branched and grew towards the rFGF10-soaked beads (Park et al., 1998; Lebeche et al., 1999; Weaver et al., 2000; Lü et al., 2005). However, in other 3D culture experiments, where rFGF10 was added ubiquitously to the Matrigel, thereby precluding localized FGF10 expression, the embedded epithelium still branched relatively normally (Ohtsuka et al., 2001). Additionally, *in vivo* studies have demonstrated that branching could be rescued in *Fgf10-/-* knockout embryos upon conditional and ubiquitous FGF10 expression in the mesenchyme (Volckaert et al., 2013).

During early pseudoglandular lung development, FGF10 is expressed in the sub-mesothelial mesenchyme around the distal epithelial buds (Bellusci et al., 1997) (Fig. 4). FGF10 signals through its epithelial receptor fibroblast growth factor receptor 2b (FGFR2b), thereby upregulating the expression of the transcription factors ETV4 and ETV5 (Herriges et al., 2015; Jones et al., 2019b). These in turn upregulate the transcription of *Shh*. SHH is secreted from the epithelium, and, depending on its concentration in the surrounding extracellular matrix, either represses FGF10 expression or upregulates its own SHH antagonist, hedgehog interacting protein (HHIP), whereupon levels of FGF10 are maintained. In this manner, localized expression of FGF10 in the mesenchyme dynamically shifts over time, remaining concentrated around the distal bud tips, and is downregulated in the bud clefts during bifurcation, and in the proximal stalks, where levels of HHIP are lower. This dynamic feedback mechanism also interacts with many of the other pathways and feedback loops controlling branching morphogenesis (for example, SHH also interacts with BMPs and WNTs) in an intricate regulatory web (reviewed in Swarr and Morrisey, 2015).

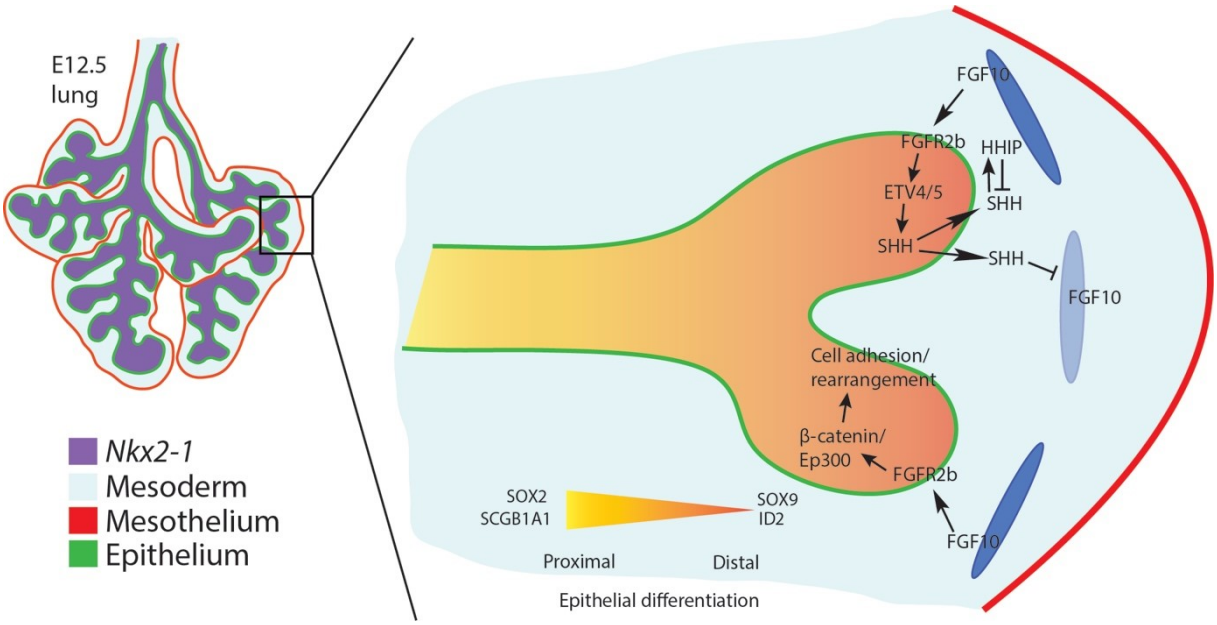

Figure 4 – Branching in pseudoglandular stage lungs is controlled by FGF10/FGFR2b signalling. The illustration shows a distal branch along the proximal-distal axis (orange gradient). Distal tips elongate towards areas of high FGF10 expression (dark blue ovals). FGF10 signals via FGFR2b on the epithelial surface, upregulating SHH, which in turn signals back to the mesenchyme to inhibit FGF10 in a negative feedback loop. FGF10 controls cell adhesion

and rearrangement through β-catenin activity. Additional details found in main text. Figure modified from Jones et al., 2021.

How exactly FGF10/FGFR2b signalling regulates the branching process, from bud initiation and elongation to bifurcation, remains an area of active research. We recently published a review on the current state of knowledge concerning this question (Jones et al., 2021). Many of the proposed explanations linking FGF10/FGFR2b signalling to branching regulation remain speculative. For instance, during bud initiation (domain branching), increased proliferation in localized regions of peripheral branch epithelium is sufficient to cause epithelial buckling and the protrusion of a new branch (Varner and Nelson, 2014). Evidence suggests that these regions of epithelial buckling can be stabilized through cellular mechanisms such as apical constriction, which changes the geometry of the distal tip cells prior to directed branch elongation (Fig. 5A). Apical constriction depends on actomyosin cytoskeletal reorganization. Work on chick embryos showed that apical constriction was prevented upon administration of a FGF receptor tyrosine kinase inhibitor (Kim et al., 2013); whereas, in the mouse, more recent evidence has suggested that actomyosin rearrangement depends in part on Wnt/β-catenin signalling acting downstream of FGF10/FGFR2b signalling (Fumoto et al., 2017).

After domain branch establishment, buds elongate and grow into the surrounding mesenchyme. This stage of branch formation is a prime example of biophysical mechanisms coordinating with molecular pathways to orchestrate morphogenesis. Here, amniotic fluid flow within the lumens of the airways, together with the cellular regulation of FGF10/FGFR2b signalling, regulates branch growth (Unbekandt et al., 2008). As Figure 5B shows, amniotic fluid flow is relatively strong and directed in the conducting airways and proximal stalks of growing branches. This produces mechanical stress which is sensed and transduced *via* mechano-sensory mechanisms by the epithelial cells lining these regions (Bokka et al., 2015b, 2015a, 2016; George et al., 2015; Nelson et al., 2017). In response, cells might adjust polarity, alter their cytoskeleton, or form thickened epithelial sheets in the more proximal regions of the branch. In addition, increased intraluminal fluid pressure regulates mitotic spindle orientation by fixing it, so that when these cells divide, they do so parallel to the plane of the proximal distal axis (Tang et al., 2011, 2018). Compare this to the situation at the distal tip,

where mechanical stress due to amniotic fluid flow is relatively weak and variable. Here, the polarity of cells is not well-defined, and, due in part to FGFR2b signalling, the mitotic spindle orientation of these highly proliferative cells is more random (Tang et al., 2011, 2018). This allows these distal regions to grow adaptively, adjusting course to ensure optimal space-filling occupancy. Note also that airway smooth muscle cells (ASMCs) emerge around the most proximal stalk region at this stage of branching.

Eventually, the distal branch tip will undergo planar or orthogonal bifurcation (Metzger et al., 2008b). In general, bifurcation involves four steps: (1) branch arrest and tip dilation, where the branch stops its directional growth and the distal lumen swells to form a bulb; (2) tip flattening, where the bulbous tip assumes a flattened distal edge; (3) cleft initiation, where a cleft forms at the midline of the flattened tip; and (4), cleft deepening and sister branch elongation, where the newly formed branches restart the iteration of elongation and eventual bifurcation (Kim et al., 2015). At this stage, the stalk of the branch is stabilized by increased ASMC deposition, and proximal cell proliferation is drastically reduced (Fig. 5C). The decision of the distal tip to branch is partly controlled by molecular mechanisms, as well as by barriers to elongation found in the extracellular matrix, such as fibronectin (De Langhe et al., 2005; Warburton et al., 2005). An intriguing example of a barrier to growth is the deposition of ASMC in the cleft of the branching tip. Evidence suggests that these cells begin to localize in the mesenchyme adjacent to the future bud cleft *before* the bud itself has begun bifurcating (Kim et al., 2015). While the interpretation of this finding has recently been questioned (Young et al., 2020), the deposition of ASMCs adjacent to future cleft sites does suggest these cells play a role in branching, perhaps in conjunction with fibronectin and other extracellular matrix components. Furthermore, these ASMCs appear to be regulated by SHH signalling (Weaver et al., 2003; White et al., 2006), which concomitantly causes the FGF10 signalling centers to split, following the inhibitory feedback mechanism described above (Fig. 4). This combined effect of a mesenchymal barrier to elongation and the establishment of new signalling centers ensures the sister buds of the bifurcating tip are set for a new round of directed branch elongation.

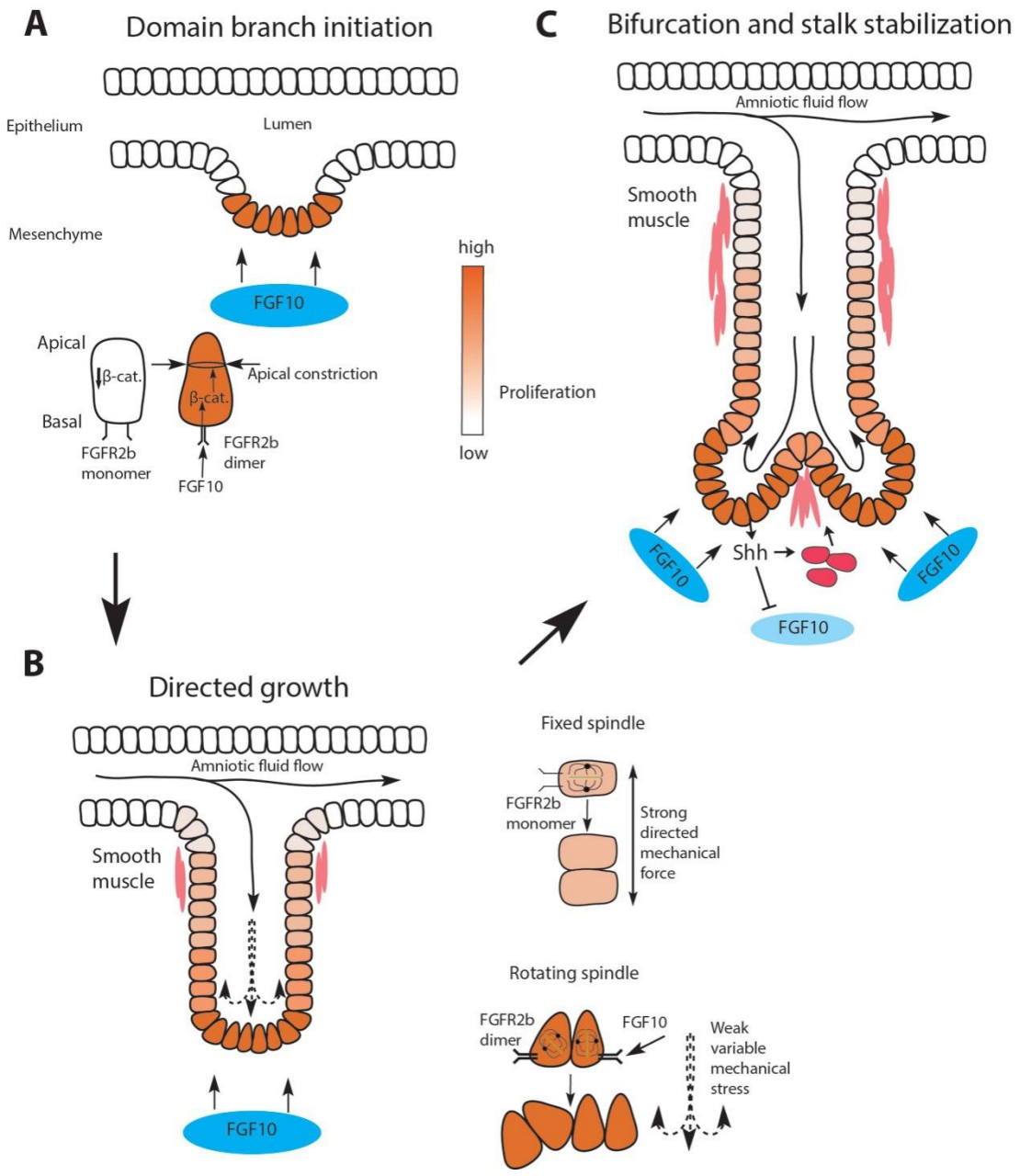

Figure 5 – Model of branch formation, directed growth, and bifurcation. (A) Domain branches form on the lateral sides of established airways. High localized cell proliferation in response to regions of FGF10 expression (blue oval) causes the epithelial sheet to buckle outward. Bud tips assume a clear apical-basal polarity in response to β-catenin-mediated apical constriction, which is regulated in part by FGF10 signalling. **(B)** An interplay of mechanical forces and FGF10 signalling coordinates directed branch growth towards regions of high FGF10 expression. Here, amniotic fluid flow results in strong and directed mechanical forces on the proximal branch epithelium, which orients the mitotic spindle of the dividing cells parallel to the proximal-distal axis. At the bud tips, mechanical stress is lower and more variable, which, in coordination with FGF10 signalling, promotes the random spindle orientation of dividing cells, enabling the branch to grow in the optimal direction. **(C)** As the

branch grows, the proximal stalk is strengthened by smooth muscle (red cells), while the distal tip eventually encounters barriers to its progress, such as smooth muscle deposited in the mesenchyme at bifurcation points. Concomitant with this, the FGF10/SHH feedback loop causes the FGF10 signalling center to split (dark blue ovals), resulting in two centers which guide the newly formed daughter branches. See text for more details. Figure modified from Jones et al., 2021.

Continued investigation is required to uncover novel roles played by FGF10 during airway branching morphogenesis, and to refine currently proposed models. In addition to molecular regulation, ongoing research in the field has focused on determining the biomechanical and physical means, as well as the mathematical principles by which FGFR2b signalling regulates branching morphogenesis. This work highlights the physical regulation of cell and tissue geometries and mechanics, of extracellular matrix (ECM)-driven morphogenesis, and of mesenchymal determinants to branching. There is a growing appreciation of the interplay between mechanisms under molecular control and purely physical and mechanical forces regulating branching morphogenesis, which has engaged diverse specialists, from molecular and cell biologists to mathematical and computational modellers (Lang et al., 2018, 2021; Jones et al., 2021).

1.5 Alveolar epithelial lineage formation in the mouse lung

The specialized region of *Nkx2-1* positive foregut endoderm which marks the site of lung organogenesis ultimately contains the progenitors for all the specialized airway epithelial cells of the mature lung. Airway epithelium is broadly divided based on geographical, cellular, and molecular criteria into proximal (the stalk) and distal (the tip) regions. The proximal epithelium is composed of relatively differentiated cells and can be demarcated histologically by the expression of SOX2 and SCGB1A1; the distal epithelium contains the alveolar epithelial progenitor cells characterized by SOX9 and ID2 expression (Fig. 4). Airway progenitors can be classified into two major groups: bronchiolar progenitors and alveolar progenitors, which include AT1, AT2 and bipotential progenitors (Fig. 6). A specialized cell – the bronchioalveolar stem cell (BASC) present at the bronchioalveolar duct junction (BADJ) – expresses markers for the proximal and distal lineages, and can serve as a progenitor for each (Jones et al., 2019c).

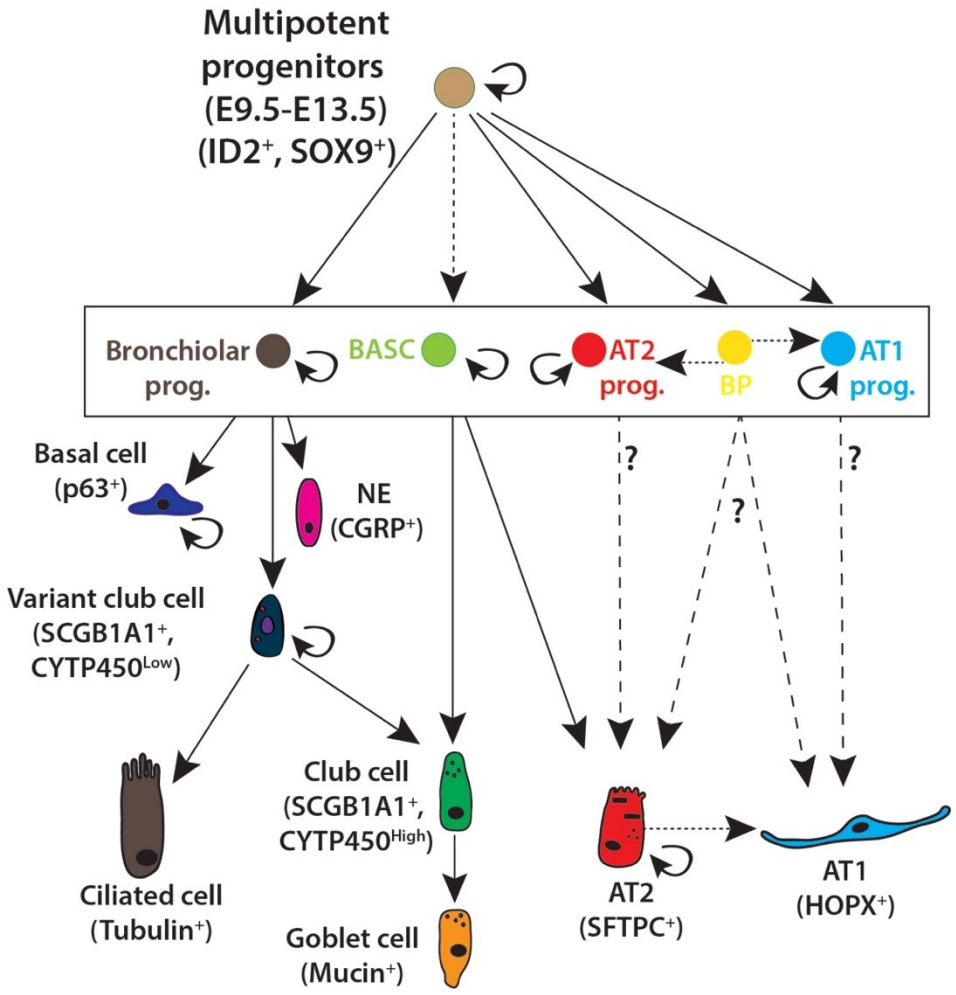

Figure 6 – Lung epithelial cell tree. Between E9.5-E13.5, multipotent epithelial cells positive for ID2 and SOX9 give rise to the bronchiolar progenitors and the distal alveolar progenitors (AT1, AT2, and bipotential), and ultimately, to all the different epithelial cell types of the mature lung. Hashed lines indicate uncertainty about the level of contribution of a parent progenitor population to the daughter population. Question marks (?) indicate current debate, as discussed below, on the relative importance of the three alveolar progenitors to mature alveolar cell populations. BASC = Bronchioalveolar stem cell; AT1 = Alveolar type 1 cell; AT2 = Alveolar type 2 cell; BP = Bipotential progenitor; NE = Neuroendocrine cell.

The mechanisms controlling the transitions of the airway epithelium from a branching program to the airway and alveolar differentiation programs are poorly understood. It is well-established that SOX9 expression not only marks the earliest epithelial lung progenitors, but also the distal cells during branching morphogenesis (Rockich et al., 2013). During lung specification and early branching, SOX9 is partly controlled through beta-catenin (CTNNB1), which prevents expression of gastrointestinal gene markers, as well as the proximal airway

epithelial marker SOX2, thereby promoting the undifferentiated status of lung-specific epithelial cells (Ostrin et al., 2018). As branching proceeds, SOX9 expression persists in the distal airway progenitors, while more proximal daughter cells begin differentiating into the different airway cell types expressing SOX2. It has been suggested that the branching program of epithelial progenitors antagonizes the differentiation program in these cells (Chang et al., 2013), and that the choice of a given progenitor cell to favour one developmental program over another is precisely balanced by spatiotemporal cues (Yang and Chen, 2014). These cues include ligand/receptor interactions and signalling pathways, as well as cellular morphology and geographic location.

That the alveolar lineages derive from distal multipotent SOX9-positive progenitors is clear. Less clear is when, and from exactly which progenitor pool(s), the alveolar lineages emerge. Like most biological realities, boundaries and classifications tend to overlap and blur into one another. How should a *bona fide* alveolar lineage progenitor be classified? Are there multiple classes of progenitors? How heterogeneous are the progenitor pools? Considering these questions, two different models of alveolar lineage specification and formation have been proposed: the bipotential progenitor model, and the early lineage specification model.

The bipotential progenitor model proposes that oligopotent alveolar progenitors give rise to a population called “bipotential progenitor cells (BP cells)” (Treutlein et al., 2014). According to the model, these cells are found around E16.5 in the mouse and can self-renew or differentiate into either of the two alveolar epithelial lineages. Based on single-cell transcriptomic experiments conducted at different embryonic timepoints, it was shown that BP cells have a gene signature characteristic of both mature AT1 and AT2 cells. During alveologenesis, a BP cell downregulates one of the two alveolar epithelial cell signatures, while upregulating the other to become a mature alveolar epithelial cell. However, a critical limitation of the work supporting this model was that lineage tracing of the BP cells was missing. Therefore, it remains unclear what proportion of mature alveolar epithelial cells pass through a BP cell state.

The second and more recent model of alveolar lineage formation proposes that the majority of mature AT1 and AT2 cells arise from unipotent, not bipotential, progenitors which are specified as early as E13.5 in the mouse lung (Frank et al., 2019). This 'early lineage specification' model was supported by single cell transcriptomic analyses along with lineage tracing experiments. In one of these experiments, a dual transgenic mouse line was used to label SFTPC-positive and HOPX-positive cells at E15.5. These cells were considered bipotential, and it was suggested, based on their minor contribution to the more mature AT1 and AT2 cell populations at PN0, that BP cells play a minor role in alveolar lineage formation. However, given the timepoints chosen in this study to label cells, it remains unclear what proportion of alveolar epithelial progenitors are unipotent at E13.5; the significance of the BP cell during alveolar lineage formation, therefore, is still to be established.

1.5.1 The role of FGFR2b signalling on alveolar lineage formation

Previous studies have uncovered transcriptional regulators and signalling pathways involved in alveolar lineage specification and differentiation, including the transcription factors CCAAT enhancer binding protein (C/EBP) and cAMP response element binding protein (CREB), as well as glucocorticoid signalling (Martis et al., 2006; Manwani et al., 2010; Bird et al., 2011; Habermehl et al., 2011). Furthermore, our lab has recently described that miR-142 plays a role in the fate of alveolar progenitors (Shrestha et al., 2017, 2019). In the absence of miR-142, a proportion of alveolar progenitors differentiate towards the AT2 lineage in an Ep300-dependent manner, while overexpression of miR-142 in alveolar progenitors leads to their differentiation towards the AT1 lineage. Early evidence suggests a role for FGFR2b in this process. When miR-142 is knocked-out, FGFR2 is upregulated and increased Erk signalling is observed in experimental lungs. It remains unclear how exactly FGFR2b signalling and miR-142 are related. Of note, the proportion of alveolar epithelial progenitors which showed a response to miR-142 knock-out was small, yet highly significant.

The critical importance of FGF/Kras signalling on alveolar lineage formation is well-known in the field. For example, in the previously cited work on SOX9, it was observed that overexpression of the GTPase *Kras*, which acts downstream of FGF signalling, resulted in increased branching and the suppression of alveolar differentiation; whereas loss-of-function

of *Fgfr2* revealed that *Sox9* is a downstream target of FGF signalling (Chang et al., 2013). This work supports the general model that the distal-most progenitors respond most significantly to FGFR2b signalling, which gradually loses its importance as progenitors differentiate in a distal-proximal order (Fig. 7). Apart from a few studies, however, the mechanisms by which FGF signalling regulates the alveolar differentiation program remain unknown.

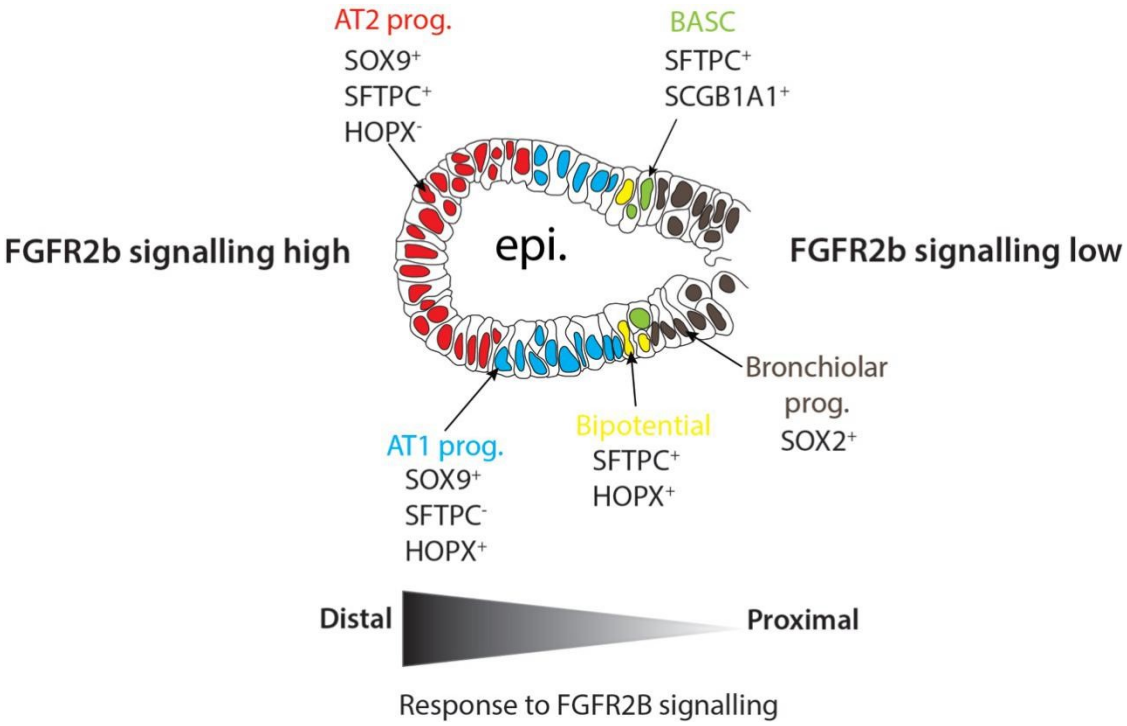

Figure 7 – The relative positions of epithelial cell types in a pseudoglandular stage lung bud. From a distal-proximal direction, progenitor populations include AT2, AT1, BASC/Bipotential, and bronchiolar progenitors. In general, the response of these populations to FGFR2b signalling is highest at the tip (AT2 progenitors), and lowest in the proximal regions (bronchiolar progenitors).

Most research on FGF regulation of the alveolar lineages has looked at AT2 cells in the context of adult homeostasis and repair after injury. For example, using the bleomycin-induced lung fibrosis model, it was reported that mice with specific deletion of *Fgfr2* in SFTPC-positive AT2 cells were less able to repair after injury, showed increased mortality, and had fewer AT2 cells overall (Dorry et al., 2020). This study also showed that even in the absence of injury, *Fgfr2b* deletion resulted in enlarged airspaces and increased collagen deposition, as well as a

decrease in the number of AT2 cells, suggesting that FGFR2 signalling is required for AT2 maintenance.

These results support earlier work which looked at the loss of *Etv5* in AT2 cells during homeostasis and repair after bleomycin-induced lung injury (Zhang et al., 2017). Here, it was shown that ETV5 was required to maintain AT2 cells, for in its absence, AT2 cells transdifferentiated to AT1s. Furthermore, loss of *Etv5* in AT2 cells drastically impaired the repair process of the epithelium after lung injury, resulting in fewer AT2 cells altogether. It is well established that ETV5 is regulated by FGFR2b signalling (Herriges et al., 2015; Jones et al., 2019b), and it was suggested that ETV5 protein stability in AT2 cells is controlled by Ras-mediated Erk signalling (Zhang et al., 2017).

Continuing work on FGF signalling regulation of alveolar lineage development has come from our lab. For instance, we have reported on transgenic mice heterozygous for *Fgf10* (*Fgf10*$^{+/-}$) (Chao et al., 2017). When analyzed at PN3, *Fgf10*$^{+/-}$ mice had a lower proportion of AT2 cells over total epithelial cells compared to wildtype controls, indicating that FGF10/FGFR2b signalling is required for AT2 lineage formation and/or maintenance. This idea is supported by research where epithelial FGFR2 expression had been knocked-out using an ID2-CreERT driver line at E15.5, and a decreased AT2/AT1 cell ratio was observed at E18.5 (Li et al., 2018).

Given the research that has been reviewed here, the fact remains that almost 25 years after its discovery as a key signalling pathway regulating lung development, the primary targets and biological activities controlled by FGF/FGFR2b signalling largely remain unknown (El Agha and Bellusci, 2014). Studying the regulation of FGFR2b signalling *in vivo* has been challenging, given that constitutive deletion of either *Fgf10* or *Fgfr2b* leads to lung agenesis, therefore leaving little tissue to study. Conditional deletions of the *Fgf10* allele, for example, or of *Fgfr2* are possible using Cre-based models. However, distinguishing between primary and secondary biological effects is difficult, given that the time separating Cre activity from complete gene inactivation is usually 24 to 48 hours (Abler et al., 2008). Furthermore, genetic deletion of *Fgf* genes does not necessarily translate to the simultaneous loss of the existing functional

protein, since the existing protein pool depends, for example, on the degradation rate of FGFs present in the extracellular matrix and bound to heparan sulfate proteoglycans (Makarenkova et al., 2009; Patel et al., 2017); total loss of functional protein might take hours or days. Studies using a dominant negative mouse model to conditionally and quickly inhibit FGF ligands at the protein level do exist, but detailed analyses of direct epithelial targets and biological responses are lacking (Hokuto et al., 2003; Danopoulos et al., 2013).

2 Aims of study

As the preceding review has shown, there is a need in the field of lung development for a basic understanding of the transcriptional targets and biological responses of FGFR2b signalling on distal airway epithelium. The following manuscript details the research our lab has conducted to address this need. In this work, we have utilized *in vivo* mouse models to conditionally inhibit FGFR2b signalling at different embryonic timepoints and have assessed the transcriptional and biological impacts shortly after inhibition, as well as later in embryonic development. Furthermore, through *in silico* data mining, we have begun the characterization of FGFR2b-responding cells during homeostasis and repair after injury.

The aims of my thesis are as follows:

1. To use a global inhibition mouse model to identify direct transcriptional targets of, and investigate major biological processes regulated by, FGFR2b signalling over embryonic (E9-E10) and pseudoglandular lung development (E10.5-E16.5)
2. To employ a cell-autonomous mouse model to label and knock-out *Fgfr2b* in specific cells to assess the impact of FGFR2b signalling on alveolar epithelial lineage formation and differentiation (E16.5-E18.5)
3. To data mine published datasets to identify and characterize populations of alveolar epithelial cells responding to FGFR2b signalling during development, homeostasis, and repair after injury

3 Materials and methods

3.1 Ethical statement and husbandry

Animal experiments, harvesting organs and tissues from wild type and mutant mice following euthanasia using pentobarbital was approved at Justus Liebig University Giessen by the federal authorities for animal research of the Regierungspraesidium Giessen, Hessen, Germany (Approved Protocol GI 20/10 Nr. G 84/2016).

All mice used to generate experimental and control embryos were housed in a specific-pathogen-free (SPF) environment with free access to food and water. Up to five females were housed together, while males were housed singly. Females between 9-12 weeks of age were used to generate embryos.

3.2 Genetically modified mouse models

Experiments to inhibit FGFR2b ligands were conducted using a previously described and validated inducible dominant negative mouse model: *ROSA26*$^{rtTA/rtTA}$*; Tg(tet(o)sFgfr2b)/+* (B6-Cg-Gt(ROSA)26Sor$^{tm1.1(rtTA,EGFP)Nagy}$ Tg(tetO-Fgfr2b/lgh)1.3Jaw/sbel) (Danopoulos et al., 2013). These mice were generated by crossing *Rosa26*$^{rtTA/rtTA}$ mice with *Rosa26*$^{rtTA/rtTA}$; Tg(*tet(o)sFgfr2b)/+* mice to obtain experimental (*Rosa26*$^{rtTA/rtTA}$*; Tg(tet(o)sFgfr2b)/+*) and littermate control (*Rosa26*$^{rtTA/rtTA}$*; +/+*) embryos. This model employs a reverse tetracycline transactivator (rtTA) under the transcriptional control of the ubiquitous *Rosa26* locus. Upon administration of doxycycline, the rtTA binds to the tetracycline operator (tetO), inducing the transcription of a soluble dominant negative form of *Fgfr2b* (*sFgfr2b*), which is secreted from cells and acts to sequester all FGFR2b ligands in the extracellular matrix.

Cell autonomous *Fgfr2b* deletion and lineage labelling in alveolar progenitors was achieved by using a cell-type specific CreERT2 recombinase combined with a tandem dimer (*td*)*Tomato*^{flox} reporter and an *Fgfr2b*^{flox} knock-in line. Upon administration of tamoxifen, CreERT2 translocates to the nucleus, recombining the loxP-flanked stop cassette upstream of the *tdTomato* construct, as well as excising the IIIb exon in the *Fgfr2* gene. Targeting of AT1 progenitors was achieved by creating *Hopx*$^{CreERT2/+}$*; Fgfr2b*$^{flox/flox}$*; tdTomato*$^{flox/flox}$ embryos

(Stock *Hopx*$^{tm2.1(cre/ERT2)Joe}$*FgfR2*^{tm1Dsn}*Gt(ROSA)26Sor*$^{tm9(CAG-tdTomato)Hze}$/sbel). Experimental litters were obtained by crossing *Hopx*$^{CreERT2/+}$*; Fgfr2b*$^{flox/flox}$*; tdTomato*$^{flox/flox}$ mice with *Hopx*$^{+/+}$*; Fgfr2b*$^{flox/flox}$*; tdTomato*$^{flox/flox}$ mice, whereas control litters were obtained by crossing *Hopx*$^{CreERT2/+}$*; Tomato*$^{flox/flox}$ mice with *tdTomato*$^{flox/flox}$ mice. Targeting of AT2 progenitors was achieved by creating *Sftpc*$^{CreERT2/+}$*; Fgfr2b*$^{flox/flox}$*; tdTomato*$^{flox/flox}$ embryos (STOCK *Sftpc*$^{tm1(cre/ERT2,rtTA)Hap}$*Fgfr2*^{tm1Dsn} *Gt(ROSA)26Sor*$^{tm9(CAG-tdTomato)Hze}$/sbel). Experimental litters were obtained by crossing *Sftpc*$^{CreERT2/+}$*; Fgfr2b*$^{flox/flox}$*; tdTomato*$^{flox/flox}$ mice with *Sftpc*$^{+/+}$*; Fgfr2b*$^{flox/flox}$*; tdTomato*$^{flox/flox}$ mice, whereas control litters were obtained by crossing *Sftpc*$^{CreERT2/+}$*; tdTomato*$^{flox/flox}$ mice with *tdTomato*$^{flox/flox}$ mice.

Induced constitutive expression of FGFR signalling in labelled AT2 progenitors was accomplished using a *Sftpc*$^{CreERT2/+}$*; Rosa26*$^{rtTAflox/+}$*; Tg(tet(o)caFgfr1/+; tdTomato*$^{flox/+}$ mouse line (STOCK *Sftpc*$^{tm1(cre/ERT2,rtTA)Hap}$*Gt(ROSA)26Sor*$^{tm1.1(rtTA,EGFP)Nagy}$*Tg(tetO-Fgfr3*R248C/Fgfr1)#Dor Gt(ROSA)26Sor*$^{tm9(CAG-tdTomato)Hze}$/sbel) (Cilvik et al., 2013). Pregnant females carrying littermate experimental (expressing *Tg(tet(o)caFgfr1*), and control (without *Tg(tet(o)caFgfr1*) embryos were used for experiments.

3.2.1 *In vivo* activation of rtTA/tet(o) and CreERT2/loxp systems

Timed-pregnant females were used to conduct *in vivo* experiments, where embryonic day I 0.5 was assumed to be noon on the day a vaginal copulation plug was found.

To activate the rtTA/tet(o) system, doxycycline, dissolved either in PBS (for injection) or in water, was administered at the desired timepoint via an intraperitoneal injection (Dox-IP) (Dosage: 0.0015 mg doxycycline/g mouse weight), or through drinking water (Dosage: 200 µg doxycycline/ml water). To activate the CreERT2/loxp system, tamoxifen, dissolved in corn oil, was administered at the desired timepoint via an intraperitoneal injection (Tam-IP) (Dosage: 0.1 mg tamoxifen/g mouse weight).

3.2.2 Euthanasia

At the endpoint of an experiment, a lethal dose of pentobarbital sodium was administered to animals via IP injection (Dosage: 0.4 mg pentobarbital/g mouse weight). After breathing ceased and a lack of pupil response to light was observed, cervical dislocation was performed to ensure death. Embryos were then harvested and briefly kept in PBS on ice before lung dissection.

3.3 Embryonic lung dissection

After harvesting, embryos were placed in PBS and lungs were dissected under a stereomicroscope as detailed in Jones and Bellusci (2019). First, embryos were placed in PBS in a petri dish, and tails were removed for genotyping. Working with fine-tipped forceps and dissecting scissors, lungs were very carefully and gently extracted from the chest cavity to avoid any tissue damage. As required, lungs were similarly positioned in the petri dish in the PBS and were imaged at different magnifications. Whole lungs were used for FACS analyses, while left lobes were taken for RNA isolation and qPCR, and right lobes were processed for paraffin embedding.

3.4 DNA isolation and PCR

DNA was isolated from embryonic tails by placing the tissue in 200 µl of DirectPCR lysis reagent (Viagen) + 2 µl proteinase K and incubating the samples overnight in a thermomixer set to 56°C and 400 rpm. The proteinase K was then heat inactivated at 85°C for 45 minutes.

Gene-specific primers were used to detect genes of interest through polymerase chain reaction (PCR) (Table 1). PCR reaction mixes were calculated for 20 µl per reaction and included 10 µl 2xTaq PCR Master Mix (Qiagen), primers at a final concentration of 0.2 µM, Rnase-free water, and up to 1 µg of genomic DNA. PCRs were performed in a C1000 Thermocycler (Bio-Rad). Cycling steps were optimized for each gene of interest, but generally followed a standard protocol: Initial denaturation for 3 min. at 94°C, between 25-35 cycles of a 3-stage program involving a denaturation step for 1 min. at 94°C, an annealing step for 1 min. at 50-68°C, and an extension step for 1 min. at 72°C. A final extension step was included

for each protocol for 10 min. at 72°C. PCR products were detected using a QIAxcel Advanced capillary gel electrophoresis machine (Qiagen).

Table 1: Primers for genotyping transgenic (Tg) and wildtype (WT) genomic sequences

Gene	Tg – Forward	Tg – Reverse	WT – Forward	WT – Reverse	Product size (bp)
Rosa26rtTA flox	GAGTTCTCTGC TGCCTCCTG	CGAGGCGGATA CAAGCAATA	AAGACCGCGAA GAGTTTGTC		Tg – 215 WT – 322
Tet(o)sFgfr2b	CAGGCCAACCA GTCTGCCTGGC	CGTCTGAGCTG TGTGCACCTCC			Tg – 310
Sftpc-CreERT2	CCCAGTCCCTCT CTGAATTTG	CATCGCTCGAC CAGTTTAGTTA	GTTTCTACCGA CCCTGTGAAG		Tg – 1000 WT – 500
Hopx-CreERT2	CGAGGGGATCA GATGAAGAA	CCAAAAGACGG CAATATGGT	GCAGGACAGCA AAACAATGA		Tg – 800 WT – 396
Fgfr2bflox	CTGCCTGGCTC ACTGTCC	CTCAACAGGCA TGCAAATGCAA GGTC			Tg – 480 WT – 380
tdTomatoflox	CTGTTCCTGTAC GGCATGG	GGCATTAAAGA GCGTATCC	CCGAAAATCTG TGGGAAGTC	AAGGGAGCTGC AGTGGAGTA	Tg – 196 WT – 297
Tet(o)caFgfr1	GGCGTGTACGG TGGGAGGCCTA TATAAGC	GAACGCCTCTG TGGAGACACGC GCGGCTCC			Tg – 325

3.5 RNA isolation and RT-qPCR

Isolated embryonic left lobes used for total RNA isolation were put in 700 µl QIAzol Lysis Reagent (Qiagen). For tissue disruption and homogenization, the samples were transferred to gentleMACS M Tubes and homogenized in a gentleMACS Dissociator (Miltenyi Biotec) for one minute. Total RNA was isolated using the miRNeasy Mini Kit (Qiagen), according to the manufacturer's instructions, and eluted in 30 µl Rnase-free water. RNA amount and purity was assessed using a NanoDrop 2000c spectrophotometer (Peqlab). Up to 1 µg of total RNA for each sample was then reverse transcribed using the QuantiTect Reverse Transcription Kit (Qiagen), according to the manufacturer's instructions.

Primers were designed to amplify specific mature mRNAs using NCBI's primer-BLAST option (https://www.ncbi.nlm.nih.gov/tools/primer-blast/) (Table 2).

Table 2: qPCR primers

Gene	Forward	Reverse	Product size (bp)
Fgfr2b	CCTACCTCAAGGTCCTGAAGC	CATCCATCTCCGTCACATTG	84
Sftpa1	CAGTGTGATTGGGAGAAACCA	ATGCCAGCAACAACAGTCAA	88
Sftpb	GGCTAGACAGGCAAAAGTGTG	GACCGCGTTCTCAGAGGTG	171
Etv4	AGGAGTACCATGACCCCCTG	GGACATCTGAGTCGTAGGCG	138
Etv5	TAGCTGAAGCACAAGTTCCTGA	GCAGCTCCCGTTTGATCTTG	105
Sox2	TCCAAAAACTAATCACAACAATCG	GAAGTGCAATTGGGATGAAAA	73
Sox9	AGTCGGTGAAGAACGGACAA	CTGAGATTGCCCAGAGTGC	158
Sftpc	GGTCCTGATGGAGAGTCCAC	GATGAGAAGGCGTTTGAGGT	94
Aqp5	TAACCTGGCCGTCAATGC	GCCAGCTGGAAAGTCAAGAT	84
Scgb1a1	GATCGCCATCACAATCACTG	CAGATGTCCGAAGAAGCTGA	66
Hprt	TCCTCCTCAGACCGCTTTTT	ATCATCGCTAATCACGACGC	82

qPCR reaction mixtures were set up using the PowerUp SYBR Green Master Mix (Thermo Fisher), with a final volume of 20 µl for each reaction. Samples were run with two or three technical replicates on a LightCycler 480II using the following protocol: UDG activation at 50°C for 2 minutes; DNA polymerase activation at 95°C for 2 minutes; and 40 cycles of denaturation at 95°C for 15 seconds, annealing at 60°C for 15 seconds, and extension at 72°C for 1 minute. To validate amplification specificity, a dissociation step was also included for each sample. Threshold cycles (Ct) were calculated and used for relative expression analyses, using mouse Hprt as the reference gene.

3.6 Microarray

Differential gene expression was determined from total RNA using microarray analyses. For total RNA concentrations greater than 50 ng/µl, the T7-protocol was followed. In this protocol, purified total RNA was amplified and Cy3-labelled using the LIRAK kit (Agilent Technologies) following the kit instructions. Per reaction, 200 ng of total RNA was used. The Cy3-labelled

aRNA was hybridized overnight to 8 x 60K 60mer oligonucleotide spotted microarray slides (Agilent Technologies, design ID 028005).

For experiments where samples yielded less than 50 ng/µl of RNA, the SPIA-protocol was utilized. In this protocol, purified total RNA was amplified using the Ovation PicoSL WTA System V2 kit (NuGEN Technologies). Per sample, 2µg amplified cDNA was Cy-labelled using the SureTag DNA labeling kit (Agilent Technologies). The Cy3-labelled aRNA was hybridized overnight to 8 x 60K 60mer oligonucleotide spotted microarray slides (Agilent Technologies, design ID 074809).

For each protocol, hybridization, washing and drying of the slides followed the Agilent hybridization procedure. The dried slides were scanned at 2 µm/pixel resolution using the InnoScan is900 (Innopsys). Image analysis was performed with Mapix 6.5.0 software, and calculated values for all spots were saved as GenePix results files. Stored data were evaluated using the R software (version 3.3.2) (Andy Bunn, 2017) and the limma package (version 3.30.13) from BioConductor (Ritchie et al., 2015). Gene annotation was supplemented by NCBI gene IDs via biomaRt.

3.7 Fluorescence-activated cell sorting (FACS)

To isolate alveolar cells from whole lung homogenate, embryonic lungs were first isolated in ice-cold Hank's balanced salt solution (HBSS), and then were finely chopped with a sterile razor blade on a glass plate. The tissue was added to a falcon tube and digested in 0.5% collagenase type IV at 37°C for 45 mins., with constant mixing. Single-cell suspensions were made by successively flushing the samples through 18 g, 20 g and 24 g grade needles and then filtering the samples through 70 µm and 40 µm nylon strainers. The cell suspensions were diluted with 5 mL HBSS and centrifuged at 12000 rpm for 5 min. and the supernatant was discarded. The pellet was resuspended in 10 µL blocking buffer and the following antibodies were added: 488-CD31 (1:50); FITC-CD45 (1:50); Apc Cy7 EpCAM (1:50); Apc-Podoplanin (PDPN) (1:20); and Apc Isotype Control (1:20) (all from Biolegend), for 20 min. at 4°C. The samples were washed 2x with 100 µL FACS buffer and centrifuged at 12,000 rpm for 5 min. at

4°C. The supernatant was discarded. The pellet was resuspended in 100 µL FACS buffer. Cell sorting and isolation were performed using the FACSAria™ III (BD Biosciences) cell sorter. Alveolar epithelial cells were identified as CD45-/CD31-/EpCAM+, AT1 cells as CD45-/CD31-/EpCAM+/PDPN+, AT2 as CD45-/CD31-/EpCAM+/PDPN-, and mesenchymal cells as CD45-/CD31-/EpCAM-. Cells were sorted through a flow chamber with a 100-µm nozzle tip under 25 psi sheath fluid pressure. Isolated cells were used for RNA isolation. As a main criterion for gating, we used the settings to capture 98% of the cells in the isotype control and then we applied these gating conditions to the stained cells.

To isolate RFP-labelled alveolar cells, dissected lungs were dissociated as described above before being passed serially through 100-, 70- and 40-µm cell strainers to make single-cell suspensions (BD Biosciences). Red blood cells were eliminated using RBC lysis buffer (Sigma-Aldrich), according to the manufacturer's protocol. Cells were then pelleted and resuspended in FACS buffer (0.1% sodium azide, 5% fetal calf serum (FCS), 0,05% in PBS) before being stained with antibodies (all from Biolegend): anti-EpCAM (APC-Cy7-conjugated, 1:50), CD49F (APC-conjugated, 1:50), and anti-PDPN (FITC-conjugated, 1:20) for 20 minutes on ice in the dark, followed by washing. Next, cells were washed and stained with SYTOX (Invitrogen) according to the manufacturer's instructions, to eliminate dead cells. Finally, flow cytometry and cell sorting were conducted using a FACSAria III cell sorter (BD Biosciences). Data were analyzed using FlowJo software version X (FlowJo, LLC).

3.8 Immunofluorescence

Freshly dissected right lung lobes were washed briefly in sterile PBS, then fixed in 4% PFA for 20 mins. (E12.5 lungs) to 4 hours (E18.5 lungs) at 4°C, and then washed again in PBS (3 X 5 minutes). Lungs were dehydrated by successive washes in a graded ethanol series (30%, 50%, 70%, 100%, 100%) for 5 minutes each, and then stored in 100% ethanol at -20°C until further processing.

For paraffin embedding, lungs were washed in Xylol (3 X 5 minutes, or until clear), incubated for 1 hour at 60°C in a 1:1 Xylol/paraffin mixture, washed in pure paraffin (3 X 20 minutes) at

60°C, and then stored in pure paraffin overnight at 60°C. Lungs were then embedded in paraffin blocks and sectioned using a Microtome to a thickness of 3-5 µm. Sections were placed in a 40°C water bath for approximately 30 minutes, and then placed on glass slides and incubated at 37°C overnight.

Before antibody staining, sections were first washed with gentle shaking in Xylol (3 X 10 minutes), and then in serial dilutions of ethanol (100%, 70%, 50%, and 30%) for 3 minutes each, and finally in distilled water for 5 minutes. For some stains, an antigen unmasking step was performed, which involved incubating the slides in 100°C citrate buffer (pH 6.0) for 15 minutes and then cooling on ice for approximately 30 minutes until room temperature was reached. Sections were then washed with PBST (1x PBS + 0.1% TWEEN20) (3 X 5 minutes). Blocking solution (1x PBS + 3% bovine serum albumin (BSA) + 5% goat serum (GS) + 0.4% TritonX) was then added atop each section for 1 hour at room temperature. Primary antibodies were added to incubation buffer (1x PBS + 1.5% BSA + 2.5% GS + 0.2% TritonX) and samples were incubated overnight at 4°C. Following primary antibody incubation, samples were washed in PBST (3 X 5 minutes), and secondary antibodies were added for 1 hour at room temperature, in the dark. Table 3 lists antibodies used, as well as their dilutions. Samples were washed in PBST (3 X 10 minutes) and PBS for 5 minutes, with gentle shaking. Finally, ProLong Gold antifade reagent with DAPI (Invitrogen) was added to each section and covered with a glass coverslip.

To assess the morphology of intact distal lung buds in control and experimental embryos, whole mount immunofluorescence was performed. E12.5 lungs were dissected and fixed in 4% PFA for 20 minutes on ice. Samples were washed in PBS + 1% TritonX (3 X 10 minutes) and incubated in blocking buffer (1x PBS + 1% TritonX + 10% FBS) for 1.5 hours at room temperature, followed by two washes in blocking buffer. Samples were then incubated for 2 hours with FITC-conjugated anti-CDH1 diluted in 1/4 blocking buffer and PBS, at 4°C in the dark. Lungs were then washed in PBS (3 X 10 minutes) and transferred to custom made imaging dishes (composed of a 35,0/10 mm glass bottom cell culture dish (Greiner Bio-One) and a 10,0/1 mm rubber washer fixed to the middle of the dish with a suitable adhesive, thus

creating an ideal well to mount and image the sample). ProLong Gold antifade reagent with DAPI was added to each well and covered with a glass coverslip.

Table 3: Primary and secondary antibodies used for immunofluorescence staining

Antibody	**Dilution**	**Source**	**Cat. #**
Rabbit polyclonal anti-HOPX	1:200	Atlas antibodies	HPA030180
Rabbit polyclonal anti-proS-PC	1:500	Millipore	AB3786
Mouse/Rat anti-Ki67	1:200	Invitrogen	14-5698-82
Anti-proS-PB	1:500	Abcam	AB40876
Anti-PDPN	1:200	Invitrogen	14-5381-82
Mouse anti-CDH1	1:200	BD Biosciences	610181
Mouse monoclonal anti-CDH1-FITC conjugated	1:200	BD Biosciences	612130
Rabbit polyclonal anti-LAMA1	1:200	Sigma-Aldrich	L9393
Rabbit polyclonal anti-SOX2	1:200	Novus Biologicals	NB 110-37235
Rabbit polyclonal anti-SOX9	1:200	Novus Biologicals	NBP 1-85551
Goat anti-SCGB1A1	1:100	Santa Cruz	sc-9772
Rabbit anti-AQP5	1:200	CalBiochem	178615
Mouse anti-Acetylated a-Tubulin	1:1000	Sigma	T6793
Donkey anti-Mouse Alexa Fluor 555	1:500	Invitrogen	A31570
Donkey anti-Goat IgG Alexa Fluor 488	1:500	Invitrogen	A11055
Rabbit anti-Goat IgG Alexa Fluor 568	1:500	Invitrogen	A11079
Goat anti-Rabbit IgG Alexa Fluor 555	1:500	Invitrogen	A21429
Goat anti-Rabbit IgG Alexa Fluor 488	1:500	Invitrogen	A11034

3.9 Proliferation and apoptosis

Proliferation was assessed either by the Click-iT EdU Imaging Kit (Invitrogen) or Ki67 antibody staining on paraffin sections (1:200 dilution). For the former approach, 5-ethynyl-2'-deoxyuridine (EdU), a nucleoside analogue of thymidine incorporated into DNA during DNA synthesis, was IP-injected two hours before pregnant females were sacrificed (Dosage: 0.005 mg EdU / g mouse weight). Embryonic lungs were harvested, paraffin-embedded, sectioned and placed on glass slides. Sections were then deparaffinized and stained for EdU according to the manufacturer's protocol.

Apoptosis was assessed on paraffin sections via the TdT-mediated dUTP Nick-End Labelling (TUNEL) assay using the DeadEnd Fluorometric TUNEL System (Promega) according to the manufacturer's instructions.

3.10 Microscopy and image acquisition

Brightfield images of lungs from in vivo experiments were captured on a Leica MZ 125 stereoscopic dissecting microscope using a Spot Insight 2.0 Mp Color Mosaic camera and Spot 4.5.9 imaging software.

3.10.1 Immunofluorescent microscopy

Sections were imaged on a Leica DM 5500B upright fluorescent microscope system, with a DFC 360FX camera, and Leica Application Suite Advanced Fluorescence imaging software. Signal intensity was optimized to either a control or experimental sample, and the acquisition and intensity values were similarly applied to each sample in that experiment, thus ensuring valid comparisons.

3.10.2 Confocal microscopy

For imaging of whole mount samples, confocal microscopy was used. Z-stacks of the distal buds of E12.5 lungs were obtained on a Leica TCS SP5 confocal microscopy system using Leica Application Suite X software. For each bud, the first optical section of the z-stack was acquired at the basal edge of the epithelium. Z-stack images were taken at 0.5 µm increments through the bud, until imaging was no longer possible due to complete loss of signal intensity. Compensation of intensity loss through the bud was obtained using the linear compensation by AOTF option. 3-D reconstructions and movies were created using Leica Application Suite X software.

3.10.3 Transmission electron microscopy

Transmission electron microscopy (TEM) was used to identify the effects of FGFR2b ligand inhibition on the ultrastructure of distal epithelial and mesenchymal cells in E12.5 lungs.

Chest cavities of freshly harvested E12.5 embryos were gently opened by incising from the lower abdomen, through the sternum, to just under the chin using a pair of fine dissection scissors. An incision was made along the diaphragm from the midline to the spine. The embryos were then immediately placed, ventral side up, in an immersion fixative solution containing 4% PFA + 2% sucrose + 0.05% calcium chloride + 1x PIPES buffer (0.1M, pH 7.4) (Sigma-Aldrich) in a 50 ml Falcon tube, such that each sample was immersed in 5X the volume of fixative in its own tube. Tubes were placed on ice and gently shaken for 2 hours, after which the fixative was removed and replaced by 4% PFA + 0.05% glutaraldehyde (GA) (Sigma-Aldrich), 2% sucrose, 0.05% calcium chloride + 1X PIPES buffer (0.1M, pH 7.4). Samples remained in this fixative overnight at 4°C.

The next morning, the samples were processed for routine transmission electron microscopy. Briefly, the fixed lungs were dissected and placed into molten agar, which was allowed to harden before the samples were cut longitudinally in half. Each half was fixed for 30 minutes in 1.5% GA fixative containing 2% sucrose + 0.05% calcium chloride + 1X PIPES buffer (0.1M, pH 7.4). The fixative solution was then removed, and samples were washed with 1X PIPES (3 X 5 minutes). Samples were then incubated for 1 hour at room temperature in reduced osmium fixation solution containing 0.15% sodium hexacyanoferrate(II) and 2% reduced osmium, then washed very briefly with distilled water, and dehydrated via washes in a graded ethanol series (70%, 80%, 90%, 100%), 3 times 10 minutes each step. Samples were then embedded by immersion in propylene oxide (3 X 5 minutes), in 1:1 propylene oxide:Agar 100 epoxy resin (1 X 30 minutes) following the manufacturer's instructions to produce blocks of medium hardness (Agar Scientific), and finally in pure Agar 100 epoxy resin in a desiccation chamber at room temperature overnight. The Agar 100 resin-penetrated lungs were then flat embedded into fresh Agar 100 resin and polymerized at 60°C for at least 2 days, or until complete polymerization was achieved. Ultrathin sections were then prepared, and

micrographs were obtained using a Zeiss LEO 906 transmission electron microscope equipped with a TRS slow-scan 2K CCD camera and ImageSP software.

3.11 scRNA-seq database mining

3.11.1 Correlating FGFR2b signatures to published E17.5 scRNA-seq data

E17.5 lung scRNA-seq expression data from Frank et al. (2019) was accessed (GEO GSE113320) and the AT1 and AT2 lineages were clustered and displayed on a tSNE plot using the Seurat v2.2 R package pipeline (http://satijalab.org/seurat/), similar to the original paper. FGFR2b gene signature scores were calculated as previously described (Tirosh et al., 2016). Subclustering of cluster 4 (mature AT2s) was performed using the updated Seurat v3. Plots were displayed using UMAP to increase clustering resolution. SCTransform from the Seurat package was used for data normalization and scaling. PCA was followed by UMAP using pc = 30. Clusters were identified using the FindClusters function, with a resolution of 0.5. For the heatmap, the top 50 genes of each subcluster were selected based on the average log10fold changes, and scaled, centered, and normalized expression was displayed. The threshold to identify differentially expressed genes was set to log10fold change = 0.25.

3.11.2 Correlating FGFR2b signatures to published bleomycin-injury scRNA-seq data

For this analysis, the pre-processed data set published in Strunz et al. (2020) was retrieved from the listed GitHub repository (https://github.com/theislab/2019_Strunz) and explored with SCANPY (v1.6.0), as previously described (Wolf et al., 2018). This study assessed the gene expression changes of murine lungs after bleomycin injury at multiple timepoints with Drop-seq. The whole lung data set was further used without modification, whereas the EpCAMpos enriched data set with densely sampled timepoints (days 1–14, 21, 28, 35, 56) was subset to cell types belonging to the alveolar epithelium (AT1, AT2, Krt8 ADI, activated AT2). The principal components and knn graph (n_pcs = 10, n_neighbors = 20) were re-calculated and formed the input for the UMAP algorithm.

To quantify the enrichment of the FGFR2b signatures, a score was calculated using SCANPY's tl.score_genes() on both the whole lung data set and the alveolar epithelium subset. The input

signatures consisted of 42 genes for timepoint E12.5, 76 genes for E14.5 and 48 genes for E16.5. For visual inspection, the three scores were then overlaid onto the UMAP embeddings for both data sets.

3.12 *In situ* hybridization expression data

To assess the expression patterns of genes in embryonic lungs, the online database 'Genepaint', which contains *in situ* hybridization data for many genes expressed in E14.5 lungs, was used (https://gp3.mpg.de/) (last accessed 01-03-2022). The genes significantly downregulated in our E12.5, E14.5 and E16.5 + 9 h experiments were assessed, and the ones which were clearly expressed were chosen for the figures.

3.13 Quantification and statistical analyses

3.13.1 Bud morphometry

Confocal images of E12.5 distal lung buds were used for morphometric quantifications. Lung mesothelium and airways were traced in Adobe Illustrator CS6 (version 16.0.4) to create skeletal outlines. These outlines were exported and lengths and areas were quantified using FIJI (version 2.0.0-rc-68/1.52g) (Schindelin et al., 2012).

Significance was determined by unpaired two-tailed Student´s t-tests on average lengths and areas. All data are presented as mean ± SEM. Values of $p<0.05$ were considered significant.

3.13.2 RT-qPCR expression

ΔCt and ΔΔCt values were calculated according to the following formulas:

$$\Delta Ct = Ct_{reference} - Ct_{gene\ of\ interest}$$

$$\Delta\Delta Ct = Mean\Delta Ct_{experimental} - Mean\Delta Ct_{control}$$

Unpaired two-tailed Student's t-tests were performed on the ΔCt values, which can be assumed to be normally distributed. All data are presented as mean ± SEM. A p-value < 0.05 was considered significant.

3.13.3 Microarray gene expression

Mean spot signals were background corrected with an offset of 1 using the NormExp procedure on the negative control spots. The logarithms of the background-corrected values were quantile-normalized. The normalized values were then averaged for replicate spots per array. From different probes addressing the same NCBI gene ID, the probe showing the maximum average signal intensity over the samples was used in subsequent analyses. Genes were ranked for differential expression using an unpaired two-tailed Student's t-test on a moderated t-statistic, and heatmaps were generated displaying genes according to descending p-values. Gene set tests were done on the ranks of the t-values, using the function 'geneSetTest' in the limma package from BioConductor (Ritchie et al., 2015). Gene sets were either user defined or, for pathway analyses, according to the KEGG database.

3.13.4 FACS quantification

Average flow cytometry values were used for quantifications. Significance was determined by unpaired two-tailed Student's t tests. All data are presented as mean ± SEM. Values of $p < 0.05$ were considered significant. The number of independent samples (n) can be found in the figures.

3.13.5 Quantification of lineage-labelled cells

Immunostained sections from each sample were imaged at 63x. Multiple images (between 7 and 15) of distal alveolar regions were captured per section and exported as TIFF files. Images were processed and analyzed using FIJI (version 2.1.0/1.53c) (Schindelin et al., 2012). First, images were separated into their component colour channels (red, green, and blue). The average background value of each channel was determined and subtracted from the total signal value. Separately, red-positive and green-positive were manually labelled and counted. These fields were then overlaid, and the double positive cells were tallied. Average cell counts

were determined per sample. Unpaired two-tailed Student's t tests were performed on the average values. All data are presented as mean ± SEM.

4 Results

4.1 Validation of the double transgenic mouse model to conditionally inhibit FGFR2b signalling

To inhibit FGFR2b signalling conditionally and globally in the mouse lung during development, we used a 'Tet-On' double transgenic mouse model: *Rosa26$^{rtTA/rtTA}$; tet(o)sFgfr2b/+* (Fig. 8A). In this system, *reverse tetracycline transactivator* (*rtTA*) expression is controlled by the ubiquitous *Rosa26* locus. In the absence of doxycycline (Dox), rtTA protein is inactive, unable to bind to its target *tet-operator* (*tet(o)*) DNA elements (T. Das et al., 2016). However, in the presence of Dox, rtTA binds to *tet(o)*, thereby inducing the expression of a soluble form of FGFR2b (*sFgfr2b*) within minutes of exposure to Dox (Danopoulos et al., 2013). The genetically-engineered sFGFR2b is composed of the mouse FGFR2b extracellular domain and the heavy chain hinge and Fc domain of the mouse immunoglobulin (*Igh*) (Hokuto et al., 2003). Consequently, sFGFR2b is not membrane-bound, and is excreted from expressing cells into the surrounding extracellular matrix. Here, sFGFR2b sequesters all FGFR2b ligands, preventing them from binding to their native FGFR2b receptor on the epithelial surface.

Figure 8B shows the *in vivo* validation of our mouse model. Pregnant mice carrying littermate control (*Rosa26$^{rtTA/rtTA}$; +/+*) and experimental (*Rosa26$^{rtTA/rtTA}$; tet(o)sFgfr2b/+*) embryos were fed Dox-food from different timepoints (E9.5 (data not shown)), E10.5, E11.5, E13.5, and E14.5) and the embryos were harvested, and lungs dissected, at E18.5. Lungs subject to the earliest Dox exposure (E9.5) failed to develop at all, which is reminiscent of the lung agenesis seen in constitutive genetic loss of *Fgf10* or *Fgfr2b* (Sekine et al., 1999; De Moerlooze et al., 2000). The later that Dox was administered to the system, the more normal the lungs developed (compare E10.5 (Fig. 8Bb) to E14.5 (Fig. 8Be)), yet drastic phenotypes were observed at each timepoint. Figure 8C shows the *in vitro* validation of our transgenic approach. While control lungs branched extensively over time (Fig. 8Ca, c, e, g), experimental lungs failed to branch, forming instead long tubular extensions (Fig. 8Cb, d, f, h) similar to that observed *in vivo*. These results provide validation for our transgenic mouse model to conditionally block FGFR2b ligand activity at the protein level, which is functionally equivalent to preventing native FGFR2b signalling.

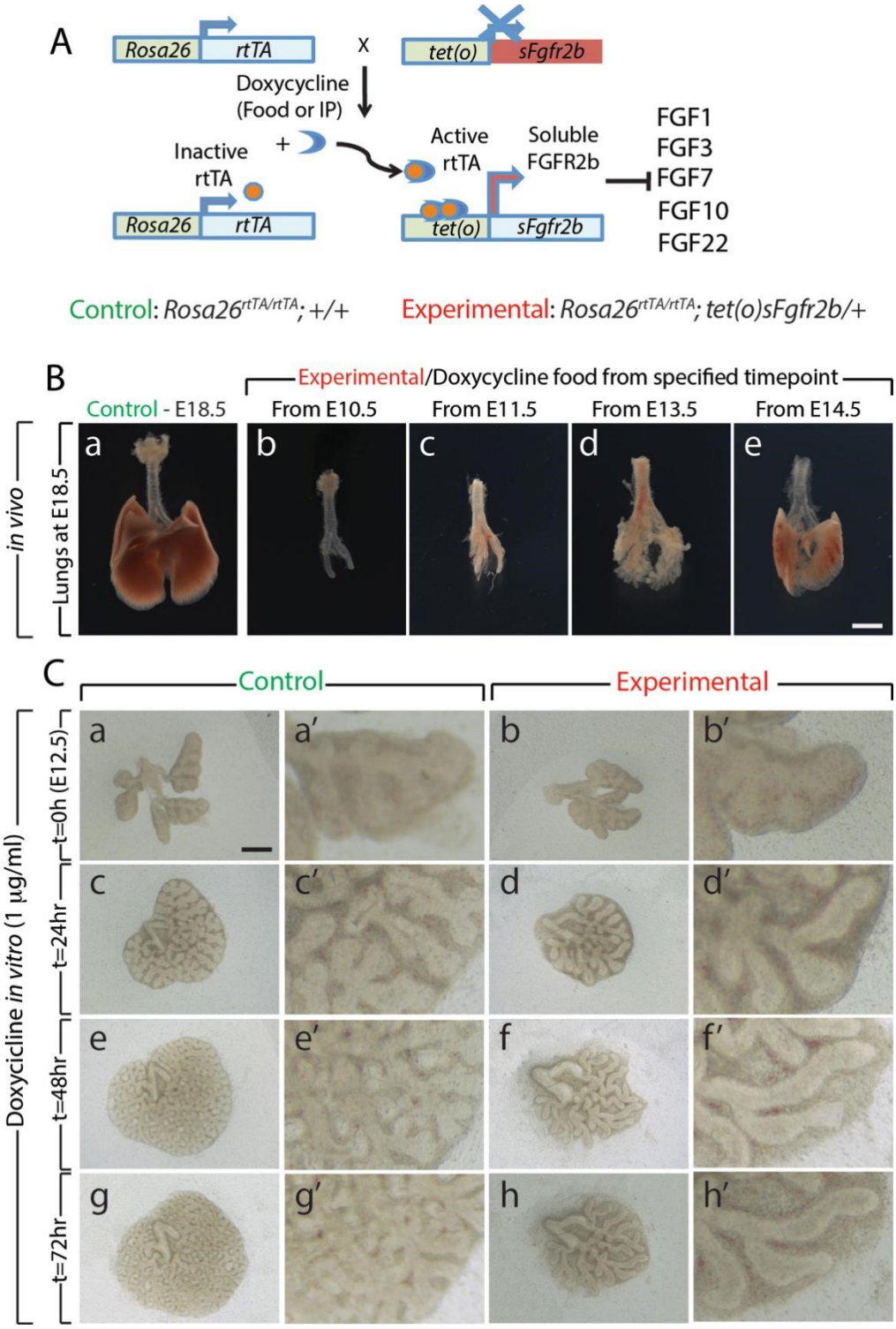

Figure 8 – The *Rosa26*$^{rtTA/rtTA}$*; tet(o)sFgfr2b/+* double transgenic mouse model and experimental validation. (A) The double transgenic mouse model to inhibit FGFR2b signalling: rtTA is ubiquitously produced from the *Rosa26* locus. In the presence of doxycycline, the rtTA becomes active, and binds to the tetracycline operator (*tet*(*o*)) thereby inducing the expression of soluble FGFR2b. Soluble FGFR2b is secreted into the extracellular matrix and sequesters all FGFR2b ligands, preventing them from activating the native FGFR2b receptors.

(B) *In vivo* validation of the mouse model: pregnant females carrying littermate control (*Rosa26$^{rtTA/rtTA}$; +/+)* (a) and experimental *(Rosa26$^{rtTA/rtTA}$; tet(o)sFgfr2b/+)* (b-e) embryos were fed Dox-food starting at E10.5 (b), E11.5 (c), E13.5 (d) or E14.5 I, sacrificed at E18.5, and lungs harvested. *Scale bar:* 500 µm. **(C)** *In vitro* validation: pregnant females carrying control (a,c,e,g and a',c',e',g') and experimental (b,d,f,g and b',d',f',h') embryos were sacrificed at E12.5. The lungs were dissected, cultured in the presence of Dox added to the culture medium, and imaged every 24 hours for three days. *Scale bar:* (a-h) 500 µm; (a'-h') 125 µm. (Figure previously published in Dilai, 2020).

4.2 Embryonic and early pseudoglandular stage (E9-E11)

The results in this section are adapted from Taghizadeh and Jones et al. (2020).

4.2.1 Transient inhibition of FGFR2b signalling at E9 and at E9.5 leads to limb agenesis and lung hypoplasia

Control (*Rosa26r$^{tTA/rtTA}$; +/+*) and experimental (*Rosa26$^{rtTA/rtTA}$; Tg(tet(o)sFgfr2b)/+*) embryos were generated by crossing *Rosa26$^{rtTA/rtTA}$; Tg(tet(o)sFgfr2b)/+* males with *Rosa26$^{rtTA/rtTA}$; +/+* females. Pregnant females were injected intraperitoneally (IP) at E9 with Dox (Fig. 9A). In our experimental conditions, the expression of the soluble form of FGFR2b peaks 6 hours after Dox-IP and lasts for 24 hours. We also reported that the inhibitory activity is reversible after this 24 hour time period (Danopoulos et al., 2013).

FGF10 is the primary FGFR2b ligand expressed in the lung during embryonic and early pseudoglandular development (Cardoso et al., 1997; Jones et al., 2019a). Therefore, our experimental approach effectively leads to the global inhibition of FGF10 activity. Figure 9B displays the phenotypic differences between experimental and control embryos. While the craniofacial features of experimental and control embryos are similar (Fig. 9Ba,e), the limb agenesis in experimental embryos is striking (Fig. 9Bb,f). This result is unsurprising: FGF10 signalling is vital for the induction of the apical ectodermal ridge (AER) in the limb rudiment at E9.5 and E10 in the forelimb and hindlimb, respectively (Jin et al., 2019). Therefore, the limb agenesis phenotype observed represents an excellent validation that the induced expression of soluble FGFR2b is translated into a functional inhibition of FGFR2b signalling.

Interestingly, experimental lungs were similar in gross morphology to controls (Fig. 9Bc-h), except for the absence of lobar septations in the right lobe, which prevented the separation of the caudal, medial and cranial lobes (Fig. 9Bi). qPCR analysis on selected differentiation marker genes indicated no significant differences between the expressions of *Etv4/Etv5* (transcription factors regulating epithelial differentiation), *Sox9* (distal epithelial marker), *Sox2* (proximal epithelial marker), *Sftpc* (alveolar cell type 2 maker (AT2)) *or Aqp5* (alveolar type 1 (AT1) marker) in control versus experimental lungs (Fig. 9C).

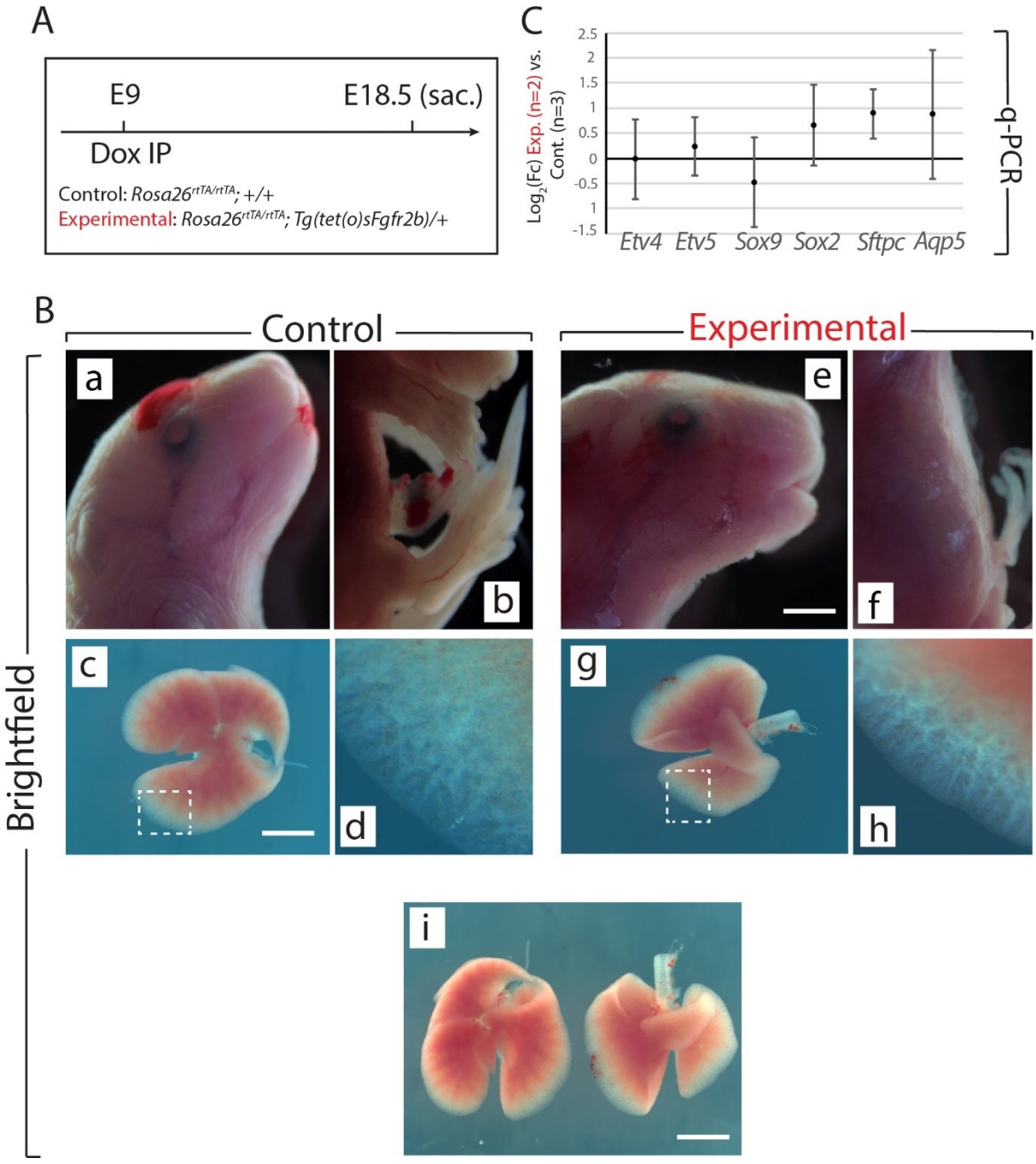

Figure 9 – Transient inhibition of FGFR2b signalling at E9 results in irreversible limb agenesis and defects in lobar septation. (A) Experimental design: females carrying littermate control (*Rosa26$^{rtTA/rtTA}$; +/+*) and experimental (*Rosa26$^{rtTA/rtTA}$; Tg (tet(O)sFgfr2b)/+*) embryos were administered a single Dox-IP at E9, and embryos were harvested at E18.5. **(B)** Comparison of gross morphology between control and experimental embryos: craniofacial (a and e) and limb (b and f) phenotypes; whole lung comparison (c, d and g, h); and side-by-side comparison of a control (left) and experimental lung (i). Scale bar: (a,b,e,f) 2 mm; (c,g,i) 750 µm; (d,h) 150 µm. **(C)** Quantification by qPCR of epithelial differentiation marker expression (*Etv4, Etv5, Sox2, Sox9, Sftpc*, and *Aqp5*) relative to *Hprt.* N = 2 in experimental group and n = 3 in control group.

We further assessed the impacts of FGFR2b signalling on lobar septation by injecting Dox at E9.5 (Fig. 10A) and examined the resulting phenotype at E17. As in the previous experiment, we observed complete limb agenesis in experimental embryos (Fig. 10Ba,f). Macroscopically, experimental lungs were reduced in overall size compared to controls (Fig. 10Bb,e, c, g), while the absence of the accessory lobe and impaired lobar septation in the right lung were evident (Fig. 10Bc,g). The branching morphology of the left lobe, which was reduced in size in experimental versus control lungs, revealed no noticeable differences in branching at this scale (Fig. 10Bd,h). Immunofluorescence antibody staining with CDH1 (E-cadherin; an epithelial specific marker) and SOX9 (a marker for distal epithelium) to determine the status of the distal alveolar progenitors revealed no obvious differences between control and experimental lungs (Figure 10Bk-l). Similar results were obtained with SFTPC, an AT2 marker (Fig. 10Bm-p). These immunofluorescence results were supported by qPCR analysis, which showed no significant differences in the expressions of *Etv5*, *Sox9*, *Sox2*, *Sftpc*, *Aqp5* between experimental and control lungs (Fig. 10C).

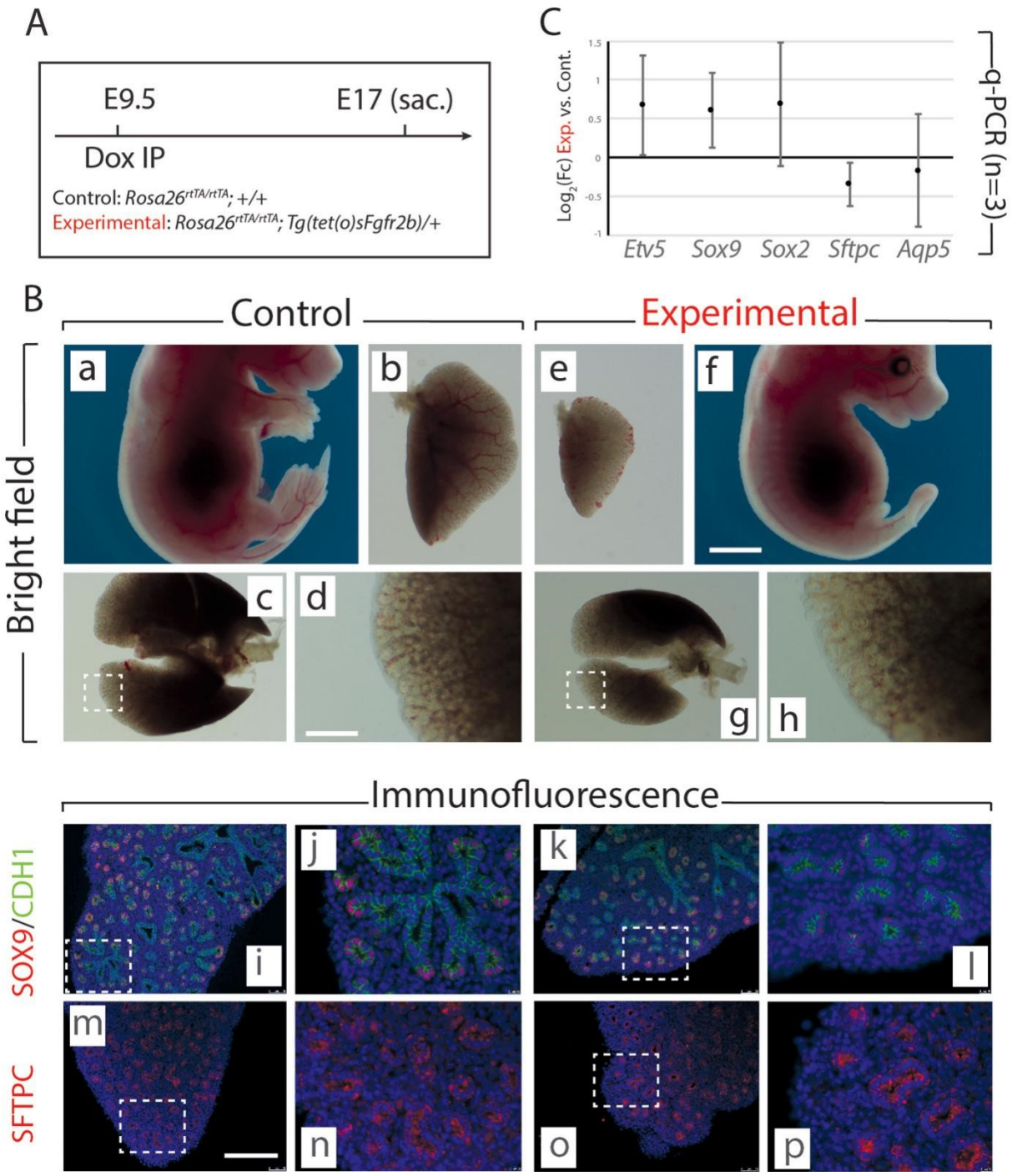

Figure 10 – Inhibition of FGFR2b signalling at E9.5 results in lobar defects but not branching defects. (A) Experimental design: females carrying littermate control (*Rosa26r$^{tTA/rtTA}$; +/+*) and experimental (*Rosa26$^{rtTA/rtTA}$; Tg (tet(O)sFgfr2b)/+*) embryos were administered a single Dox-IP at E9.5, and embryos were harvested at E17. **(B)** Comparison of gross morphology reveals limb agenesis (f vs. a), as well as lung hypoplasia (compare e vs. b and g,h vs. c,d) in experimental vs. control embryos. Immunofluorescence staining for CDH1 and SOX9 (i-l), as well as for SFTPC (m-p) reveals no obvious difference in differentiation status between control and experimental groups. Scale bar: (a,f) 5 mm; (b,e) 500 µm; (c,g) 750 µm; (d,h) 185 µm; (i,k,m,o) 150 µm; (j,l,n,p) 25 µm. **(C)** Quantification by q-PCR of epithelial differentiation marker expression (*Etv5, Sox2, Sox9, Sftpc*, and *Aqp5*) relative to *Hprt*. N = 3 in both groups.

Taken together, our results suggest that during embryonic lung development (E9-E11), FGFR2b signalling is primarily involved in lobar septation and accessory lobe formation.

4.2.2 Transient inhibition of FGFR2b signalling at E11 leads to arrested lung development

Next, we examined at E18.5 the impact of transient FGFR2b inhibition at E11 (Fig. 11A). Macroscopic examination of craniofacial structures revealed incomplete eyelid formation in experimental embryos (see arrow in Fig. 11Bf and a). This phenotype was previously described in *Fgf10*-null embryos, and is a result of impaired proliferation and coordinated migration of the leading epithelial edge-cells of the developing eyelids (Sekine et al., 1999; Tao, 2020). Assessing the limb phenotype revealed that both forelimbs and hindlimbs formed in the experimental embryos (Fig. 11Bg,h). However, the autopods (carpal/tarsal, metacarpal/metatarsal, phalanges) of experimental embryos were truncated (Fig. 11B g,h vs, b,c), a phenotype which was previously described upon inhibition of FGFR2b ligands at E11.5 (Danopoulos et al., 2013). Finally, the gross morphology of experimental embryos clearly showed arrested development, indicating that the impact of FGFR2b inhibition between E11 to E12 was irreversible (Fig. 11Bd vs. I and Fig. 11C). Interestingly, the trachea and primary bronchi developed normally in experimental embryos, which contrasts sharply with the severely underdeveloped right and left lobes (compare Fig. 11Be and j).

Unsurprisingly, if experimental embryos from our E11 Dox-IP experiments would come to term, they would not survive due to their severely underdeveloped lungs. Contrast this to the embryos injected with Dox at E9.5, which, although limbless, are viable and seem to breathe normally (See supplementary movie in Taghizadeh et al., 2020).

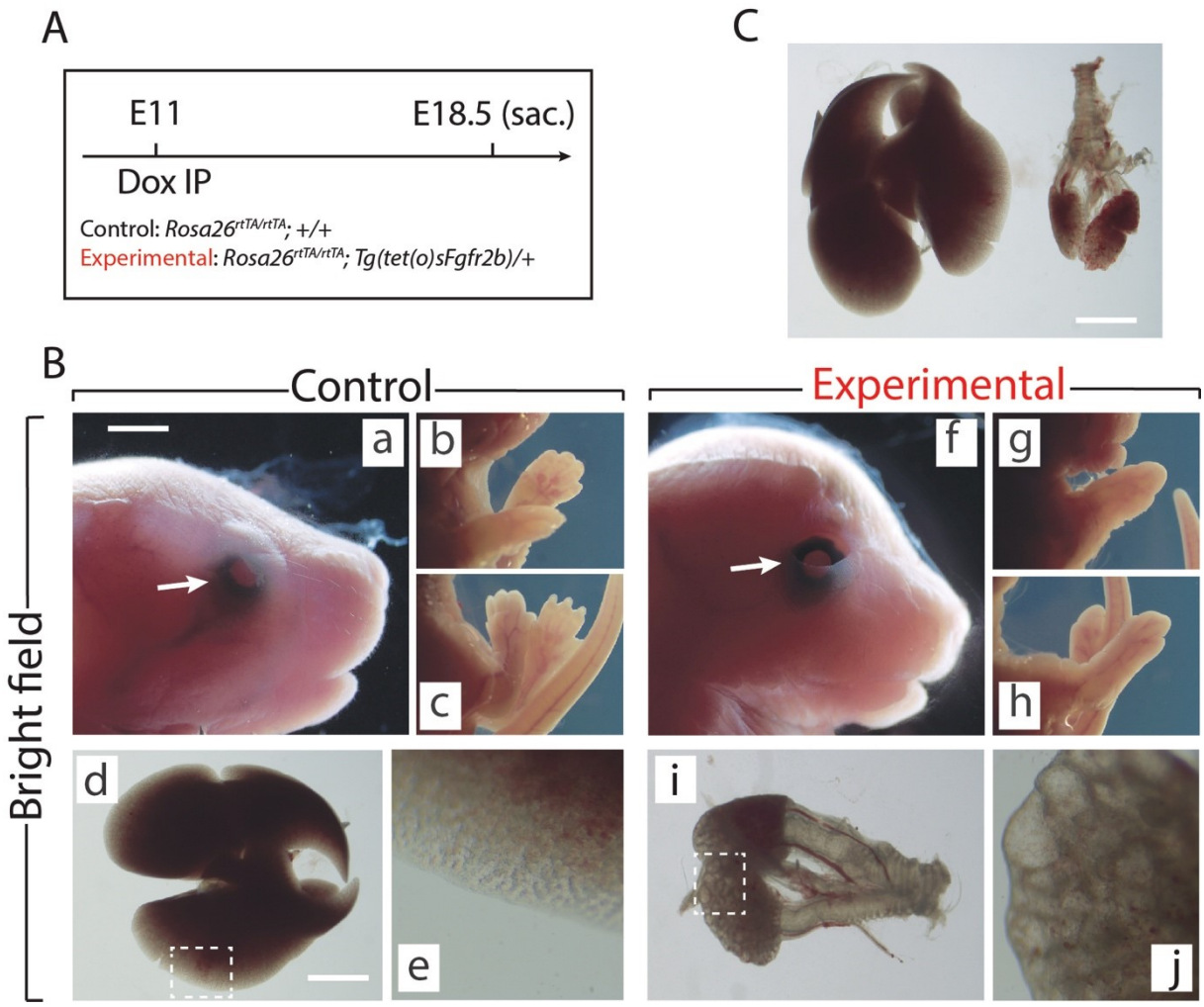

Figure 11 – Transient inhibition of FGFR2b signalling at E11 results in arrested development. **(A)** Experimental design: females carrying littermate control (*Rosa26r$^{tTA/rtTA}$; +/+*) and experimental (*Rosa26$^{rtTA/rtTA}$; Tg (tet(O)sFgfr2b)/+*) embryos were administered a single Dox-IP at E11, and embryos were harvested at E18.5. **(B)** Brightfield images of control (a–e) and experimental embryos (f–j), showing eyelid (a,f), fore- and hindlimb digit (b,c,g,h), and lung (d,e,i,j) defects. Scale bar: (a,f) 2 mm; (b,c,g,h) 5 mm; (d) 750 µm; (i) 375 µm; (e,j) 25 µm. **(C)** Side-by-side comparison of control (left) and experimental lung.

4.3 Early to mid pseudoglandular development (E12.5-E14.5)

The results in this section are adapted from Jones et al. (2019a).

4.3.1 Identification of an FGFR2b target gene signature by gene array

Pseudoglandular lung development in the mouse begins around E10.5. Our results at E11 suggest that transient FGFR2b inhibition at this early stage completely prevents proper lung formation. To assess the potential targets downstream of FGFR2b signalling at this early stage, we chose to look more closely at E12.5 lungs. This timepoint of study has two major advantages: first, the lungs at E12.5 are much larger than at E11, thus allowing easy dissection and the provisioning of adequate biological material to conduct analyses; and second, the primary iterations of branching morphogenesis are clearly established with the distal epithelial tips distinguishable from the proximal airways, thus enabling the demarcation of FGFR2b-responding cells.

To assess direct targets of FGFR2b signalling in E12.5 lungs, we administered single Dox-Ips to pregnant females and isolated embryos 6 or 9 hours later (Fig. 12A). Compared to control lungs (Fig. 12Ba and b), experimental lungs showed branching simplification and an increased distance between the distal epithelium and the mesothelium at 9 hours (Fig. 12Bc and d). A gene array was conducted on RNA isolated from control lungs (n=3, due to minimal phenotypic difference, two controls came from the 6 hrs. timepoint and one from the 9 hrs. timepoint) and from experimental lungs at 6 hours (n=3) and at 9 hours (n=3). Figure 12C shows a heatmap of the top 100 regulated genes (selected according to p-value) between experimental and control lungs at 9 hours, as well as the corresponding expression levels for those genes at 6 hours. Figure 12D lists the highly regulated KEGG pathways from the entire gene array. Note the pathways involved in cell-cell and cell-extracellular matrix adhesion (focal adhesion, ECM-receptor interaction, and cell adhesion molecules) as well as cell migration (regulation of actin cytoskeleton).

Furthermore, genes from the heatmap were grouped into four clusters according to similar expression patterns (expression patterns 1-4) (Fig. 12C). The genes contained in the ‘expression pattern 4’ cluster showed early down-regulation (beginning at 6 hrs.) after attenuation of FGFR2b signalling, and their expressions continued to decrease over time. These genes are predominantly epithelial specific, and therefore constitute the ‘FGFR2b gene signature’ of potential direct transcriptional targets of FGFR2b signalling at E12.5 (Fig. 12E).

To internally validate our experimental model, we looked for the regulation of genes involved in the canonical FGF10-SHH regulatory feedback loop (see references in 'Introduction'). Recall that in this loop, FGF10 expressed in the mesenchyme signals to the epithelium through FGFR2b, which leads to the upregulation of the transcription factors ETV4/ETV5. These in turn upregulate the expression of *Sonic hedgehog* (*Shh*), which encodes a secreted growth factor, SHH (Herriges et al., 2015). SHH signals back to the mesenchyme resulting in the upregulation of specific genes, including *Foxl1*, *Foxf1*, *Gli1*, and *Ptch2*, as well as the downregulation of *Fgf10* (Bellusci et al., 1997; Lebeche et al., 1999). Our FGFR2b signature contains the downregulation of *Etv5* and *Shh* (Fig. 12E). As Figure 12F shows, genes belonging to the clusters regulated later in our array perfectly reflect what one would expect downstream of reduced SHH expression: genes in 'expression pattern 3' are downregulated in our array at 9 hrs., and contain the SHH signalling-specific genes *Foxl1*, *Foxf1*, *Gli1*, and *Ptch2*; while the 'expression pattern 1' cluster shows the upregulation of genes 9 hrs. after FGFR2b signalling inhibition, including *Fgf10*, which is expected given the downregulation of the SHH regulatory mechanism. Taken together, this evidence functionally validates our gene array, and supports the model proposed in Figure 12G.

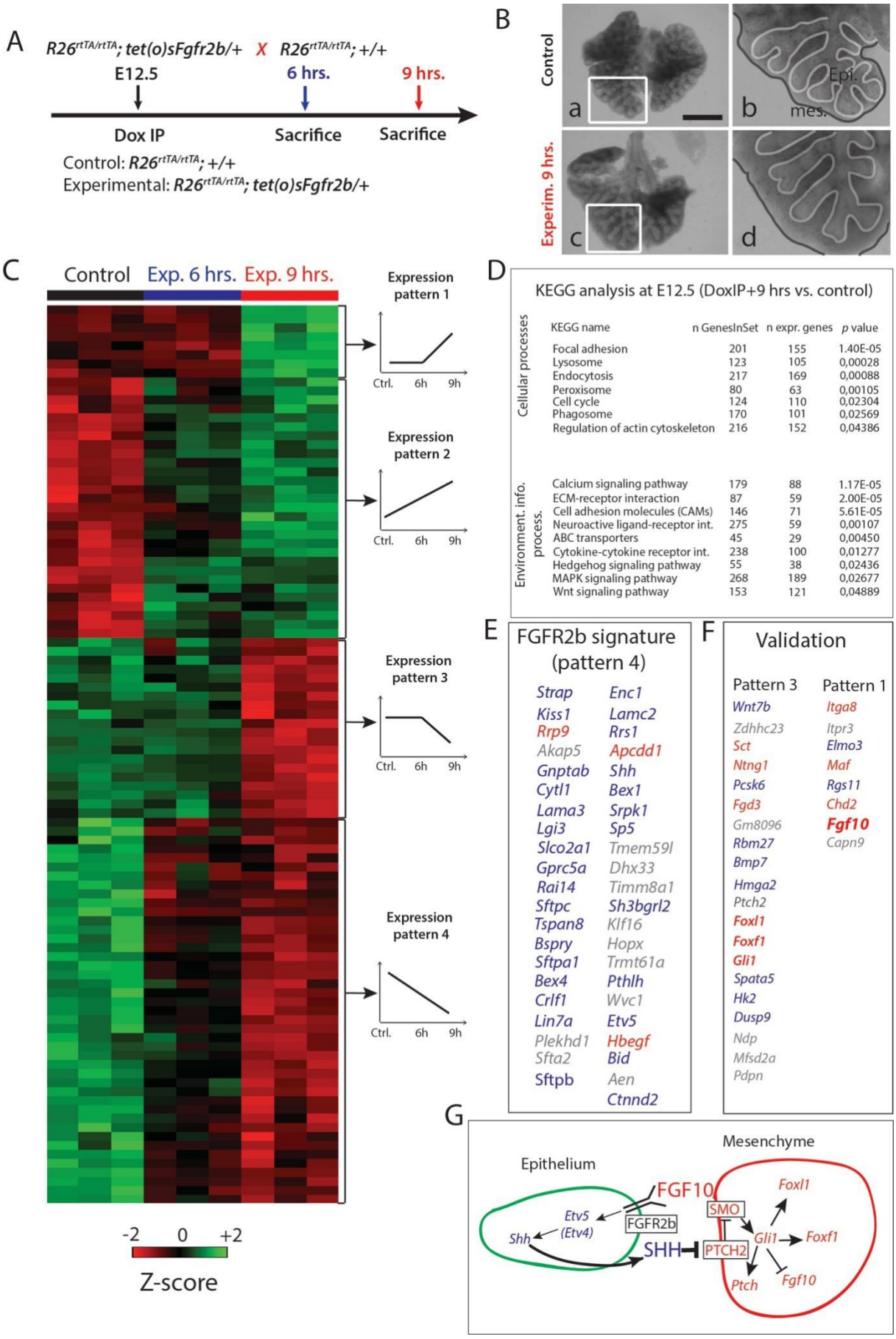
A
R26rtTA/rtTA; tet(o)sFgfr2b/+ X R26rtTA/rtTA; +/+
E12.5
6 hrs.
9 hrs.
Dox IP
Sacrifice
Sacrifice
Control: R26rtTA/rtTA; +/+
Experimental: R26rtTA/rtTA; tet(o)sFgfr2b/+
B
Control
Experim. 9 hrs.
a
b
c
d
Epi.
mes.
C
Control
Exp. 6 hrs.
Exp. 9 hrs.
Expression pattern 1
Expression pattern 2
Expression pattern 3
Expression pattern 4
Ctrl.
6h
9h
-2
0
+2
Z-score
D
KEGG analysis at E12.5 (DoxIP+9 hrs vs. control)
Cellular processes
Environment. info. process.
KEGG name | n GenesInSet | n expr. genes | p value
Focal adhesion 201 155 1.40E-05
Lysosome 123 105 0,00028
Endocytosis 217 169 0,00088
Peroxisome 80 63 0,00105
Cell cycle 124 110 0,02304
Phagosome 170 101 0,02569
Regulation of actin cytoskeleton 216 152 0,04386
Calcium signaling pathway 179 88 1.17E-05
ECM-receptor interaction 87 59 2.00E-05
Cell adhesion molecules (CAMs) 146 71 5.61E-05
Neuroactive ligand-receptor int. 275 59 0,00107
ABC transporters 45 29 0,00450
Cytokine-cytokine receptor int. 238 100 0,01277
Hedgehog signaling pathway 55 38 0,02436
MAPK signaling pathway 268 189 0,02677
Wnt signaling pathway 153 121 0,04889
E
FGFR2b signature (pattern 4)
Strap
Kiss1
Rrp9
Akap5
Gnptab
Cytl1
Lama3
Lgi3
Slco2a1
Gprc5a
Rai14
Sftpc
Tspan8
Bspry
Sftpa1
Bex4
Crlf1
Lin7a
Plekhd1
Sfta2
Sftpb
Enc1
Lamc2
Rrs1
Apcdd1
Shh
Bex1
Srpk1
Sp5
Tmem59l
Dhx33
Timm8a1
Sh3bgrl2
Klf16
Hopx
Trmt61a
Pthlh
Wvc1
Etv5
Hbegf
Bid
Aen
Ctnnd2
F
Validation
Pattern 3
Wnt7b
Zdhhc23
Sct
Ntng1
Pcsk6
Fgd3
Gm8096
Rbm27
Bmp7
Hmga2
Ptch2
Foxl1
Foxf1
Gli1
Spata5
Hk2
Dusp9
Ndp
Mfsd2a
Pdpn
Pattern 1
Itga8
Itpr3
Elmo3
Maf
Rgs11
Chd2
Fgf10
Capn9
G
Mesenchyme
Epithelium
FGF10
Foxl1
Etv5
(Etv4)
Shh
FGFR2b
SMO
Gli1
Foxf1
SHH
PTCH2
Ptch
Fgf10

Figure 12 – Identification of an FGFR2b gene signature by a gene array approach. (A) E12.5 littermate control and experimental lungs were collected 6 hrs. or 9 hrs. after a single Dox-IP injection to pregnant females. **(B)** FGFR2b signalling attenuation leads to visible branching defects at Dox-IP+9 hours (increased mesothelial-epithelial distance and branching inhibition). Meso.=Mesothelium; Epi.=Epithelium. *Scale bar:* (a, c) 500 µm; (b, d) 175 µm. **(C)** Heatmap of the top 100 genes (based on p-value) differentially expressed at the 9 hrs. timepoint between experimental and control lungs. Four clusters of genes can be grouped according to expression pattern (Patterns 1-4). **(D)** KEGG results for experimental vs. control lungs. **I** Genes identified in the 'pattern 4' cluster comprise the FGFR2b gene signature at E12.5. These genes are downregulated beginning at 6 hrs. and are increasingly repressed up to 9 hrs. after FGFR2b signalling inhibition. Genes in blue are epithelial specific, those in red are specific to the mesenchyme, while those in grey are equally present in both cellular compartments according to (Jones et al., 2019a). **(F and G)** Validation of the gene array approach: specific genes in the 'pattern 3' and 'pattern 1' clusters are involved in the canonical FGF10-FGFR2b-ETV4/5-SHH regulatory feedback loop. These clusters are not regulated significantly at 6 hrs., but are at 9 hrs., likely in response to the transcriptional regulation of the FGFR2b 'pattern 4' signature genes. See text for more details.

4.3.2 Inhibition of FGFR2b activity reduces distal epithelial bud lumen area associated with cell rearrangements

Next, we analysed the branching defects at the cellular level using 3D-reconstructions of serial confocal images of distal epithelial buds in control and experimental lungs. These lungs were isolated 9 hours following a Dox-IP to pregnant females carrying E12.5 embryos and were whole-mount stained with CDH1 (E-cadherin) antibody. Figure 13A shows a longitudinal section, cross section, and 3D projection of control (a, c, e) and experimental (b, d, f) buds. Quantification of the relative lumen area at different positions within the bud shows a clear reduction in this ratio in experimental buds, compared to controls (n=3; Fig. 13B). In addition, the average epithelial thickness was larger in experimental buds, compared to controls (Fig. 13B). This increased thickness was likely a consequence of epithelial cells piling atop one another, and failing to form an ordered monolayer, as seen in control buds. Altogether, inhibition of FGFR2b activity led to the collapse of the lumen within the bud, and to increased epithelial thickness, which we think are the consequences of cell rearrangements within the epithelial layer. This conclusion is supported by the fact that extensive analysis of cell proliferation and cell death in the epithelium and mesenchyme, at this timepoint, did not indicate any difference between control and experimental lungs (n=3; Fig. S1).

We also analysed the appearance of epithelial tip cells in control and experimental lungs by transmission electron microscopy (TEM) (Fig. 13C). Our results reveal numerous impacts on cell ultrastructure in experimental samples, including altered Golgi morphology, decreased microvilli size and number, and opened tight junctions (see Fig. S2). In terms of impacts on cell rearrangement, in experimental lungs, the thickness of the basement membrane was consistently greater than that of control lungs (see dashed line in Figure 13Cb and d). This increase in basement membrane thickness was confirmed by immunofluorescence for laminin (LAMA1) (Fig. 13De-h). Second, epithelial cell-cell adhesion was affected in experimental lungs, compared to controls. This is evidenced by the many large gaps between adjacent epithelial cells in experimental lungs (see the asterisks in Figure 13Cc and d), whereas adjacent epithelial cells in control samples formed tight associations with few gaps. Impacts on adhesion are further demonstrated by looking at the adherens junctions, where a darker staining was observed in experimental lungs, compared to controls (Fig. 13Ce-h). This darker staining suggests an accumulation of adherens junction associated protein, including CDH1. Indeed, immunofluorescent staining revealed drastically increased CDH1 expression in the distal epithelium of experimental lungs versus controls (Fig. 13Da-d).

Our results demonstrate that inhibition of FGFR2b signalling leads to impaired distal bud morphology, including collapsed bud lumens and thicker epithelial layers. It is likely that this phenotype is primarily a result of epithelial disorganization caused by adhesion and rearrangement defects.

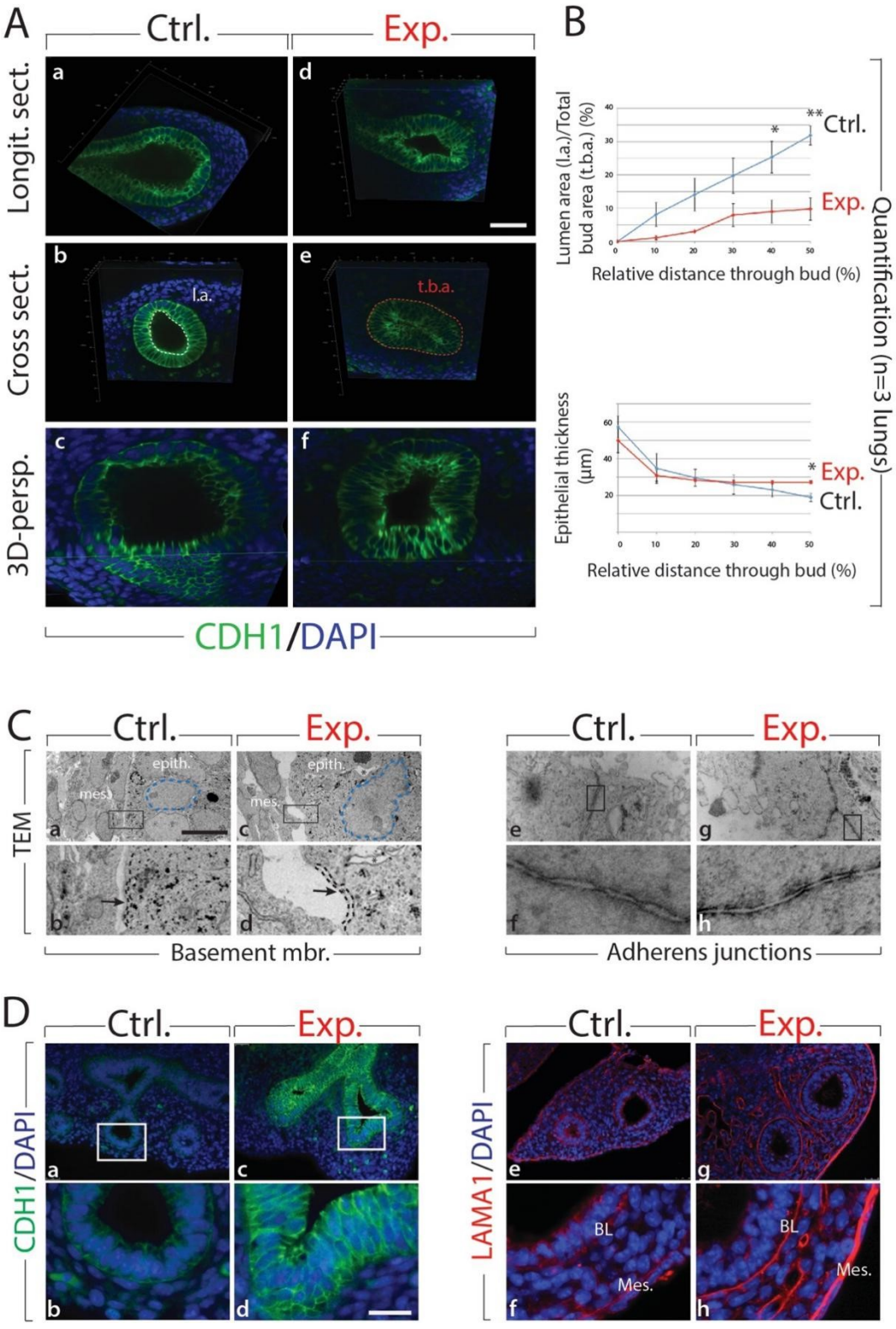

Figure 13 – Inhibition of FGFR2b signalling for 9 hours in E12.5 lungs leads to collapse of the epithelial bud associated with cell rearrangements and altered cell-cell adhesion. (A) Whole-mount confocal images of distal lung buds. Control buds show open lumens and an ordered epithelial monolayer (a-c), while experimental lung buds show collapsed lumens associated with multi-layered epithelium (d-f). Please note that due to our fluorescence acquisition

requirements, the intensity of the signal cannot be compared between control and experimental samples. L.a.=lumen area; t.b.a.=total bud area. *Scale bar:* (a, b, d, e) 40 µm; (c, f) 16 µm. **(B)** Quantification of relative lumen area (l.a./t.b.a.) and epithelial thickness. (n=3; *p-value < 0.05, **p-value < 0.01). **(C)** TEM of distal lung buds highlighting the thickened basement membrane (black dashed line and arrows; a-d) and the darker staining around the adherens junctions (arrows; e-h) in experimental vs. control lungs. Note also the enlarged and irregularly shaped nuclei (blue dashed line; a and c) and the gaps between adjacent epithelial cells (asterisk; c and d) in experimental vs. control lungs. Mes.=mesenchyme; epith.=epithelium. *Magnification:* (a, c) 7750x; (e, g) 27800x; (b, d) 38750x; (f, h) 139000x. **(D)** Immunofluorescent staining for E-cadherin (CDH1) and laminin (LAMA1). E-cadherin shows increased expression in experimental lungs (c, d) compared to controls (a, b). Laminin deposition is increased in the basal lamina and mesothelium (Meso.) in experimental (g, h) vs. control lungs (e, f). *Scale bar:* (a, c) 75µm; (b, d) 19 µm.

4.3.3 FGFR2b signalling is required to maintain the differentiation status of the epithelial multipotent progenitors

Next, we examined the impact of attenuated FGFR2b signalling on the differentiation of the multipotent epithelial progenitor cells. Figure 14A confirms the reduced expression of SOX9 distally in experimental (d-f) vs. control (a-c) lungs at 9 hours post Dox-IP. In control lungs, SOX2 expression in the proximal epithelium established a clear boundary between proximal and distal regions (Fig. 14Ag-i). However, in experimental lungs, SOX2 expression in the proximal epithelium expanded more distally, showing a salt and pepper expression pattern with increased expression in the mesenchyme around the conducting airway (Fig. 14A; j-l).

Until recently, the close examination of epithelial tip cell differentiation was limited, as only a few signature genes denoting differentiation status were known to be expressed in those cells. However, this limitation has been overcome after the paradigm-shifting paper by Treutlein et al. (2014) published gene signatures for the AT1 and AT2 cell lineages. In order to probe more extensively the status of these differentiation marker genes in E12.5 epithelial tip cells, we assessed the AT1 and AT2 signatures from our gene array (experimental vs. control) at the 9 hours' timepoint. Figure 14B shows a clear global reduction in the markers characteristic of the AT2 signature, with minimal change in the AT1 signature. Gene set analysis confirms a highly significant difference in the AT2 signature in experimental vs. control lungs (n=3; p=0.000004). No significant change was observed in the AT1 signature. We therefore conclude

that upon inhibition of FGF ligands, the tip epithelial cells, which include the progenitors for the alveolar lineages, lose expression of the markers characteristic of the AT2 signature, and that globally the expression of these genes is under the control of FGFR2b signalling.

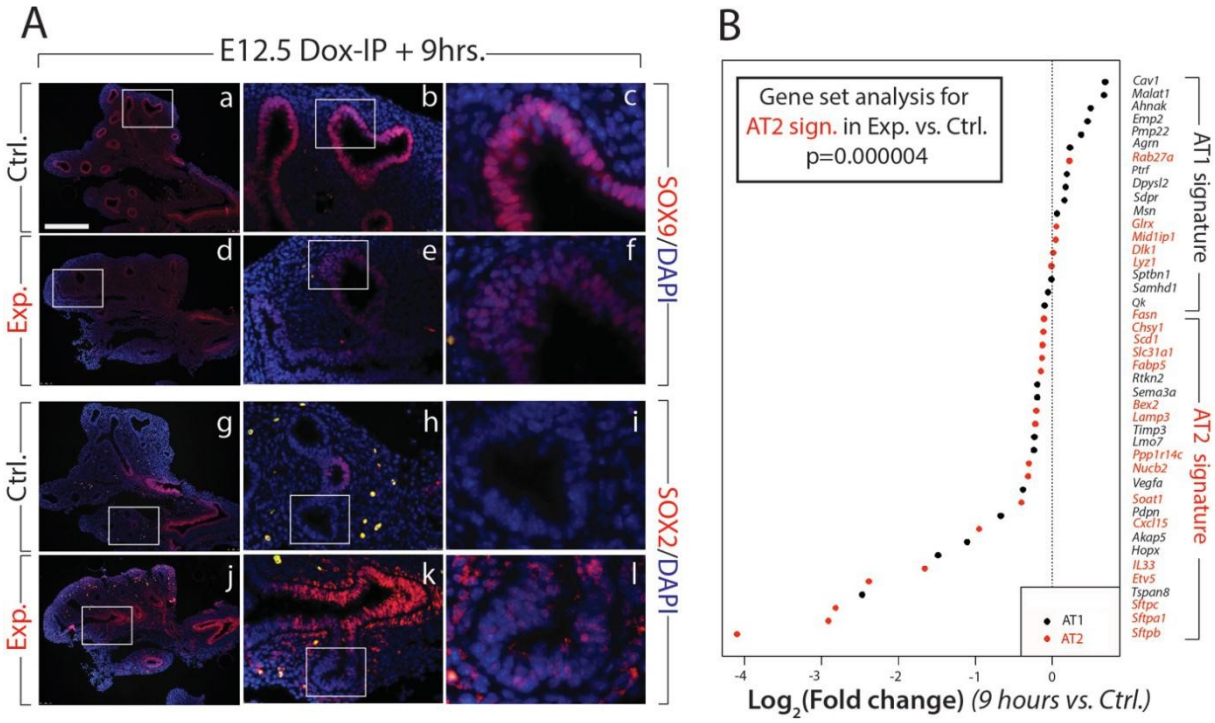

Figure 14 – Impacts of FGFR2b signalling at E12.5 on epithelial differentiation. (A) Changes in SOX9 (a-f) and SOX2 (g-l) protein expression in experimental vs. control lungs. *Scale bar:* (a, d, g, j) 300 µm; (b, e, h, k) 100 µm; (c, f, i, l) 33 µm. **(B)** Expression of AT1 and AT2 markers in 9 hours vs. control lungs. Note the significant global reduction in the expression of the AT2 markers. (n=3). (Part of this figure previously published in Dilai, 2020).

In summary, inhibition of FGF ligands at E12.5 for nine hours impacts the morphology of the tip epithelial cells, resulting in branching morphogenesis defects. Furthermore, these tip cells include the progenitors for the alveolar lineages, which, after FGFR2b signalling inhibition, lose expression of the markers characteristic of the AT2 signature.

4.4 Mid pseudoglandular stage development (E14.5)

The results in this section are adapted from (Jones et al., 2020).

4.4.1 Identification of the FGFR2b transcriptomic signature at E14.5 supports a primary role for FGF signalling in proliferation

Our work on the role of FGFR2b signalling during early pseudoglandular stage lung development (E12.5) suggested that FGF ligands primarily regulate distal epithelial cell-cell and cell-matrix adhesion and organization, as well as progenitor differentiation at this time. However, FGFR2b signalling showed no discernible regulation of proliferation at this early stage.

We built upon our results at E12.5 by using a similar experimental approach at E14.5, where we globally inhibited FGFR2b signalling for nine hours with a single Dox-IP (Fig. 15A). The impacts of inhibition on the branching of the distal epithelium were evidenced in the elongation of distal buds, the thickening of the mesenchyme, and the reduced bud number in experimental lungs (Fig. 15B). These gross morphological impacts were like those found at E12.5.

After extracting total RNA from control and experimental samples, we conducted qPCR analyses as well as a gene array. We determined that *Etv5*, a *bona fide* downstream target of FGFR2b signalling in the epithelium (Jones et al., 2019b), was significantly downregulated in experimental compared to control samples, as were *Sox9* and *Sftpc*, which are canonical markers for distal epithelial cells and AT2s, respectively (Fig. 15C). Markers for AT1 cells and proximal epithelium, *Aqp5* and *Scgb1a1*, respectively, showed no significant regulation at this timepoint. These results suggest that FGFR2b ligands act primarily on distal epithelial cells to maintain distal and AT2 progenitor status. Indeed, a gene-set analysis of AT1 and of AT2 signature genes from our E14.5 + 9 hrs. gene array showed a significant downregulation of AT2 markers in experimental lungs compared to controls, with little regulation on the AT1 signature (Fig. S3A-C).

Next, we identified the top 100 genes regulated in the gene array (according to p-value) (Fig. 15D). These 100 genes comprised two distinct groups of differentially regulated targets, 77 of which were downregulated (and assumed, therefore, to be positively regulated by FGFR2b signalling) and 23 of which were upregulated in experimental versus control lungs (See Fig. S4 for an enlarged version of the heatmap). The 77 downregulated genes comprise the FGFR2b gene signature at E14.5. As at E12.5, the current array was validated by assessing the expected regulation of the well-established FGF10-FGFR2b-ETV4/5-SHH pathway. Both *Etv4* and *Etv5* were highly and significantly downregulated in our E14.5 array (Log_2FC of -1.87 and -2.83, respectively), with a concomitant slight, yet significant downregulation of *Shh* (Log_2FC = -0.51, p-value = 0.004) and its downstream mesenchymal target *Gli1* (Log_2FC = -0.87, p-value = 0.00007). Consequently, it is predicted that *Fgf10* expression should increase with loss of SHH signalling, and indeed, that is what was found from the array (*Fgf10* Log_2FC = 0.58, p-value = 0.0009). This evidence, along with the expected regulation of Wnt signalling (*Wnt7a* Log_2FC = -1.04 and *Wnt7b* Log_2FC = -1.55), and the downregulation of the distal epithelial transcription factor *Sox9* (Log_2FC = -1.98), together with the predicted gross morphological changes observed, provide compelling evidence for the validity of our model to inhibit FGFR2b signalling at this timepoint.

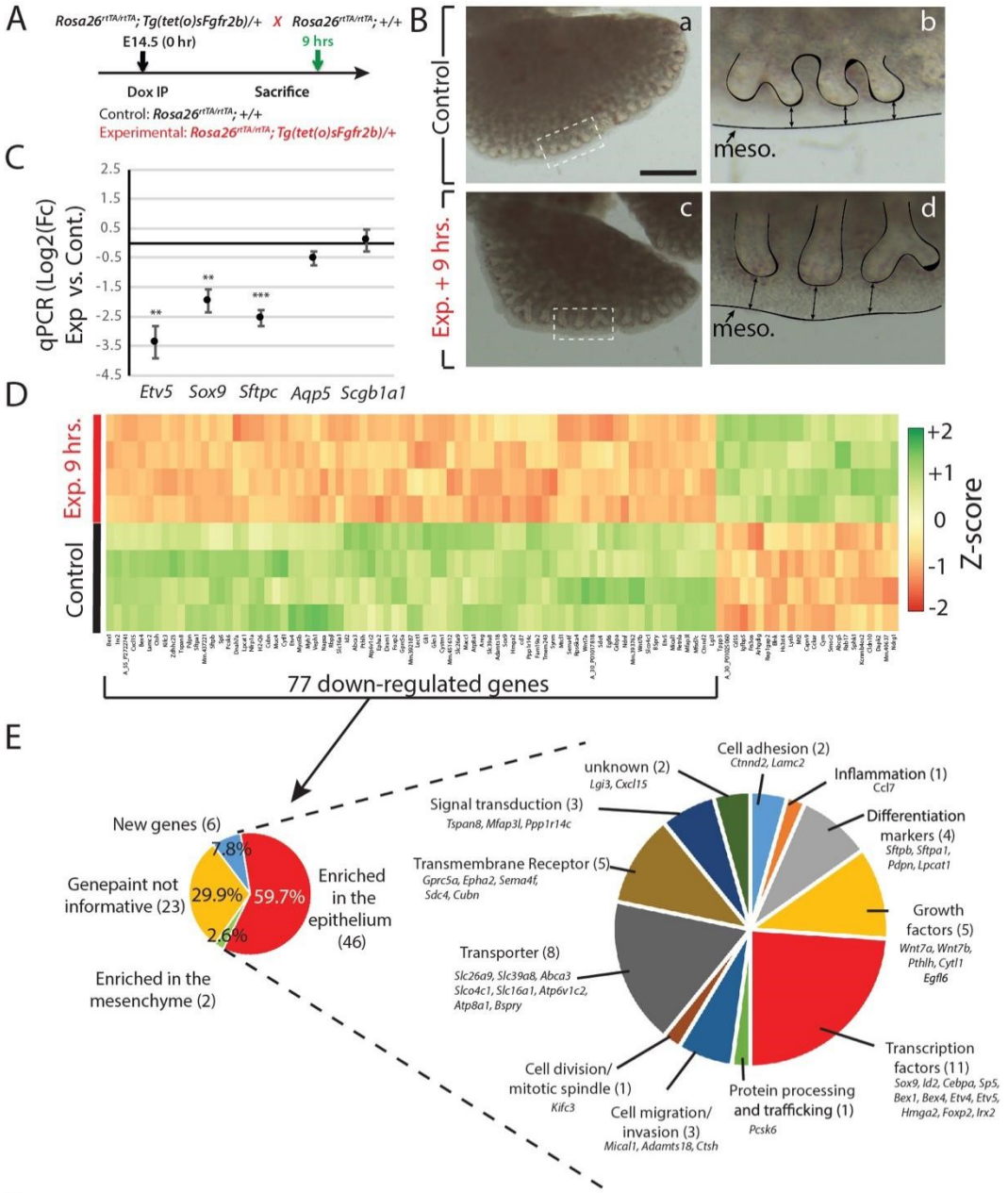

F

	KEGG name	n genes in set	n genes expr.	p value
KEGG	Ribosome biogenesis in eukaryote	74	69	3.55 E-19
	RNA transport	164	153	3.23 E-18
	Spliceosome	126	123	9.46 E-14
	DNA replication	35	35	1.88 E-10
	Pyrimidine metabolism	100	92	8.13 E-10
	Mismatch repair	22	22	8.33 E-7
	Cell cycle	123	119	4.04 E-6
	Aminoacyl-tRNA biosynthesis	44	44	5.02 E-6
	Biosynthesis of amino acids	76	62	5.93 E-6
	Metabolic pathways	1224	978	6.56 E-6

Figure 15 – Transcriptomic effects of FGFR2b signalling inhibition for 9 hours in E14.5 lungs.
(A) Experimental design: pregnant females carrying E14.5 experimental and littermate control

embryos were injected with a single Dox-IP and sacrificed 9 hours later. **(B)** Brightfield images of control (a, b) and experimental (c, d) lungs. Note the elongated epithelial tubes, reduced branching, and increased distance between the distal tips and mesothelium (black arrows) in the experimental lung compared to control. (Meso. = mesothelium). *Scale bar:* (a, c) 500 µm, (b, d) 125 µm. **(C)** qPCR analysis showing downregulation of *Etv5*, *Sox9*, and *Sftpc* in experimental vs. control lungs, while little change is observed in *Aqp5* and *Scgb1a1*. (n=3; **p-value < 0.01, ***p-value < 0.001). **(D)** Microarray expression data of the top 100 genes (according to p-value) regulated in experimental vs. control lungs. **(E)** Gene ontology of the 77 downregulated genes from the heatmap in D. genes were first grouped based on their region of enrichment in the lung according to expression data from 'Genepaint'. The 46 genes clearly enriched in the epithelium were then grouped according to their primary biological functions. **(F)** KEGG pathway analyses on the entire microarray data showing the top 10 regulated pathways in the experiment, according to significance.

Using the online *in situ* hybridization database 'Genepaint', we found that 59.7% of the 77 downregulated genes are enriched in the epithelium and 2.6% in the mesenchyme, while 7.8% of the genes are not included in the database. The *in situ* data for the remaining 29.9% were uninformative (Fig. 15E; Fig. S4). Gene ontological analysis of the genes enriched in the epithelium found that they comprise 11 main biological processes: cell adhesion (*Ctnnd2* and *Lamc2*), inflammation (*Ccl7*), markers of differentiation (*Sftpb*, *Sftpa1*, *Pdpn*, and *Lpcat1*), growth factors (*Wnt7a*, *Wnt7b*, *Pthlh*, *Cytl1*, and *Egfl6*), transcription factors (*Sox9*, *Id2*, *Cebpa*, *Sp5*, *Bex1*, *Bex4*, *Etv4*, *Etv5*, *Hmga2*, *Foxp2*, and *Irx2*), protein processing and trafficking (*Pcsk6*), cell migration and invasion (*Mical1*, *Adamts18*, and *Ctsh*), cell division and mitotic spindle (*Kifc3*), transporter (*Slc26a9*, *Slc39a8*, *Abca3*, *Slco4c1*, *Slc16a1*, *Atp6v1c2*, *Atp8a1*, and *Bspry*), transmembrane receptor (*Gprc5a*, *Epha2*, *Sema4f*, *Sdc4*, and *Cubn*), and signal transduction (*Tspan8*, *Mfap3l*, and *Ppp1r14c*). Furthermore, we identified the top 10 KEGG pathways most significantly regulated by the genes in the array and found that most of them are critical for cellular proliferation (ribosome biogenesis, RNA transport, spliceosome, DNA replication, pyrimidine metabolism, cell cycle, aminoacyl-tRNA biosynthesis, biosynthesis of amino acids, and metabolic pathways) (Fig. 15F). The top five of these E14.5 KEGG pathways were shared by the top five E12.5 pathways (Fig. 16A and B); however, each of the remaining pathways was different between the two timepoints. While at E12.5, pathways involved in cell-cell and cell-matrix adhesion were emphasized, at E14.5, pathways involved in the cell cycle and proliferation were more pronounced. This reflects a shift in the biological regulation

of FGFR2b signalling, from primarily a morphogenic to a proliferative effect, between early and mid-pseudoglandular stages.

We further analyzed the top genes directly regulated by FGFR2b signalling at E14.5 and E12.5. We found 43 genes specifically regulated at E12.5, 57 specifically regulated at E14.5, and 20 genes common between the two timepoints (Fig. 16C). KEGG pathway analyses of these groups of genes revealed that pathways regulated at E12.5, such as hedgehog signalling and pathways related to cancer, were also regulated by the genes shared among E12.5 and E14.5; whereas the E14.5 specific genes regulated the hippo signalling pathway, lysosome, axon guidance, and signalling pathways regulating the pluripotency of stem cells.

Surprisingly, none of the top KEGG pathways unique to E14.5 were involved in cellular proliferation, as suggested by the KEGG analysis of the entire gene array (Figure 15F). To assess the shift in FGFR2b biological regulation from a morphogenic (E12.5) to a proliferative (E14.5) effect, we plotted the regulation of cell-cycle specific genes (as an indication of proliferation) from the entire E12.5 gene array compared to their regulation in the E14.5 array (Fig. 16Da). Six cell cycle genes were specifically and significantly regulated at E12.5, 20 at E14.5, and three genes were shared between the two timepoints. Apart from the *cyclin dependent kinase* (*Cdk2*) and *cell division control 6* (*Cdc6*) genes significantly regulated specifically at E14.5, six other genes stand out (*E2f3, Myc, Mcm2, Mcm7, Skp2, and Gadd45b*) (see black arrows, Fig. 16Da and b). Of these six genes, all except *Gadd45b* showed a downregulation upon FGFR2b signalling inhibition; *E2f3* and *Myc* are both transcription factors, the first regulating the cell cycle, and the second related to proliferation, apoptosis, and cellular transformation; *Mcm2* and *Mcm7* are members of the minichromosome maintenance complex which is needed for the initiation of DNA replication; and *Skp2* is necessary for DNA synthesis during replication. Interestingly, the sixth gene from this list, *Gadd45b*, was significantly upregulated at E14.5. This gene encodes a protein which inhibits cell growth and showed a similarly significant yet opposite regulation to *Myc*, suggesting that proliferation at this stage is controlled both by the induction and repression of gene transcription.

A

KEGG analysis at E12.5 (DoxIP+9 hrs vs. control)

KEGG name	n genes in set	n genes expr.	p value
Ribosome biogenesis in eukaryote	76	69	9.68 E-16
RNA transport	161	136	7.29 E-14
Spliceosome	126	120	2.57 E-10
DNA replication	35	35	4.74 E-7
Pyrimidine metabolism	97	85	2.97 E-6
Calcium signaling pathway	179	88	1.17 E-5
Focal adhesion	201	155	1.40 E-5
ECM-receptor interaction	87	59	2.01 E-5
Cell adhesion molecules (CAMs)	146	71	5.61 E-5
Ether lipid metabolism	37	22	6.30 E-5

B

KEGG analysis at E14.5 (DoxIP+9 hrs vs. control)

KEGG name	n genes in set	n genes expr.	p value
Ribosome biogenesis in eukaryote	74	69	3.55 E-19
RNA transport	164	153	3.23 E-18
Spliceosome	126	123	9.46 E-14
DNA replication	35	35	1.88 E-10
Pyrimidine metabolism	100	92	8.13 E-10
Mismatch repair	22	22	8.33 E-7
Cell cycle	123	119	4.04 E-6
Aminoacyl-tRNA biosynthesis	44	44	5.02 E-6
Biosynthesis of amino acids	76	62	5.93 E-6
Metabolic pathways	1224	978	6.56 E-6

(modified from Jones et al., 2019a)

C

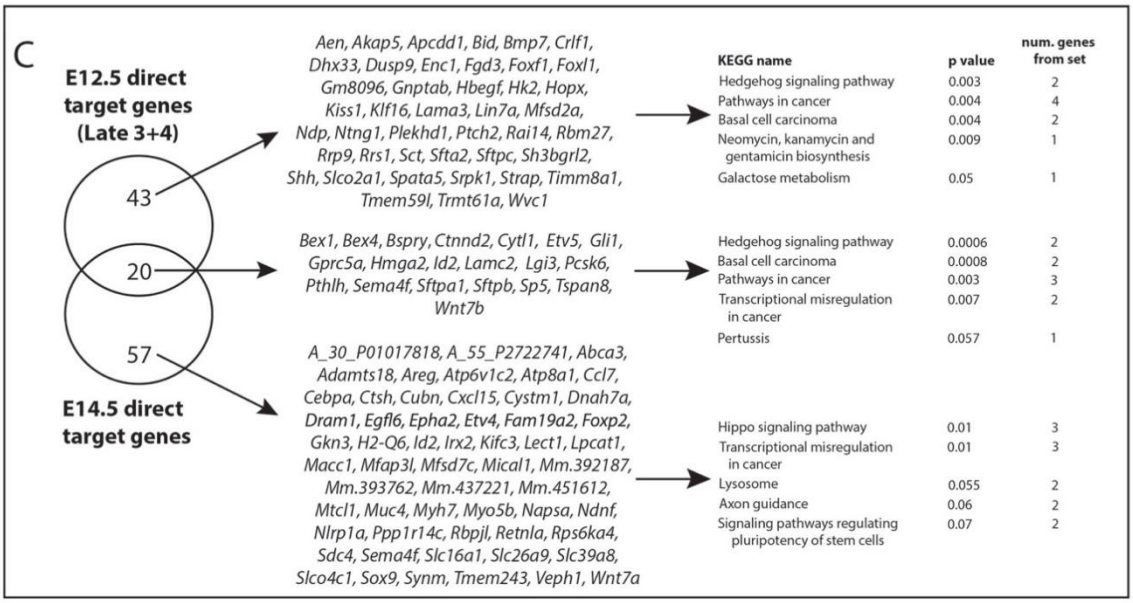

KEGG name	p value	num. genes from set
Hedgehog signaling pathway	0.003	2
Pathways in cancer	0.004	4
Basal cell carcinoma	0.004	2
Neomycin, kanamycin and gentamicin biosynthesis	0.009	1
Galactose metabolism	0.05	1
Hedgehog signaling pathway	0.0006	2
Basal cell carcinoma	0.0008	2
Pathways in cancer	0.003	3
Transcriptional misregulation in cancer	0.007	2
Pertussis	0.057	1
Hippo signaling pathway	0.01	3
Transcriptional misregulation in cancer	0.01	3
Lysosome	0.055	2
Axon guidance	0.06	2
Signaling pathways regulating pluripotency of stem cells	0.07	2

D

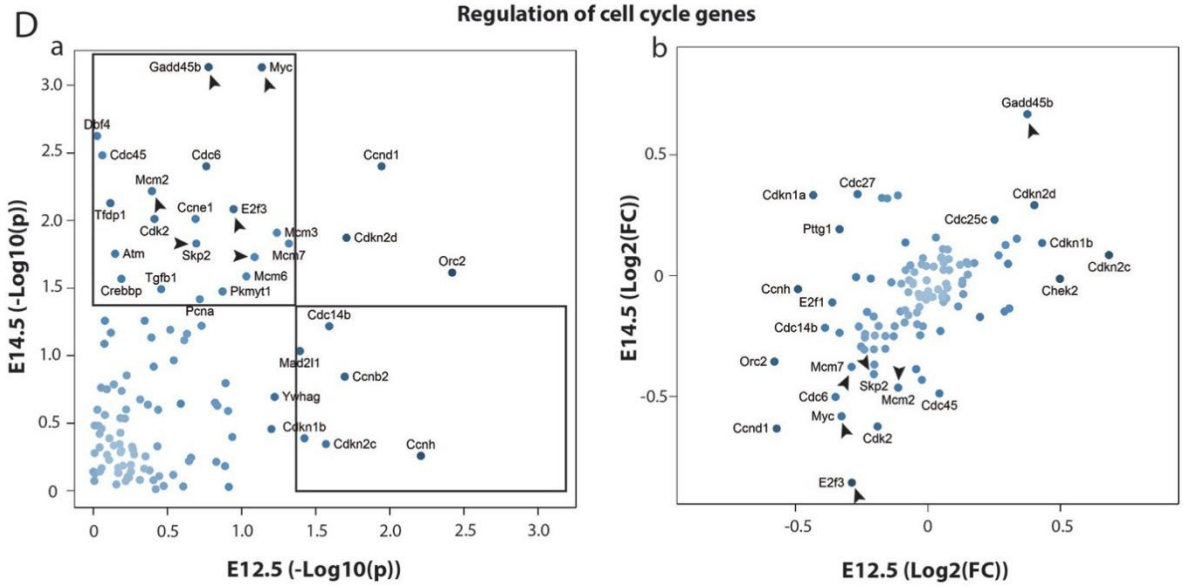

Figure 16 – Comparison of the FGFR2b transcriptomic targets between E12.5 and E14.5. (A) KEGG analysis at E12.5 and **(B)** at E14.5. **(C)** List of the genes which are specific to E12.5 and to E14.5, and which are shared between the two timepoints, along with the top five KEGG pathways regulated by each group of genes. **(D)** Scatterplots depicting the regulation,

according to p-value (a) and fold change (b), of cell cycle specific genes at E12.5 and at E14.5. Black arrows indicate significantly regulated genes specifically at E14.5. See text for details.

To further investigate the role of FGFR2b signalling on proliferation at E14.5, we stained experimental and littermate control lungs nine hours after FGFR2b inhibition for Ki67 and TUNEL, to assess proliferation and apoptosis, respectively (Fig. 17). Ki67 intensity was significantly decreased in experimental lungs compared to controls, in both the distal epithelial and mesenchymal compartments (Fig. 17A and B), whereas apoptosis was nearly absent in both control and experimental samples (data not shown). Here, as in our E12.5 experiments, the epithelial cells pile atop one another in a disorganized fashion in the lumens of experimental distal epithelial buds (compare Fig. 17Ac and f).

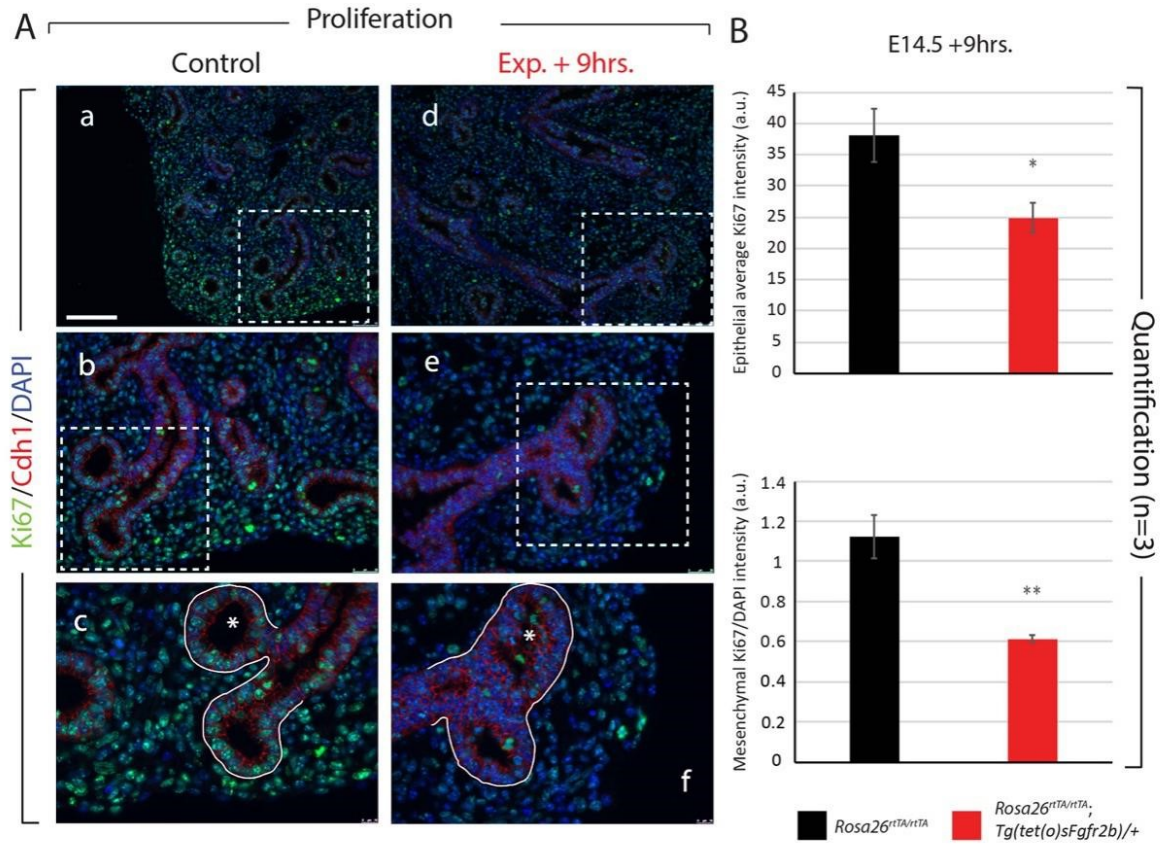

Figure 17 – Analysis of proliferation in E14.5 lungs after 9 hours FGFR2b inhibition. (A) Control (a-c) and experimental (d-f) lungs were stained for Ki67 and CDH1 to assess proliferation in the epithelial and mesenchymal compartments (separated by the white line in c and f). Note the multi-layered and disorganized epithelium invading the lumen of experimental lung buds (compare asterisks in c and f), which is a hallmark of FGFR2b inhibition

at E12.5 as well. *Scale bar:* (a, d) 100 µm, (b, e) 50 µm, (c, f) 20 µm. **(B)** Quantification of Ki67 expression showing a significant decrease in proliferation in both the epithelial and mesenchymal compartments. (a.u. = arbitrary units) (*p-value < 0.05, **p-value < 0.01).

Taken together, the results of FGFR2b inhibition at E14.5 + 9 hrs. reveal a high correlation with the regulation of epithelial morphogenesis and differentiation at E12.5, but also emphasize the primary importance of FGFR2b signalling on the proliferation of distal epithelial and mesenchymal cells at E14.5, likely through the cell cycle specific genes identified from the array.

4.4.2 Inhibition of FGFR2b signalling for 24 hours drastically decreases proliferation and impacts AT2 differentiation

To further assess the effects of short-term inhibition of FGFR2b signalling on E14.5 lungs, we analyzed the phenotype of experimental lungs 24 hours after FGFR2b ligand inhibition (Fig. 18A). Examination of the experimental and control lungs revealed impaired branching of the epithelium with the characteristic elongated distal branches and thicker mesenchyme (Fig. 18Ca-d). qPCR analysis showed that expression of *Etv5* and *Sftpc* was reduced in experimental lungs compared to controls (Fig. 18B). While the downregulation of *Sftpc* was significant, that of *Etv5* was not, which contrasts with the highly significant downregulation of this gene after 9 hours inhibition (see Fig. 15C). This could be a consequence of the recovery of normal FGFR2b signalling, as the soluble FGFR2b is insufficiently transcribed 24 hours after a single Dox-IP (Danopoulos et al., 2013). Furthermore, *Aqp5* and *Scgb1a1*, markers for AT1 cells and proximal epithelium, respectively, tended toward upregulation in experimental compared to control lungs.

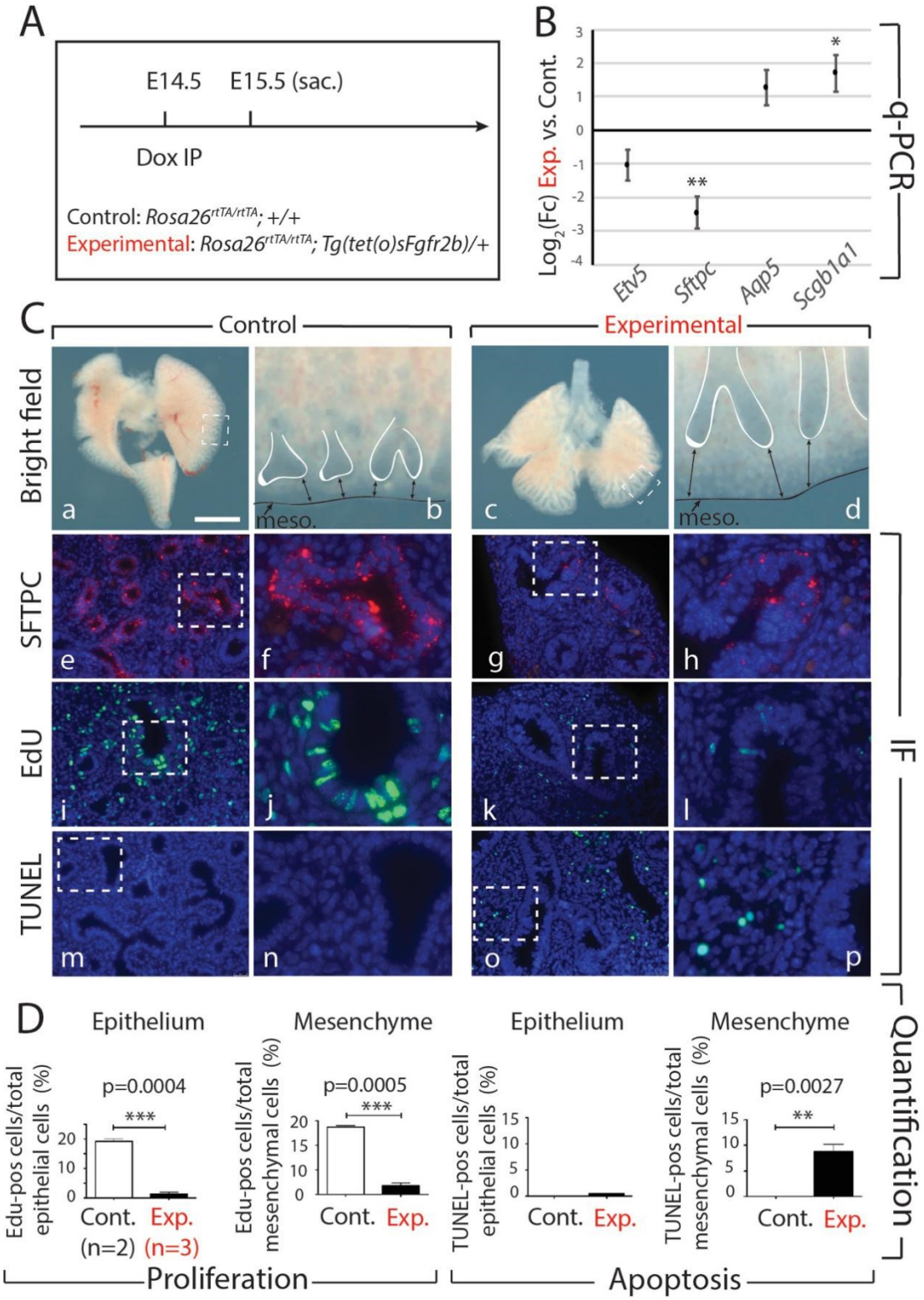

Figure 18 – Effects of transient FGFR2b signalling inhibition for 24 hours in E14.5 lungs. (A) Experimental design: pregnant females carrying experimental and littermate control embryos were injected with a single Dox-IP and sacrificed 24 hours later. **(B)** qPCR analysis showing downregulated expression of AT2 markers *Etv5* (not significant) and *Sftpc* (n=3; **p-value < 0.01), and upregulated expression of the AT1 marker *Aqp5* (not significant), and the proximal

epithelial marker *Scgb1a1* (n=3; *p-value < 0.05). **(C)** Brightfield (a-d) and immunofluorescent (e-p) images of control and experimental lungs. Note the elongated epithelial tubes, reduced distal tip branching, and increased distance between tips and mesothelium (black arrows) in experimental lungs compared to controls (d vs. b). Staining for SFTPC shows a decrease in the epithelium of experimental lungs (h vs. f), confirming the qPCR expression data. Staining for EdU and TUNEL to assess proliferation and apoptosis, respectively, showed decreased proliferation in both the epithelial and mesenchymal compartments of experimental lungs compared to controls (l vs. j), while apoptosis was increased only in the mesenchyme of experimental lungs (p vs. n). (meso. = mesothelium). *Scale bar:* (a, c) 750 µm, (b, d) 95 µm, (e, g, i, k, m, o) 75 µm, (f, h, j, l, n, p) 30 µm. **(D)** Quantification of EdU and TUNEL expressions in the epithelial and mesenchymal compartments of experimental vs. control lungs. (**p-value < 0.01, ***p-value < 0.0001).

The downregulation of *Sftpc* in experimental lungs suggests regulation of the AT2 lineage progenitors. Indeed, impacted AT2 differentiation was confirmed by SFTPC immunofluorescence staining, where control lungs showed a robust and strong expression in distal epithelium (Fig. 18Ce and f), the expression in experimental lungs was clearly reduced (Fig. 18Cg and h). Finally, analysis of proliferation and apoptosis, using EdU and TUNEL staining, respectively, demonstrated a drastic reduction in proliferative cells in experimental compared to control lungs (Fig. 18Ci-l). Our quantification confirmed decreased proliferation in both the epithelium ($p<0.001$) and the mesenchyme ($p<0.001$), while cell death was increased in the mesenchyme ($p=0.0027$) but not in the epithelium of experimental lungs (Fig. 18D).

These results demonstrate that inhibiting FGFR2b signalling at E14.5 for 24 hrs. leads to effects on branching, proliferation, and progenitor cell differentiation similar to those found after 9 hrs., albeit, much more pronounced. The primary role of FGFR2b signalling on proliferation was also clear at the 24-hour timepoint; neither epithelial nor mesenchymal cells in experimental lungs regained proliferative capacity, while the number of apoptotic cells significantly increased in the mesenchyme.

4.4.3 Continuous inhibition of FGFR2b signalling from E14.5 to E18.5 impacts the distal epithelial cell lineages

Next, we assessed the impacts of continuous FGFR2b inhibition from E14.5 to E18.5 by feeding pregnant mice carrying experimental and littermate controls Dox-food for the duration of the experiment (Fig. 19A). Examination of the experimental lungs compared to the controls revealed abnormal lung development with delayed growth resulting in noticeably smaller lungs, as well as dilated epithelial end buds (Fig. 19Ca-d). Immunofluorescence antibody staining for the proximal epithelial club cell marker SCGB1A1 indicated that proximal epithelium extended to the distal periphery of the lung in experimental vs. control lungs (Fig. 19Ce-h). We also observed a severe reduction in SFTPC+ cells, as well as a complete absence of AQP5+ cells in experimental lungs (Fig. 19Ci-p). These findings were supported by qPCR analyses of mRNA isolated from whole lungs, which showed a significant reduction in *Sftpc* and *Aqp5* expression in experimental vs. control lungs. However, no change was seen in *Scgb1a1* expression (Fig. 19B). These results suggest that FGFR2b signalling from E14.5 to E18.5 primarily affects the distal epithelial cell lineages.

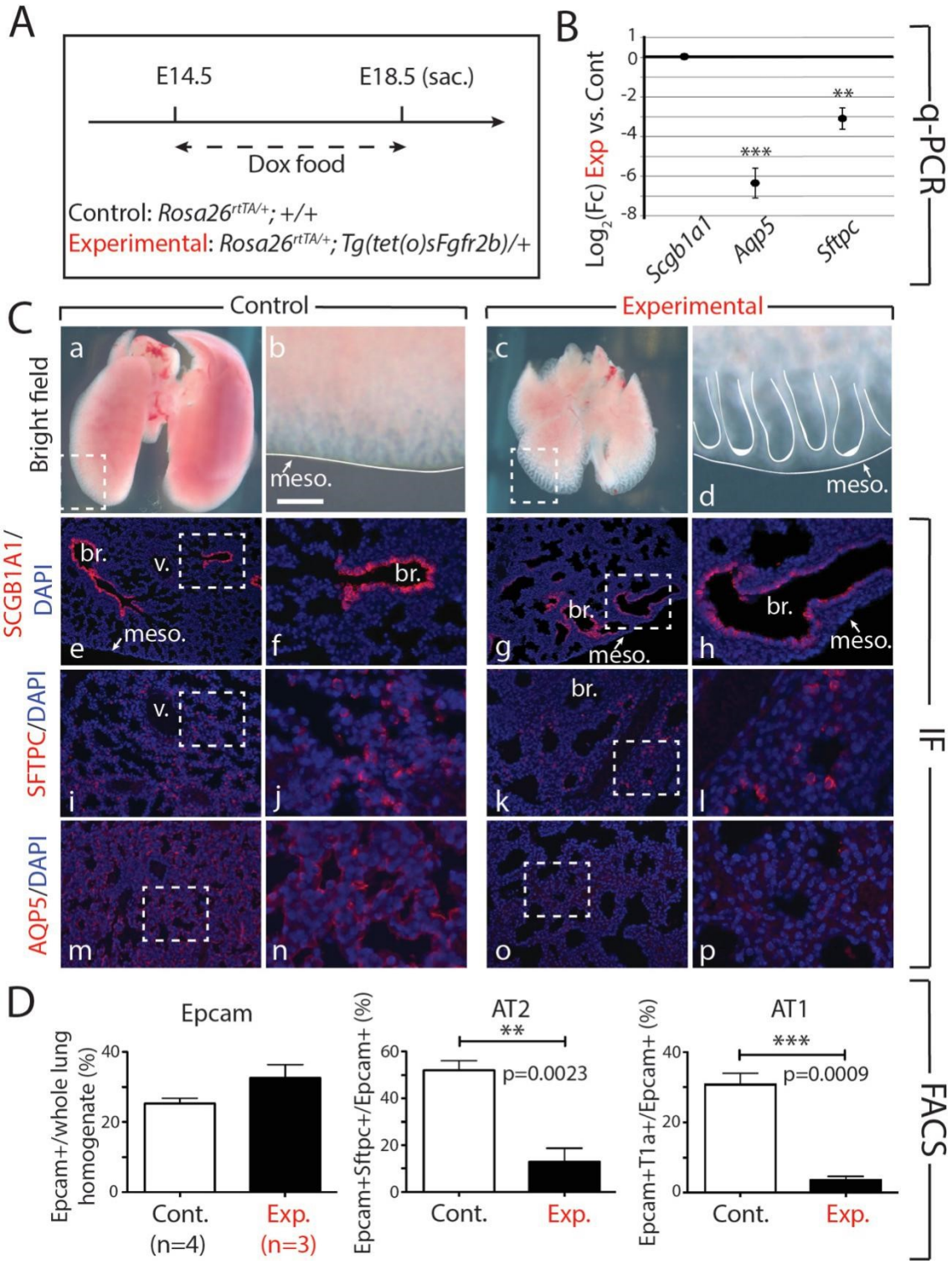

Figure 19 – Continuous inhibition of FGFR2b signalling from E14.5 to E18.5 leads to impaired AT1 and AT2 formation. (A) Experimental design: pregnant females carrying experimental and littermate control embryos were fed Dox-food continuously for four days before being sacrificed at E18.5. **(B)** qPCR results showing significant downregulation of the AT1 marker *Aqp5* and the AT2 marker *Sftpc* in experimental versus control lungs. *Scgb1a1* shows no change in expression. (n=3; **p-value < 0.01, ***p-value < 0.001). **(C)** Brightfield (a-d) and

immunofluorescent (e-p) images of control and experimental lungs. Note the smaller overall size and the dilated epithelial branches of experimental lungs compared to controls (c and d vs. a and b). Staining for SCGB1A1 shows a clear boundary between SCGB1A1+ proximal and SCGB1A1-negative distal epithelium in control lungs (e and f), whereas an ectopic distribution is seen in experimental lungs (g and h), with SCGB1A1+ cells found in distal regions of the lung. Staining for SFTPC (i-l) and AQP5 (m-p) reveal a downregulation of these proteins in experimental compared to control lungs, confirming the downregulation of these genes seen in the qPCR analysis (B). (meso. = mesothelium, br. = bronchus, v. = vessel). *Scale bar:* (a, c) 750 µm, (b, d) 95 µm, (e, g, i, k, m, o) 150 µm, (f, h, j, l, n, p) 30 µm. **(D)** FACS-based quantification shows no significant difference in the proportion of EpCAM+ (epithelial) cells relative to the total (CD45- CD31-) lung cells in experimental versus control lungs, but a significant decrease in the proportion of AT2 (EpCAM+ SFTPC+ from total EpCAM+) (**p-value < 0.01) and AT1 (EpCAM+T1alpha+ from total EpCAM+) (***p-value < 0.001) cells in experimental versus control lungs.

The decrease In experimental lungs of AT1 and AT2 cell numbers was also validated by flow cytometry (Fig. 19D). The ratio of EpCAM+ cells (EpCAM, or epithelial cell adhesion molecule, is ubiquitously expressed in the epithelium) to the whole lung homogenate did not change between experimental and control lungs, which is likely a consequence of arrested proliferation in both the epithelial and mesenchymal compartments of experimental lungs, thus resulting in smaller lungs overall. However, a clear reduction in the ratios of AT1 and AT2 (over the total number of EpCAM+ cells) was observed (p=0023 and p=0.0009 for ratio of AT2 and AT1 cells over EpCAM in experimental vs. control lungs, respectively, Fig. 19D). This result indicates that the alveolar lineage was completed aborted in experimental lungs, which corresponds with the expansion of SCGB1A1+ cells into the distal epithelium (Fig. 19Cg and h).

Taken together, results from the continuous long-term inhibition of FGF ligands beginning in E14.5 lungs suggest that FGFR2b signalling, while promoting lung growth, also directly targets the alveolar lineages. In the absence of FGFR2b signalling from E14.5 onward, both the AT1 and AT2 cells fail to form.

4.4.4 Transient inhibition of FGFR2b at E14.5 leads to irreversible developmental damages at E18.5

Given the strong phenotypic effects of a single Dox-IP after 9 and 24 hours in experimental lungs, we were interested in investigating to what extent E14.5 lungs could recover from a single Dox-IP later in development. We therefore injected pregnant females at E14.5 and assessed experimental and littermate control embryos at E18.5 (Fig. 20A). Recall that a single Dox-IP leads to the recombination of soluble FGFR2b shortly thereafter, with levels peaking around 6 hours before returning to pre-injection levels after 24 hours (Danopoulos et al., 2013). Thus, a single Dox-IP in our mouse model leads to approximately 24 hours FGFR2b signalling inhibition.

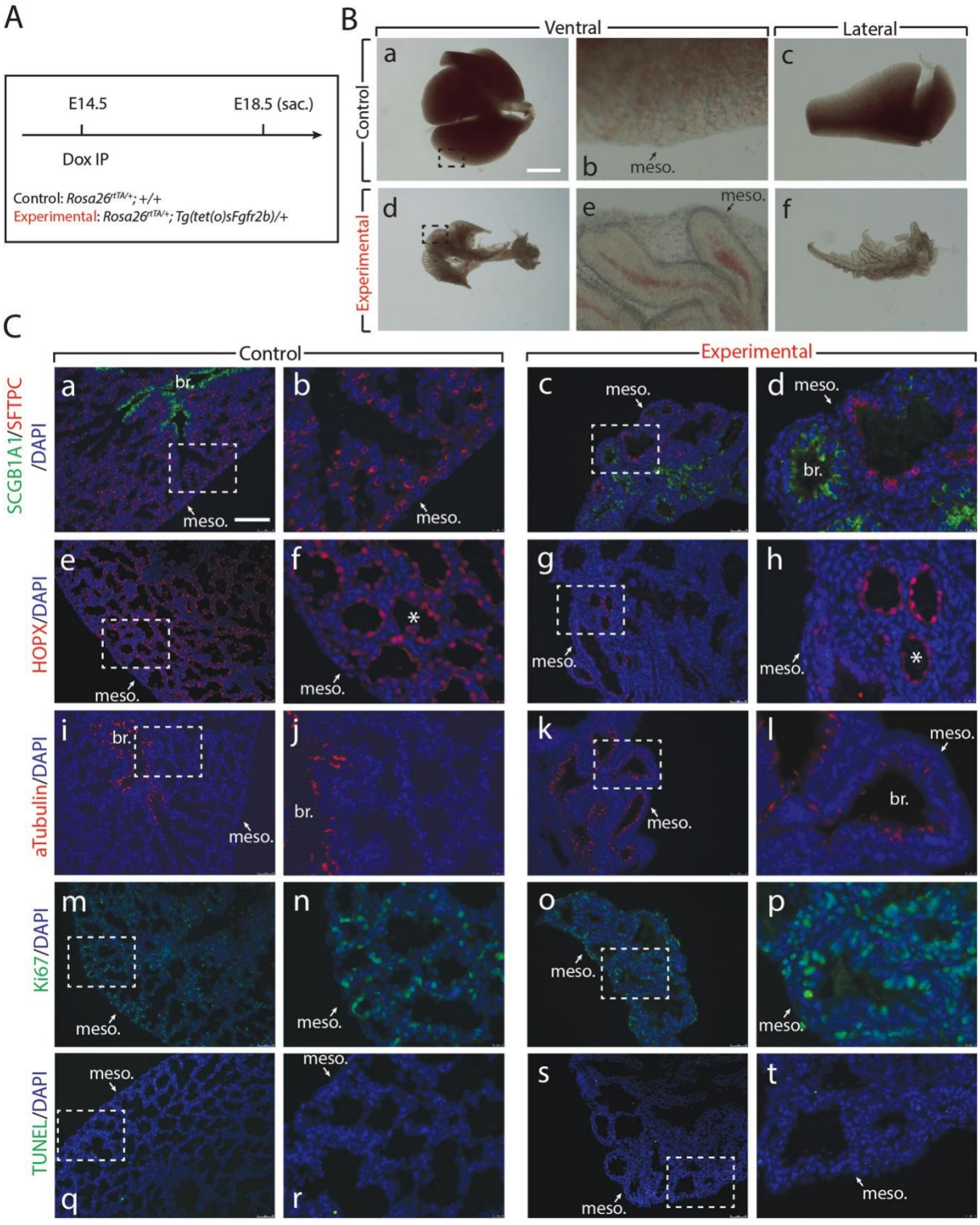

Figure 20 – Experimental lungs are developmentally arrested after transient FGFR2b signalling inhibition at E14.5. (A) Experimental design: pregnant females carrying experimental and littermate control embryos were injected with a single Dox-IP at E14.5 and embryos were harvested at E18.5. **(B)** Brightfield images of the ventral side of the whole lung in control (a, b) and experimental (d, e) samples, as well as the lateral perspective of the accessory lobe (c and f). Apart from the drastic difference in overall lung size between

experimental and control lungs (d vs. a), notice the complete failure of the experimental epithelium to form the numerous branches and alveoli seen in the control, as well as the reduced mesenchyme and thickness of the lobes seen in the experimental lungs (f vs. c). (meso. = mesothelium). *Scale bar:* (a, d) 1.5 mm, (b, e) 95 µm, (c, f) 375 µm. **(C)** Immunofluorescent images (a-t) for control and experimental lungs. Antibody staining for AT1 (HOPX) and AT2 (SFTPC) cells suggests an overall reduction in the number of these cells in experimental compared to control lungs (compare c and g to a and e). Furthermore, in the case of HOPX staining in the experimental lungs (see g and h), there are cells with a similar expression pattern to the AT1 cells seen in controls, but also epithelial cells displaying a sparse, much reduced expression pattern (compare cells in the structure labelled by asterisks in h vs. f). Staining for the proximal epithelial markers SCGB1A1 and acetylated alpha-Tubulin reveals ectopic and distal expression in experimental compared to control lungs (compare d and l to b and j). Finally, staining for Ki67 (m-p) and TUNEL (q-t) to assess proliferation and apoptosis, respectively, shows that, in general, there is little to no impact on proliferative processes in either the epithelial or mesenchymal compartments. (meso. = mesothelium, br. = bronchus). *Scale bar:* (a, c, e, g, i, k, m, o, q, s) 125 µm, (b, d, f, h, j, l, n, p, r, t) 25 µm.

Remarkably, experimental lungs assessed at E18.5 showed a much more drastic phenotype than experimental lungs from our continuous long-term inhibition of FGFR2b (compare Fig. 20B with Fig. 19C). We propose that this is likely a consequence of the route of administration of the doxycycline between the two experiments (Food vs. IP). An IP-injection delivers to the system a relatively high dose of doxycycline in a short time, while doxycycline from food accumulates in the system gradually and over a longer period of time. Whereas experimental lungs from the continuous inhibition experiment were slightly smaller than control lungs, exhibiting reduced branching along with elongated epithelial tubes, the experimental lungs of the transient inhibition experiment were drastically different from littermate controls; these lungs were much smaller than controls, showed very long spaghetti-like non-branched epithelial tubes, and almost a complete absence of mesenchyme in addition to reduced thickness of the lobes when viewed laterally (Fig. 20Ba-f).

Immunofluorescent stains for SFTPC and HOPX, markers for AT2 and AT1 cells, respectively, revealed the impacts of transient FGFR2b inhibition on both lineages (Fig. 20Ca-h). While in control lungs SFTPC and HOPX were robustly expressed in distal alveolar sacs, expression of these markers in experimental lungs was clearly decreased and of varying robustness, especially of the HOPX protein (compare HOPX expression by the asterisks in Fig. 20Ch).

Staining for the proximal club cell marker SCGB1A1 also revealed the variable and disorganized distribution of proximal and distal epithelial lineages in experimental lungs (compare Fig. 20Ca and b to c and d). While a clear demarcation between proximal and distal epithelium existed in control lungs, there was no clear demarcation in experimental lungs, with SCGB1A1 being expressed in both proximally and distally located epithelium (of interest, however, is the observation that SCGB1A1 expression did not co-localize with that of SFTPC, suggesting that individual epithelial cells had adopted either a proximal or distal cell fate, respectively).

We also stained for other markers of proximal cell types. For example, acetylated alpha-Tubulin, a marker for ciliated cells, further confirmed the atypical expression of the proximal epithelial lineage in the distal epithelium of the experimental lungs (Fig. 20Ci-l). While ciliated cells lined the proximal conducting airways of control lungs, they were scattered throughout the proximally and distally located epithelium of experimental lungs.

Finally, to determine whether the drastic phenotype seen in experimental lungs was a consequence of aberrant proliferation, we stained control and experimental lungs for Ki67 and for TUNEL to assess proliferation and apoptosis, respectively (Fig. 20Cm-t). The experimental lung showed a significant number of Ki67+ cells and did not appear different compared to the control lung. Apoptosis was not differentially regulated between control and experimental lungs. We therefore conclude that transient inhibition of FGFR2b signalling, apart from completely arresting the gross morphological development of the lung, leads to the near total failure of the distal epithelium to form. In addition, the proximal epithelium, along with the remaining mesenchyme, appears to normally proliferate four days after transient FGFR2b signalling inhibition.

4.5 Late pseudoglandular and early canalicular stage (E14.5-E16.5)

The results in this section are adapted from (Jones et al., 2022).

4.5.1 AT1 and AT2 progenitor lineage labelling suggests a level of cross-lineage contribution

It has been argued that AT1 and AT2 progenitor cell populations are largely unipotent as early as E13.5 during mouse lung development (Frank et al., 2019). This contrasts with the earlier model proposing that the majority of mature pneumocytes pass through a bipotential progenitor well after E13.5 (Treutlein et al., 2014). To address this issue, we investigated the lineage-commitment of early alveolar progenitors using our mouse models. We labelled AT1 and AT2 progenitor cells during the late pseudoglandular stage using *Hopx*$^{CreERT2/+}$; *tdTomato*$^{flox/flox}$ (n=3) and *Sftpc*$^{CreERT2/+}$; *tdTomato*$^{flox/flox}$ (n=3) transgenic mouse lines, respectively. We labelled cells via two tamoxifen IP (Tam-IP) injections (E14.5 and E15.5) and assessed the contribution of lineage-labelled cells to each alveolar epithelial population at E18.5 (Fig. 21A). Assessing the expression of SFTPC and of HOPX proteins via immunofluorescence staining in the *Sftpc*^{CreERT2} line, it was observed that around 19% and 78% of labelled (RFP^{Pos}) cells were HOPX^{Pos} and SFTPC^{Pos}, respectively (Fig. 21B and C). The expression of labelled SFTPC^{Pos} and of HOPX^{Pos} cells in the *Hopx*^{CreERT2} line was essentially the reverse of what was found in the *Sftpc*^{CreERT2} line: around 74% and 30% of RFP^{Pos} cells were HOPX^{Pos} and SFTPC^{Pos}, respectively (Fig. 21D and E).

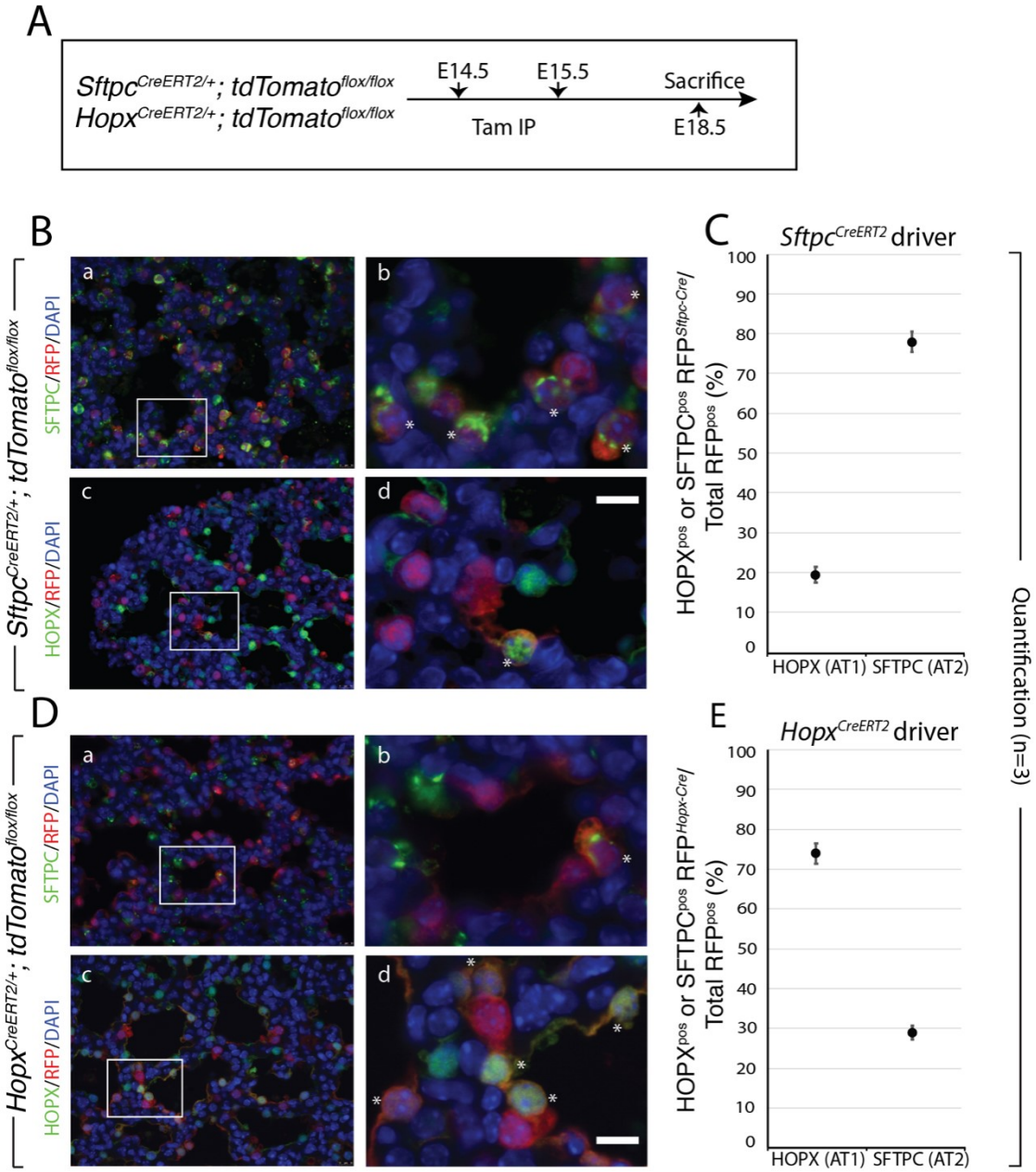

Figure 21 – Lineage tracing of AT2 (*Sftpc*) and AT1 (*Hopx*) progenitors suggests inter-lineage contributions. (A) Transgenic mice carrying a *CreERT2* allele downstream of a *Sftpc* promoter or a *Hopx* promoter were used to label AT2 or AT1 progenitors, respectively, by recombining a floxed 'stop' cassette upstream of a *tdTomato* reporter. Timed-pregnant females were injected intraperitoneally with tamoxifen (Tam-IP) at E14.5 and E15.5, and embryonic lungs were harvested just prior to birth at E18.5. **(B)** Lineage-labelled *Sftpc*$^{CreERT2/+}$; *tdTomato*$^{flox/flox}$ embryonic lungs were immunostained for SFTPC (a and b) and HOPX (c and d) to assess the contribution of labelled cells to the AT2 and AT1 lineages, respectively (see asterisks in panels b and d for examples of lineage-labelled AT2 and AT1 cells, respectively). *Scale bar: (a, c) 30 µm, (b, d) 7.5 µm.* **(C)** Labelled AT1 and AT2 cells were counted from multiple images taken from three independent samples (n=3) and are displayed as a percentage of the total number of Tomato RFP^{pos} cells. Labelled HOPX (AT1) cells compose around 19.21% ± 1.62% of the total RFP^{pos} population, whereas labelled (SFTPC) AT2 cells compose around 78.09% ± 2.50%. **(D)**

Lineage-labelled *Hopx*$^{CreERT2/+}$; *tdTomato*$^{flox/flox}$ embryonic lungs were immunostained for SFTPC (a and b) and HOPX (c and d) to assess the contribution of labelled cells to the AT2 and AT1 lineages, respectively (see asterisks in panels b and d for examples of lineage-labelled AT2 and AT1 cells, respectively). *Scale bar:* (a, c) 30 µm, (b, d) 7.5 µm. **I** Labelled HOPX (AT1) cells compose around 74.02% ± 1.29% of the total RFP^{pos} pool, whereas labelled (SFTPC) AT2 cells compose around 29.75% ± 0.50%.

These data demonstrate that a significant proportion of mature pneumocytes (around 20%-30%) derive from lineage-flexible progenitors (both uni- and bi-potent) when labelled during mid-pseudoglandular development.

4.5.2 Cell autonomous deletion of *Fgfr2b* in SFTPC^{pos} AT2 progenitors pushes them toward the PDPN^{pos} AT1 lineage

To investigate the role of FGFR2b signalling specifically on AT2 progenitor cell fate, we utilized a previously validated *Sftpc*$^{CreERT2/+}$; *tdTomato*$^{flox/flox}$; *Fgfr2b*$^{flox/flox}$ line (Ahmadvand et al., 2022b). This line labels AT2 (*Sftpc*) progenitors while simultaneously excising the IIIb isoform of the *Fgfr2* gene (De Moerlooze et al., 2000).

We Tam-IP injected at E14.5 and E15.5 timed-pregnant females carrying either control (*Sftpc*$^{CreERT2/+}$; *tdTomato*$^{flox/flox}$) (n=7) or experimental (*Sftpc*$^{CreERT2/+}$; *tdTomato*$^{flox/flox}$; *Fgfr2b*$^{flox/flox}$) (n=7) embryos and harvested the lungs at E18.5 (Fig. 22A). We then FACS-isolated alveolar epithelial cells (AEC) based on the pan-epithelial marker EpCAM and the alveolar lineage specific marker CD49f (EpCAM^{pos}CD49f^{pos}). From these, RFP-labelled AT1 (AEC^{pos}, RFP^{Pos}, T1α^{Pos}) and AT2 (AEC^{Pos}, RFP^{Pos}, T1α^{Neg}) cells were isolated (see Fig. S5A-C for the FACS gating strategy). As Figure 22B shows, the proportion of RFP-labelled AEC decreased from around 49% in control samples to 41% in experimental lungs. From these epithelial cells, the percentage of RFP^{Pos}-labelled T1α^{pos} AT1 cells relative to the RFP^{Pos} epithelium (EpCAM^{Pos}RFP^{Pos}) drastically increased from around 21 in controls to 86% in experimental lungs, while the percentage of labelled AT2 (EpCAM^{Pos}RFP^{Pos}T1α^{Neg}) cells significantly decreased from around 79% to 15%.

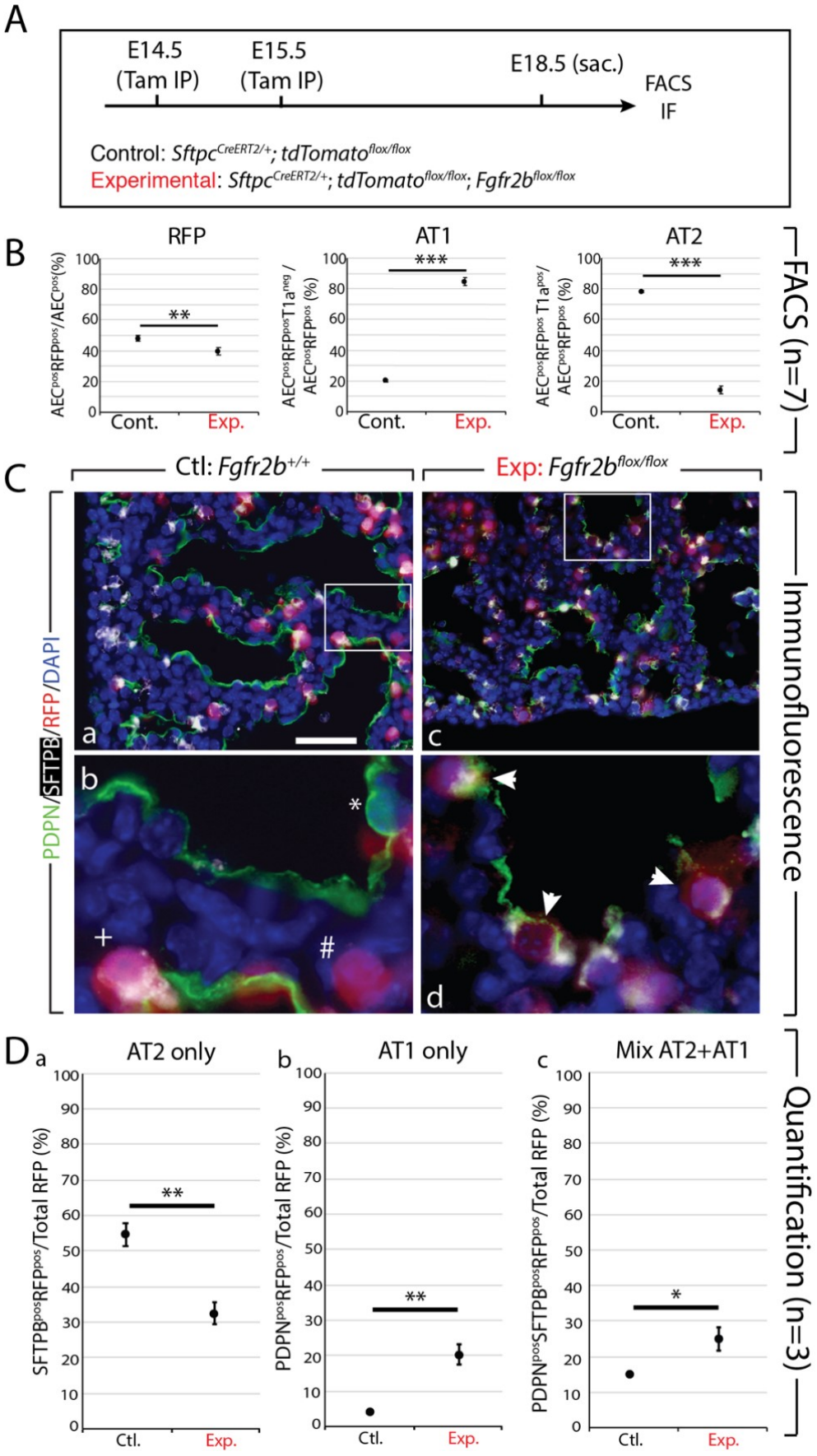
A
E14.5
(Tam IP)
E15.5
(Tam IP)
E18.5 (sac.)
FACS
IF
Control: Sftpc CreERT2/+; tdTomato flox/flox
Experimental: Sftpc CreERT2/+; tdTomato flox/flox; Fgfr2b flox/flox
B
RFP
AT1
AT2
AEC pos RFP ppos/AEC pos(%)
AEC pos RFP ppos T1a neg / AEC pos RFP ppos (%)
AEC pos RFP ppos T1a pos / AEC pos RFP ppos (%)
Cont.
Exp.
FACS (n=7)
C
Ctl: Fgfr2b +/+
Exp: Fgfr2b flox/flox
PDPN/SFTPB/RFP/DAPI
a
b
c
d
Immunofluorescence
D
a AT2 only
b AT1 only
c Mix AT2+AT1
SFTPB pos RFP ppos/Total RFP (%)
PDPN pos RFP ppos/Total RFP (%)
PDPN pos SFTPB pos RFP ppos/Total RFP (%)
Ctl.
Exp.
Quantification (n=3)

Figure 22 – Cell autonomous deletion of *Fgfr2b* in *Sftpc*-positive progenitors results in increased proportion of RFP-labelled AT1 cells and mixed AT1 and AT2 cells. (A) Experimental design. Pregnant females carrying either control or experimental embryos were injected with TAM-IP at E14.5 and E15.5, and embryonic lungs were harvested at E18.5. **(B)** Control (n=7) and experimental (n=7) lungs were processed for FACS analysis and isolation of cells. $EpCAM^{pos}$ $CD49f^{pos}$ alveolar epithelial cells (AEC) were sorted, then the tomato RFP^{pos} population was isolated. From these, AT1 and AT2 cells were isolated based on the expression of the AT1 marker T1α (Podoplanin). A decrease in the proportion of RFP-labelled alveolar epithelial cells ($AEC^{pos}RFP^{pos}/AEC^{pos}$) is observed in experimental (40.6% ± 2.57%) versus control lungs (48.64% ± 1.21%). A significant increase is seen in the proportion of RFP-labelled AT1 cells (AEC^{pos} RFP^{pos} $T1\alpha^{pos}/AEC^{pos}$ RFP^{pos}) in experimental versus control lungs (85.5% ± 2.44% vs. 20.93% ± 0.64%); concomitantly, a significant decrease in labelled AT2 cells (AEC^{pos} RFP^{pos} $T1\alpha^{neg}/AEC^{pos}$ RFP^{pos}) is observed in experimental versus control lungs (14.5% ± 2.44% vs. 79.07% ± 0.64%). (n=7; ***p-value < 0.001). **(C)** Immunofluorescent staining for PDPN (AT1 marker) and SFTPB (AT2 marker) in control $Fgfr2b^{+/+}$ (a and b) and experimental $Fgfr2b^{flox/flox}$ (c and d) lungs. Single- and double-labelled cells are shown in 'b' (* = $PDPN^{pos}$, # = RFP^{pos}, + = $SFTPB^{pos}/RFP^{pos}$). Triple-labelled cells are shown in 'd' (arrowheads = $PDPN^{pos}/SFTPB^{pos}/RFP^{pos}$). *Scale bar: (a, c) 30 µm, (b, d) 7.5 µm*. **(D)** Quantification of 'C' shows (a) decreased proportion of RFP-labelled AT2 (SFTPB-positive) cells in experimental versus control lungs (32.23% ± 2.94% vs. 54.34% ± 3.33%); (b) an increased proportion of RFP-labelled AT1 ($PDPN^{pos}$) cells in experimental versus control samples (19.81% ± 2.01% vs. 4.78% ± 0.17%); (c) as well as an increased proportion of RFP-labelled cells expressing both AT1 and AT2 markers in experimental versus control lungs (24.89% ± 2.88% vs. 15.59% ± 0.13%). **(**n=3; *p-value < 0.05, **p-value < 0.01).

To validate our FACS-isolation strategy, AT1 and AT2 gene signature expressions (as published by Treutlein et al. (Treutlein et al., 2014)) were assessed in isolated AT1 cells against the signature expressions in isolated AT2 cells in control lungs (n=7 samples were pooled into two samples for the gene array; Fig. S5E). (Please note, due to the extreme lack of RFP^{Pos}-labelled experimental AT2 cells, it was not possible to obtain enough mRNA to assess expression data on these experimental cells). As expected, the isolated AT1 cells showed an increased AT1 signature expression compared to the isolated AT2 cells, while the AT2 cells displayed an increased AT2 signature compared to the AT1 cells. In addition to the gene arrays, qPCR results on *Fgfr2b* expression help validate our model (Fig. S5D). In the FACS-isolated RFP^{pos} AT1 cells from experimental lungs, the expression of *Fgfr2b* is drastically reduced when compared to either the control AT1 or AT2 cells.

In addition to our FACS-based analyses, we did immunofluorescent antibody staining for PDPN (an AT1 marker) and SFTPB (an AT2 marker) on RFP^{pos} control and experimental lung sections (Fig. 22D). This strategy allowed us to identify RFP-labelled cells expressing a single marker protein (either AT1 or AT2) or expressing both markers (mixed AT1 and AT2) (Fig. 22Cb and d). Quantification of these samples (Fig. 22Da-c) showed that RFP-labelled $SFTPB^{pos}$ AT2 cells over the total RFP^{pos} pool decreased from around 54% in controls to 32% in experimental lungs; that RFP-labelled $PDPN^{pos}$ AT1 cells increased from around 5% in controls to 20% in experimental lungs; and that RFP-labelled cells expressing both markers increased from around 16% in controls to 25% in experimental samples.

Taken together, these data suggest that after cell autonomous deletion of *Fgfr2b* in $SFTPC^{pos}$ AT2 progenitor cells, these cells transition toward the $PDPN^{pos}$ AT1 lineage.

4.5.3 Cell autonomous deletion of *Fgfr2b* in $HOPX^{pos}$ AT1 progenitors pushes them toward the $SFTPC^{pos}$ AT2 lineage

To further explore the lineage-flexibility of AT2 progenitors, and to address whether a similar result was observed in AT1 progenitors, we repeated the experiments using the $Sftpc^{CreERT2}$ driver line. In addition, to label AT1 progenitors, we used a $Hopx^{CreERT2}$ driver crossed with $tdTomato^{flox/flox}$ mice to obtain control embryos and crossed with $Fgfr2b^{flox/flox}$; $tdTomato^{flox/flox}$ mice to generate experimental embryos. We assessed cells in control and experimental lungs labelled between E14.5 and E15.5 by immunofluorescence at E18.5 (Fig. 23A). Immunofluorescence antibody staining was used to identify HOPX (Fig. 23Ba-d) and SFTPC (Fig. 23Ce-h) in control (n=3) and experimental (n=3) lungs for each driver line. Asterisks indicate lineage-labelled AT1 or AT2 cells. Counting lineage-labelled cells showed that for the $Sftpc^{CreERT2}$ driver line, the percentage of double positive AT1 cells ($HOPX^{Pos}$ $RFP^{Sftpc\text{-}Cre}$ (read: HOPX-positive cells RFP lineage-labelled from the SFTPC driver)) over the total pool of RFP lineage-labelled cells significantly increased from around 20% to 33% in experimental lungs (Fig. 23Da); whereas the level of labelled AT2 cells ($SFTPC^{Pos}$ $RFP^{Sftpc\text{-}Cre}$) decreased from around 81% to 67% in experimental lungs (Fig. 23Db).

For the *Hopx*^{CreERT2} driver line, the percentage of labelled AT1 cells (HOPX^{Pos} RFP$^{Hopx\text{-}Cre}$) from the total RFP pool tended decreased from around 77% to 60% in experimental lungs (Fig. 23Ea), whereas a significant increase in labelled AT2 cells over total labelled cells (SFTPC^{Pos} RFP$^{Hopx\text{-}Cre}$/RFP^{Pos}) was observed (from around 29% in controls to 36% in experimental samples) (Fig. 23Eb).

The results found for both driver lines were independent of proliferative or apoptotic effects (Figs. S6 and S7), as staining for either Ki67 (Figs. S6B and S7B) or TUNEL (data not shown) on lineage-labelled cells, respectively, revealed no changes in expression between control and experimental groups (Figs. S6C and S7C).

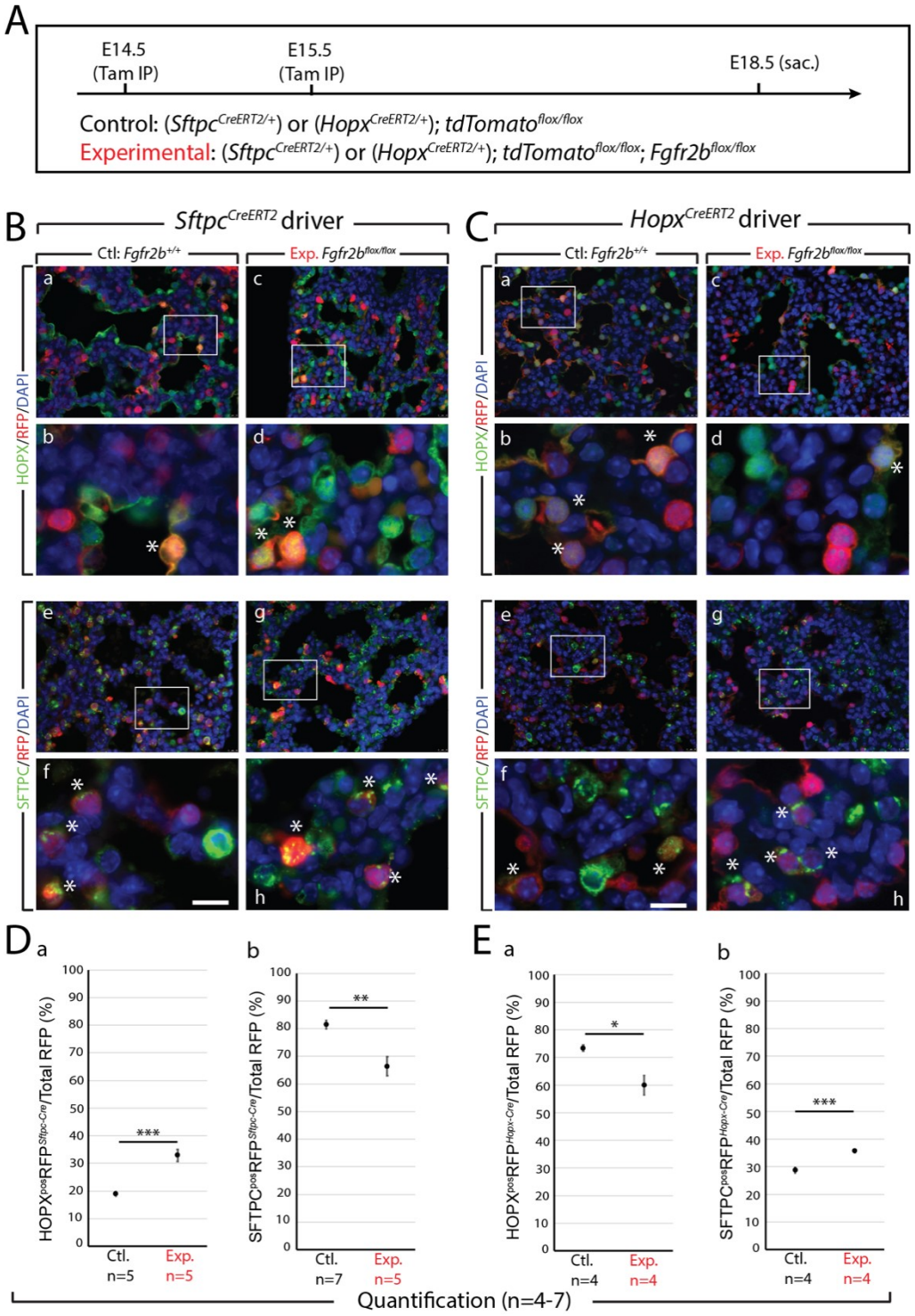

Figure 23 – Analysis of *Fgfr2b* deletion in AT2 and in AT1 progenitors. (A) Experimental design. Pregnant females carrying either control or experimental embryos were injected with TAM-IP at E14.5 and E15.5, and embryonic lungs were harvested at E18.5. **(B and C)** Representative images of control and experimental samples from the *Sftpc*^{CreERT2} (B) and *Hopx*^{CreERT2} (C) driver lines. Immunofluorescence staining of either AT1 cells (HOPX; B and C panels a-d) or AT2 cells (SFTPC; B and C panels e-h) in control (B and Ca, b and e, f) and experimental (B and Cc, d and g, h) lineage-labelled (RFP) samples. Asterisks indicate double

positive cells. *Scale bar:* (a, c, e, g) 30 µm, (b, d, f, h) 7.5 µm. **(D and E)** Quantification of samples from the *Sftpc*^{CreERT2} driver line (D) and from the *Hopx*^{CreERT2} driver line I. In the *Sftpc-CreERT2* driver line (D), (a) the percentage of HOPX^{pos} lineage-labelled RFP^{pos} cells over the total number of RFP^{pos} cells increases in experimental versus control lungs (33.25% ± 2.08% vs. 19.99% ± 0.89%); (b) whereas the percentage of lineage-labelled SFTPC^{pos} cells decreases in experimental versus control samples (66.57% ± 3.32% vs. 80.98% ± 1.49%). I In the *Hopx-CreERT2* driver line, (a) the percentage of HOPX^{pos} lineage-labelled RFP^{pos} cells over the total number of RFP^{pos} cells decreases in experimental versus control lungs (60.37% ± 3.35% vs. 77.38% ± 0.98%); (b) while the percentage of RFP-labelled SFTPC^{pos} cells increases in experimental versus control samples (36.05% ± 0.52% vs. 28.84% ± 0.96%). (n=4-7; *p-value < 0.05, **p-value < 0.01, ***p-value < 0.001).

In addition to these loss-of-function experiments, we made use of a gain-of-function mouse model (*Sftpc*$^{CreERT2/+}$*; rtTA*$^{flox/+}$*; Tg(tet(o)caFgfr1); tdTomato*$^{flox/+}$) in which expression of a constitutively active FGFR can be induced in AT2 cells with doxycycline (Fig. S8A) (Cilvik et al., 2013). This allowed us to assess whether continuous activation of FGFR signalling would suppress the commitment of labelled AT2 progenitors to the AT1 lineage. Quantification of RFP lineage-labelled cells co-stained for either HOPX or SFTPC (Fig. S8B and C) revealed a significant decrease from around 18% to 12% in the percentage of lineage-labelled AT2 progenitors committing to the AT1 lineage in experimental lungs (Fig. S8Ca); whereas the percentage of lineage-labelled SFTPC progenitors tended to increase from 83% in controls to 87% in experimental lungs (Fig. S8Cb).

To summarize, our data suggest that a significant proportion of RFP-labelled SFTPC^{pos} AT2 or HOPX^{pos} AT1 progenitors preferentially switch lineages after cell autonomous loss of FGFR2b signalling. Therefore, the decision of AT2 or AT1 progenitor cells to commit to the opposing lineage is partially regulated by FGFR2b signalling. In particular, FGFR2b signalling actively restricts the commitment of lineage-flexible alveolar epithelial progenitors to the opposing lineage.

4.5.4 Global inhibition of FGFR2b ligands reveals a set of potential direct targets of FGFR2b signalling at E16.5

To identify potential targets of FGFR2b signalling regulating the differentiation of distal airway progenitor cells at E16.5 we used the same mouse model as we did at E12.5 and at E14.5 to globally inhibit FGFR2b signalling at the protein level on the distal epithelium. Here, we injected E16.5 timed-pregnant females carrying experimental (*Rosa26*$^{rtTA/rtTA}$; *Tg(Tet(o)sFgfr2b)/+*) and littermate controls (*Rosa26*$^{rtTA/rtTA}$; *+/+*) with doxycycline intraperitoneally (Dox-IP) and harvested the embryos and their lungs nine hours later (Fig. 24A).

Macroscopically, the phenotypes of control and experimental lungs were quite similar, although the tips of the experimental buds showed the characteristic dilation of the distal lumens using this inhibitory mouse model (compare Fig. 24Bd with Bb). A gene array was conducted on whole lung homogenates from control (n=3) and experimental (n=4) embryos. A heatmap of the top 100 genes (according to p-value) differentially regulated between experimental and control samples is shown in Fig. 24C. Of these 100 genes, 72 were downregulated in experimental versus control lungs; these genes (of which only 13 can currently and reliably be classified as epithelial specific) constitute the FGFR2b signature at E16.5 (see Fig. S9). Gene ontology (Fig. 24D) and KEGG pathway analyses (Fig. 24E) of these 72 genes indicate that several biological processes are regulated by FGFR2b signalling at this timepoint. These include, in order from high to low of the number of genes involved, cellular transporting (9 genes), signal transduction (8), inflammation (7), markers of differentiation (4), transcriptional regulation (3), cell adhesion (3), interaction with nerves (3), protein processing and trafficking (2), lipid metabolism (2), response to stress (2), oxidation (2), growth factor activity (2), and transmembrane proteins (1). The pathways primarily affected by these genes include cell cycle regulation, cAMP signalling, focal adhesion, and, interestingly, hypertrophic cardiomyopathy and cardiac muscle contraction, which have been associated with the migration of AT2 progenitors out of the lumen to escape the physical forces applied by the amniotic fluid, a process regulated by FGFR2b-mediated actin/myosin-dependent mechanisms (Li et al., 2018).

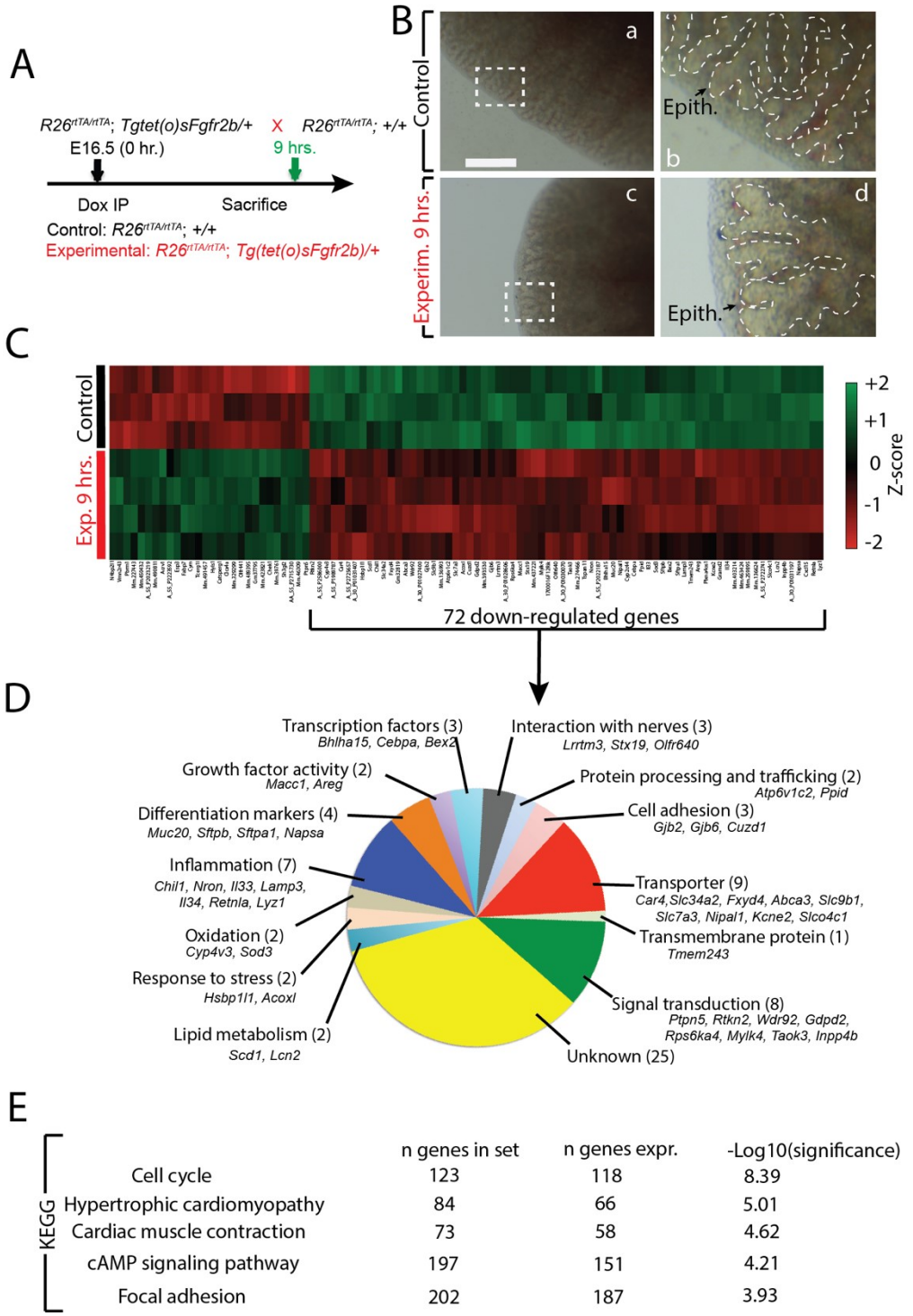

	n genes in set	n genes expr.	-Log10(significance)
Cell cycle	123	118	8.39
Hypertrophic cardiomyopathy	84	66	5.01
Cardiac muscle contraction	73	58	4.62
cAMP signaling pathway	197	151	4.21
Focal adhesion	202	187	3.93

Figure 24 – Transcriptomic changes upon FGFR2b signalling inhibition at E16.5 + 9 hours. (A) Experimental design. E16.5 littermate experimental and control lungs were collected 9 hours after a single Dox-IP injection. **(B)** Gross airway morphology (hashed line traces the epithelium) shows airway tip dilation between control (a and b) and experimental (c and d) lungs. (Epith. = Epithelium). *Scale bar:* (a, c) 500 µm, (b, d) 125 µm. **(C)** Heatmap of the top 100 genes (according to p-value) differentially expressed after 9 hours FGFR2b inhibition (n=3 control and 4 experimental). 72 of those genes are downregulated, representing potential

direct targets of FGFR2b signalling. **(D)** Gene ontology of the 72 down-regulated genes found in 'D'. **I** Top five KEGG pathways regulated from the complete gene array.

4.5.5 FGFR2b responsive genes during pseudoglandular development narrow on a subpopulation of AT2 cells at E17.5

The 72 genes identified in this study, together with the signatures found at E12.5 and E14.5, provide a valuable set of candidate transcriptional targets involved in FGFR2b signalling (See Fig. S10 for the gene signatures at each timepoint). A shortcoming of this global approach, however, is the inability to accurately characterize and assess the relative contribution to the global response from the different epithelial cell types.

One way to tackle this lack of information is to data-mine published single-cell RNA-sequencing (scRNA-Seq) datasets at different developmental time-points to obtain gene expression data for genes of interest. In this vein, we mined the recently published scRNA-Seq data from Frank et al. (2019), which contains transcriptome data from 7,106 individual *Nkx2-1*-positive epithelial cells obtained from E17.5 mouse lungs (GEO accession code GSE113320). Of the 11 categories denoted by the authors, four are of interest to us here: AT1 precursor (preAT1), AT1, AT2 precursor (preAT2), and AT2 (Frank et al., 2019). These groups are depicted and colour-coded in Supplementary Figure S11A, along with the expressions of the AT2 markers *Sftpc* and *Lamp3,* and the AT1 markers *Ager* and *Aqp5* (Fig. S11B), as well as the expression of *Fgfr2* and the well-established downstream effector of FGFR2b signalling, *Etv5* (Fig. S11C). Note the comparable expressions of *Fgfr2* in preAT2 and AT2 cells, but also the presence of this gene in preAT1 cells. Finally, we assessed the expression in the four clusters of the signature gene sets we discovered at E12.5, at E14.5, and at E16.5 (Fig. S11D-G). As the gene sets approach the timepoint of the sequenced single cells (E17.5), the expression profile becomes increasingly concentrated in a subset of the preAT2 and AT2 clusters (Fig. S11G). This finding suggests that the FGFR2b signalling target genes discovered using our global FGFR2b ligand inhibition model at E16.5 are predominantly expressed by a subset of the AT2 lineage at E17.5.

Following the identification of a subset of cells within the AT2 lineage which highly express the FGFR2b signature at E16.5, we reanalyzed the mature AT2 cluster (cluster 4 from Frank et al. (2019)). We found that this cluster groups into two subclusters, which we have termed cluster A and cluster B (Fig. 25A). We created a heatmap showing the top 50 differentially upregulated genes in each cluster (according to average Log_{10}fold change) (Fig. 25B). While canonical markers of AT2 cells, such as *Sftpc*, *Sftpb*, *Sftpa1*, and *Lamp3* are expressed in each subcluster, they are more highly expressed in cluster B (Fig. 25C), suggesting that cluster B might represent a more mature pool of AT2 cells. Interestingly, the genes most highly expressed in cluster A are predominately markers of the AT1 lineage. Indeed, assessing the expression of the AT1 and AT2 signature genes published by Treutlein et al. (2014) in clusters A and B reveals a stark contrast between the two clusters: cluster A is highly enriched in AT1 marker genes, whereas cluster B expresses the AT2 signature (Fig. S12A and B). In fact, a closer look at the AT2 signature in cluster B reveals that this cluster is composed of at least two more subgroups defined by signature gene-expressing cells. Finally, while *Fgfr2* and *Etv5* expressions are scattered somewhat uniformly throughout clusters A and B (Fig. 25C), the targets of FGFR2b signalling from E14.5 to E16.5 concentrate ever more narrowly in a subcluster of cluster B. The characterization of this FGFR2b responding subcluster remains to be determined. One hypothesis is that cluster A or B might contain the recently published 'injury-activated alveolar progenitors (IAAPs)' (Ahmadvand et al., 2021), albeit at an early stage of development. Figure S12C and D provide some preliminary data suggesting the equivalent of activated IAAPs might be found in the subcluster of cluster B, which also contains the aforementioned *bona fide* AT2 signature and FGFR2b signature activity.

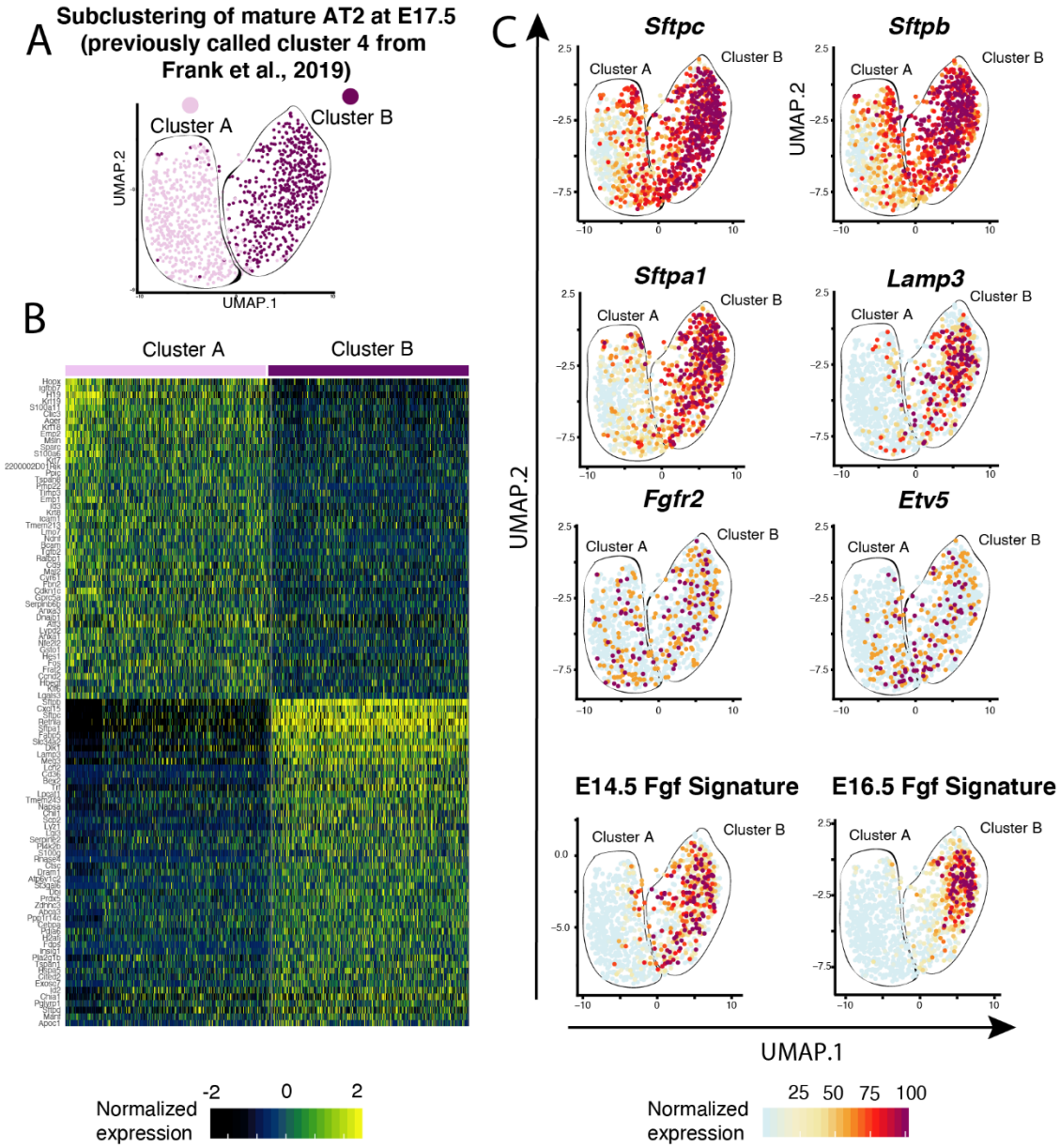

Figure 25 – FGFR2b signature concentrates on a subcluster of mature AT2 cells at E17.5. (A) Subclustering of mature AT2 cells as identified by scRNA-seq at E17.5 (Frank et al., 2019) (GEO accession code GSE113320). The cells cluster into two discrete subclusters, termed A and B. **(B)** Heatmap showing the 50 upregulated genes in each subcluster, according to Log_{10}fold change. While subcluster B is enriched in canonical AT2 marker genes, subcluster A shows enrichment in AT1 markers (see Fig. S8). **(C)** The expression profiles of select genes in subclusters A and B show high expression of markers for mature AT2 cells in cluster B: *Sftpc, Sftpb, Sftpa1* and *Lamp3*. Note how *Fgfr2b* and *Etv5*, markers for FGFR2b signalling, are scattered throughout subclusters A and B, while the FGFR2b signalling signatures determined by our lab at E14.5 and at E16.5 concentrate on a subcluster of cluster B.

In summary, using published scRNA-seq data from E17.5 mouse lungs, we were able to identify subclusters of cells based on FGFR2b signature genes over pseudoglandular development. These subclusters emerge from previously designated 'mature AT2s' (Frank et al., 2019), which, upon further subgrouping, can be divided into two major subclusters. One of those subclusters displays AT1-like gene expression patterns, while the other seems to contain *bona fide* AT2s. Within the AT2 cluster, an additional subcluster exists which is high in FGFR2b responding cells, and to a lesser extent, activated IAAPs. These data highlight the extreme heterogeneity inherent in the alveolar cell lineages, and the issues such heterogeneity raises in classifying these cells.

4.5.6 AT2 cells lose FGFR2b signalling as they transition to AT1 during repair after injury in the adult lung

A recent publication assessed the cell-type specific transcriptomic sequences involved in the regeneration of the airway after bleomycin-induced injury (Strunz et al., 2020). Using a combination of longitudinal scRNA-seq data (GEO accession code GSE141259), RNA trajectory modelling in pseudotime, as well as lineage tracing experiments, the authors demonstrated that during lung regeneration, populations of airway and AT2 stem cells converged on a transitional cell-type characterized by high *keratin 8* (*Krt8*) expression. These *Krt8*-positive airway differentiation intermediate (*Krt8*^{Pos} ADI) cells eventually gave rise to AT1 cells during repair of the gas exchange surface. Since FGFR2b signalling plays a critical role in the differentiation of pneumocytes during normal development, it is also likely involved during repair after injury. Therefore, we investigated the expression levels and locations of the FGFR2b signatures found at E12.5, E14.5, and at E16.5, in adult lung cells following bleomycin injury using this published scRNA-seq dataset.

Figure 26A reproduces the UMAP from the original Strunz et al. (2020) study and highlights the FGFR2b signatures we found at E12.5, E14.5, and E16.5. As can be seen, the signatures from each embryonic developmental stage increasingly concentrate on the AT2 and AT2-activated cell populations found during homeostasis and during repair after bleomycin-induced injury (Fig. 26B and C). Note that the E12.5 signature is nearly equally present in AT1, AT2, and AT2-activated cells (left column in Fig. 26B). As development progresses through

E16.5, FGFR2b signalling concentrates on the AT2 and AT2-activated populations (Fig. 26C), with a minor scattering of expression in KRT8^{Pos} ADI cells and mature AT1 cells. Indeed, as AT2 stem cells transition through a KRT8^{Pos} ADI state towards an AT1 fate, FGFR2b signature gene expression is significantly decreased (Fig. 26D and Fig. S13). These findings suggest that FGFR2b signalling acts on the AT2 pool during homeostasis but is lost in AT2 cells transitioning to the AT1 pool during repair after injury. Therefore, in the adult lung, as during development, FGFR2b signalling might actively prevent AT2 cells from transitioning to an AT1 fate during homeostasis.

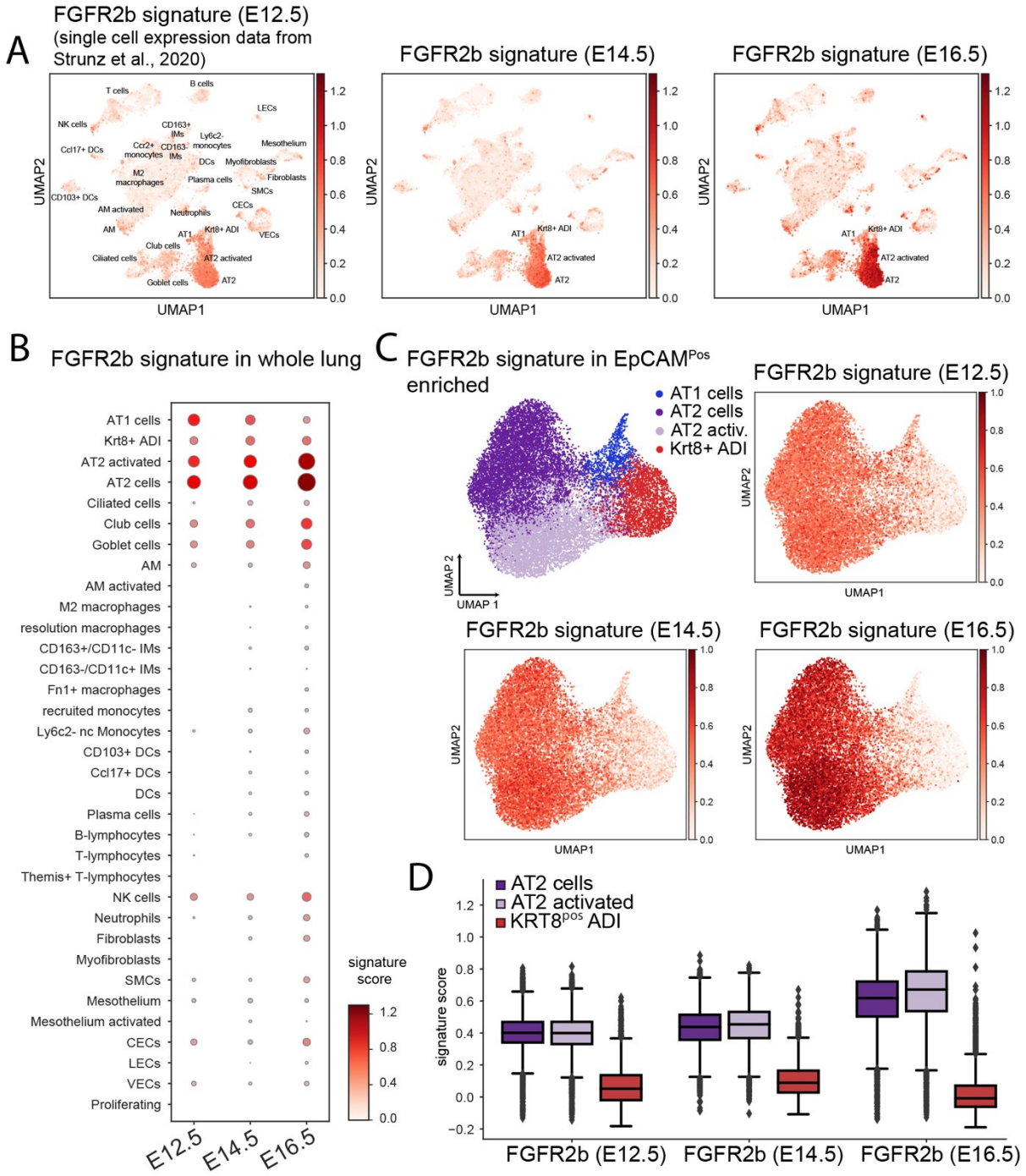

Figure 26 – FGFR2b signalling is lost in AT2 cell transition to AT1 during repair after injury. **(A)** scRNA-seq data from Strunz et al. (Strunz et al., 2020) (GEO accession code GSE141259) reanalyzed using the FGFR2b gene signatures found by our lab at E12.5, E14.5, and E16.5. Note the increasing expression of these signature genes as embryonic development progresses in the AT2 clusters. **(B)** Dot plot showing the different cell categories from 'A' and the relative FGFR2b signature scores at each embryonic timepoint in each category. **(C)** The FGFR2b signature from different embryonic timepoints (E12.5, E14.5 and E16.5) concentrate in the AT2 clusters of EpCAM^{pos} enriched alveolar cells. **(D)** Box and whisker plots of the AT2 clusters, along with the KRT8^{pos} ADI cluster found in 'C' showing the FGFR2b signature score at the given

timepoints. While each embryonic FGFR2b signature remains relatively high in the AT2 cells, each is virtually non-existent in the transitional KRT8^{pos} ADI cluster.

5 Discussion

5.1 Validation and limitations of *in vivo* FGFR2b signalling inhibition using the dominant negative soluble FGFR2b model

A potential limitation of the dominant negative *in vivo* model to inhibit FGFR2b signalling during embryonic and pseudoglandular stage lung development is that the production of soluble FGFR2b is global, being expressed by every cell. Furthermore, sFGFR2b is secreted into the mesenchyme, which could potentially inhibit mesenchyme-specific FGF signalling. This could potentially have secondary effects, especially the longer the system is active. Indeed, it has been demonstrated that in rats, FGF10 directly acts on the lung mesenchyme during the late canalicular/early saccular stage (E19) to control the differentiation of lipofibroblast progenitors (Al Alam et al., 2015). However, in earlier experiments done on isolated mid-pseudoglandular stage (E14.5) mouse primary mesenchymal cells treated with rFGF10, no significant increase in phospho-ERK signalling (which is a readout for FGF10 signalling) was observed (De Langhe et al., 2006). Since one cannot exclude that FGF10 is active on discrete mesenchymal subpopulations throughout pseudoglandular stage development, more stage-specific work needs to be done to characterize the other cell populations responding to FGF ligands.

Throughout this thesis, to control for the potential secondary effects of our dominant negative mouse model, we tried to validate the cell-types of the primary targets whenever possible. For example, we made use of a gene array comparing gene expression profiles in isolated mesenchyme vs. epithelium from E12.5 wildtype lungs (data not shown; see Jones et al., 2019a). This information, combined with our use of *in situ* expression profiling from the 'Genepaint' database, enabled us to increase our confidence concerning the cellular compartments targeted by FGFR2b signalling in our pseudoglandular stage experiments. Finally, as detailed in the 'Results' section (Fig.12E-G), we queried our E12.5 gene array data to reconstruct the well known FGF10/SHH regulatory signalling axis. Taken together, we are confident that our global *in vivo* inhibition of FGFR2b ligands for 9 hours does indeed detect the impacts of FGFR2b signalling primarily on epithelial-specific targets.

5.2 Targets repressed by FGFR2b signalling

Throughout this thesis, I have only considered the target genes induced by FGFR2b signalling (downregulated upon FGFR2b ligand inhibition). This choice was made to make the analyses of our gene arrays, and the interpretation of the data, more manageable. However, the target genes repressed by FGFR2b signalling during development are equally important to consider.

In Figure 27, a preliminary analysis comparing the genes upregulated after FGFR2b signalling inhibition for 9 hours is found. These genes come from the heatmaps depicted in Figures 12, 15, and 24. As can be seen, only two genes are shared between the E12.5 and E14.5 timepoints (contrast this to the 12 downregulated genes shared between these two timepoints, Fig. S10), whereas only one gene (*Cym*, involved in cellular metabolism) is shared between all three timepoints. Interestingly, no genes are shared between E14.5 and E16.5 (compare this to the 11 downregulated genes shared between these two timepoints, Fig. S10).

Finally, gene ontology analysis indicated that the genes upregulated in our gene arrays are involved in many of the same biological processes found with the downregulated genes. However, genes involved in cellular metabolism appear to be relatively highly represented in the set of upregulated compared to downregulated genes. This suggests that during normal pseudoglandular lung development, FGFR2b signalling effects metabolism by repressing metabolism-specific genes.

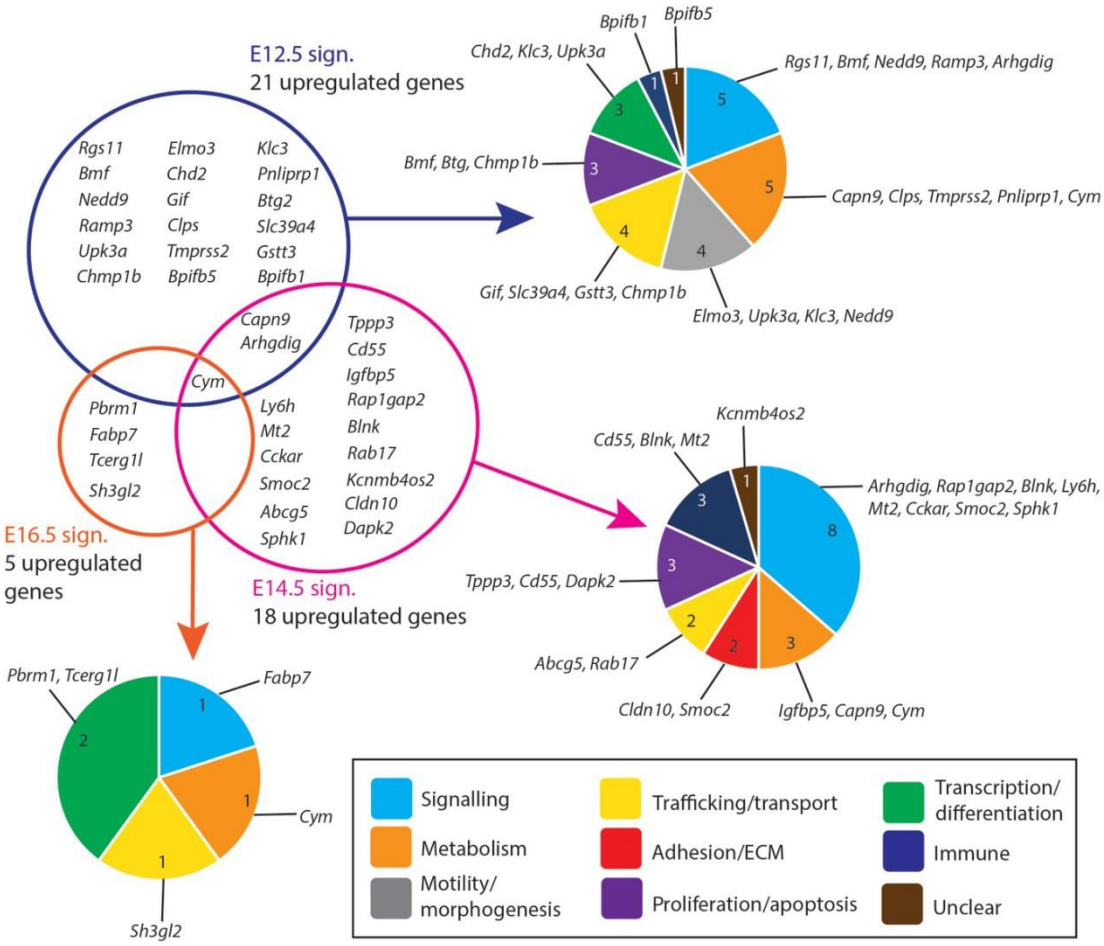

Figure 27 – Comparison of the genes upregulated upon FGFR2b ligand inhibition at E12.5, E14.5, and E16.5. The Venn diagram shows the upregulated genes specific to each timepoint and those shared between and among timepoints (blue – E12.5; pink – E14.5; orange – E16.5). A pie chart shows the primary biological activities regulated by these genes at each timepoint. See text for more discussion.

5.3 Embryonic and early pseudoglandular stage lung development (E9.5-E11)

The data presented in this manuscript indicate that during the E9–E11 time period, FGFR2b signalling plays several functions, one of which is the control of lobar septation between E9-E10.5 (Figs. 9 and 10). Lobar septation is the process by which the right lobe of the mouse separates into the cranial, medial, caudal, and accessory lobes. Septation appears to be independent of branching morphogenesis, which is yet to begin at these earliest of lung development stages (Bellusci et al., 1997).

Of the four right lobes, it is the accessory lobe which seems to be the most impacted by loss of FGFR2b signalling. Consider the impacts on the lobe when assessed at E17-E18.5 from a single Dox-IP at E9.0 (where this lobe develops relatively normally) and at E9.5 (where it fails to form) (compare Figs. 9B and 10B). Analysis of the lung branching pattern during early lung development indicates that the accessory lobe starts to form only after E10.5 (Bellusci et al., 1997), thereby providing a reasonable explanation concerning the formation of a relatively normal accessory lobe following FGFR2b signalling inhibition from E9 to E10 (E9.0 Dox-IP), but lobar agenesis from E9.5 to E10.5 (E9.5 Dox-IP).

We have previously reported that at E14.5, FGF10 expression is found at the edges of the intralobular segments in the lung (Mailleux et al., 2005; El Agha et al., 2012) indicating that FGF10 could play a direct role not only in subdividing the initial rudimentary right lobe in smaller lobes through the process of lobar septation, but also the smaller lobes in lobules through a process of lobular septation. Furthermore, we have shown that *Fgf10* expression, using *in situ* hybridization in the early mouse lung (E9.75–E11.5), is relatively high in the mesenchyme of the distal tip at E9.75, and appears to be more expressed in the right bronchi than in the left bronchi. This expression pattern seems to be the case up to E12.5 (Bellusci et al., 1997). Taken together, regional expression of FGF10 may therefore explain the lobular septation phenotype affecting the right lung.

Between E9.5-E10.5 (E9.5 Dox-IP), our results indicate that FGFR2b signalling is not only required for lobar septation, but for lobe growth as well (Fig. 10). Here, the impacts of inhibition during this time period are reversible, as the lungs are functional at birth (data not shown) and display normal epithelial differentiation (Fig. 10i-p). By contrast, inhibition from E11 to E12 (E11 Dox-IP) leads to a complete arrest in the development of the lung leading to lethality at birth (Fig. 11). These observations not only highlight the different roles played by FGFR2b during this early developmental stage, but also how rapidly the mouse lung progresses through different developmental stages.

5.3.1 Comparing mouse to human lung developmental stages

It is generally thought that stages of mammalian lung development are comparable among species (Schittny, 2017). Rodents, in particular, have been extensively used to study the basics of lung development, and have served as models for human lung diseases and disorders. However, the success of translating these findings to the human context has been limited (Wong et al., 2019). Herein lies a critical issue for translational research: do mouse models accurately recapitulate what happens during human lung development, and if so, which stages and mechanisms are comparable?

Work by our group has shown that the effects of rFGF10 on the branching of 12 weeks-old human fetal lungs (which are assumed to correspond to the pseudoglandular stage in the mouse) were negligible, while mouse lungs at E12.5 responded as expected, by increased branch formation (Danopoulos et al., 2019). Therefore, it is potentially inaccurate to compare human fetal lungs at 12 weeks of gestation versus mouse lungs at E12.5, as they could correspond to two distinct developmental phases of lung development. The work contained in this thesis demonstrates an embryonic stage in mice, where FGFR2b signalling plays roles other than those related to branching morphogenesis. Therefore, it could be more relevant to compare the impact of FGF10 signalling in 12 weeks-old fetal human lungs with a mouse lung at the embryonic stage (E9–E10). Another important and relevant question concerns the duration of the pseudoglandular stage in human lung development, which is supposed to encompass week 4 through week 17 of gestation. Based on FGF10 activity as a read out, our results suggest that at 12 weeks of gestation, the human lungs are still in the equivalent of an “embryonic phase” (Danopoulos et al., 2019). It is therefore still unclear when the pseudoglandular phase starts in humans. It is worth noting that mid-gestation in mice is E9.5, where the lungs are not yet formed, nor could the pups possibly survive premature birth. In contrast, mid-gestation in humans is about 20 weeks of gestation, close to the limit of viability of severely premature babies. In the interest of sound and valid translational studies, more molecular and cellular insights into the different developmental stages, particularly the embryonic and pseudoglandular phases, are clearly needed.

5.4 Early pseudoglandular stage lung development (E12.5)

In this thesis, *in vivo* experiments inhibiting FGFR2b ligands at E12.5 resulted in arrested epithelial branching and collapsed distal bud lumens associated with abnormal cellular adhesion (Fig. 13). Gene arrays at 6 and 9 h inhibition revealed the transcriptomic regulation of FGFR2b signalling (Fig. 12). From these arrays, we identified an FGFR2b gene signature primarily composed of genes enriched in the epithelium. Finally, data on SOX9 and SOX2 expression, as well as gene-set analyses on differentiation markers of AT2 cells, which are found to be expressed in multipotent epithelial progenitor cells, demonstrate the proximalization of the tip epithelium and a loss of distal differentiation markers 9 h after FGFR2b inhibition (Fig. 14).

5.4.1 FGFR2b primary transcriptional targets

The 'FGFR2b gene signature' at E12.5 contains genes primarily enriched in the epithelium, which show decreased expression shortly after FGFR2b ligand inhibition, and which continue to decrease during inhibition; therefore, these genes likely represent primary targets and potential key mediators of FGFR2b signalling.

Not shown in the 'Results' section of this thesis was the response to FGFR2b signalling inhibition on the expression of known transcription factors in the mouse lung at E12.5 (these results were covered in detail in a previous thesis, and can be found in Jones et al., 2019a). Herriges et al., (2012) found that of the 1100 transcription factors they searched for in the developing mouse lung (which accounts for around 90% of known transcription factors in the mouse genome), only 62 exhibited localized expression in the epithelium and/or mesenchyme. From our gene array, only 11 significantly regulated genes were exclusively or predominantly expressed in the epithelium of E12.5 lungs. Apart from the expected regulation of genes such as *Etv4, Etv5, Sox2* and *Sox9*, the other genes included *Grhl2*, *Nkx2-1*, *Id2* (all repressed by loss of FGFR2b signalling), as well as *Nkx1-2, Pitx2*, *Lmo1* and *Elf5* (all induced by loss of FGFR2b signalling).

Little is known of the transcription factors apart from the *Etv* and *Sox* genes during early pseudoglandular stage lung development. Knock-out and over-expression studies on many of our identified transcription factors showed impacts very similar to the effects seen in our study. For example, Metzger et al. (2007, 2008a) found that *Elf5 was* regulated by FGF10 and FGF7, and that over-expression of ELF5 led to branching defects and delayed AT2 differentiation; Quaggin et al. (1999) reported that *Tcf21* knock-out mice displayed reduced branching, smaller lungs, and a proximalization of lung epithelium at E14.5; finally, Varma et al. (2012) studied the transcription factor *Grhl2* during lung development, and found that GRHL2 controlled cell adhesion and migration, formed a positive feedback loop with NKX2-1 during branching morphogenesis, and was associated with proper AT2 differentiation. Given the paucity of studies of these genes during early mouse lung development, we propose that the set of target genes and transcription factors identified in our study is a valuable resource for future investigations on early lung branching morphogenesis and differentiation.

5.4.2 FGFR2b regulation of tip cell differentiation and morphology *via* SOX9

Sustained SOX9 expression in the tip epithelium of the developing lung has been associated with epithelial stem cell self-renewal. The general model predicts that individual tip cells, under the influence of FGF10/FGFR2b signalling, are prone to remain in the tip domain; as these cells divide, some of the daughter cells acquire bronchial progenitor characteristics associated with the exit from the tip domain. The transcription factor SOX9 has been extensively studied during early lung development (Perl et al., 2005; Chang et al., 2013; Rockich et al., 2013). For example, Chang et al. (2013) found that knocking out *Sox9* before E12 led to branching defects, an increase between the distal epithelium and mesothelium, and smaller lungs. Furthermore, it was found that FGFR2b signalling regulated *Sox9*, and that SOX9 suppressed the initiation of alveolar differentiation. Rockich et al. (2013) found similar results, and also assessed the impacts on cell adhesion in *Sox9* loss-of-function E14.5 lungs. Using TEM, the authors found multiple cellular defects similar to what we found in our *in vivo* model, including: irregularly shaped epithelial cells, gaps with protruding pseudopodia between adjacent cells, partial to complete loss of microvilli, and a disjointed basement membrane filled with gaps (Figs. 13 and S2). As SOX9 was lost in the distal epithelial cells of experimental lungs, the expression of SOX2 in these cells increased, further suggesting these

cells were losing their multipotency, and were adopting a proximal fate. This idea is supported by the evidence, at this stage, of a loss of the AT2 signature in the multipotent progenitors upon FGFR2b ligand inhibition. Therefore, our data suggest that the loss of SOX9, downstream of FGFR2b signalling, affects the morphogenesis and multipotent potential of distal epithelial cells.

5.5 Mid-pseudoglandular stage lung development (E 14.5)

Transient inhibition of FGFR2b signalling at E14.5 for 9 hrs., 24 hrs., and after 4 days, as well as continuous inhibition for 4 days revealed a set of transcriptional targets and biological activities related to, yet different from, those found at E12.5. This fact is captured in the comparison of gene signatures between E12.5 and E14.5 (Fig. 16C). While the primary biological activity of FGFR2b signalling at E12.5 is related to branching morphogenesis (focal adhesion, regulation of actin cytoskeleton, cell/cell and cell/ECM adhesion), the emphasis of FGFR2b signalling at E14.5 is on cellular proliferation and differentiation. The most significantly regulated genes at E14.5 are not the same as those at E12.5. This difference is evident in the KEGG pathways regulated at each timepoint, with pathways related to cell–cell and cell–extracellular matrix adhesion being significantly regulated at E12.5, and pathways related to cellular proliferation being most significant at E14.5 (Fig. 16). These differences translate at the cellular and morphological levels as well: inhibition of FGFR2b ligands at E12.5 for 9 hrs. produced clear and drastic effects on branching morphogenesis without affecting proliferation or apoptosis, while inhibition of FGFR2b ligands at E14.5 for 9 hrs. did lead to significant regulation of cellular proliferation, in both the epithelium and the mesenchyme (Fig. 17). In line with the general theme of our work during early lung development, these findings at E14.5 highlight the overlapping, yet shifting primary biological effects and direct transcriptomic targets of FGFR2b signalling within a relatively short developmental timeframe.

Another important aspect of our work at E14.5 is linked to the formation of the alveolar epithelial lineage. Our results indicate that one of the immediate effects of FGFR2b signalling at E14.5 is to control the proper differentiation of AT2 progenitor cells, while AT1 progenitors appear unaffected (Fig. 15 and 18). However, long-term inhibition of FGFR2b signalling

beginning at E14.5 clearly also impacts the AT1 lineage (Fig. 19). We therefore conclude that at E14.5, FGFR2b signalling is important for the formation of both the AT2 and the AT1 lineages. This evidence supports the work we conducted at E16.5 in this thesis, wherein we assessed the role of FGFR2b signalling in both the AT1 and AT2 lineages.

In summary, our research offers novel insights into the roles of FGFR2b signalling during embryonic and early to mid-pseudoglandular stage lung development. Our data has revealed some of the convergent and divergent sets of biological activities and transcriptomic targets among the different timepoints. The results suggest that stage-specific FGFR2b signalling activities may be at play beginning from the embryonic through to the early and mid-pseudoglandular stages of lung development. Figure 28 summarizes these findings. Further studies will have to be conducted to elucidate the shifting roles of FGFR2b signalling at successive stages (canalicular/saccular/alveolar) of lung development as well as during homeostasis and regeneration/repair after injury.

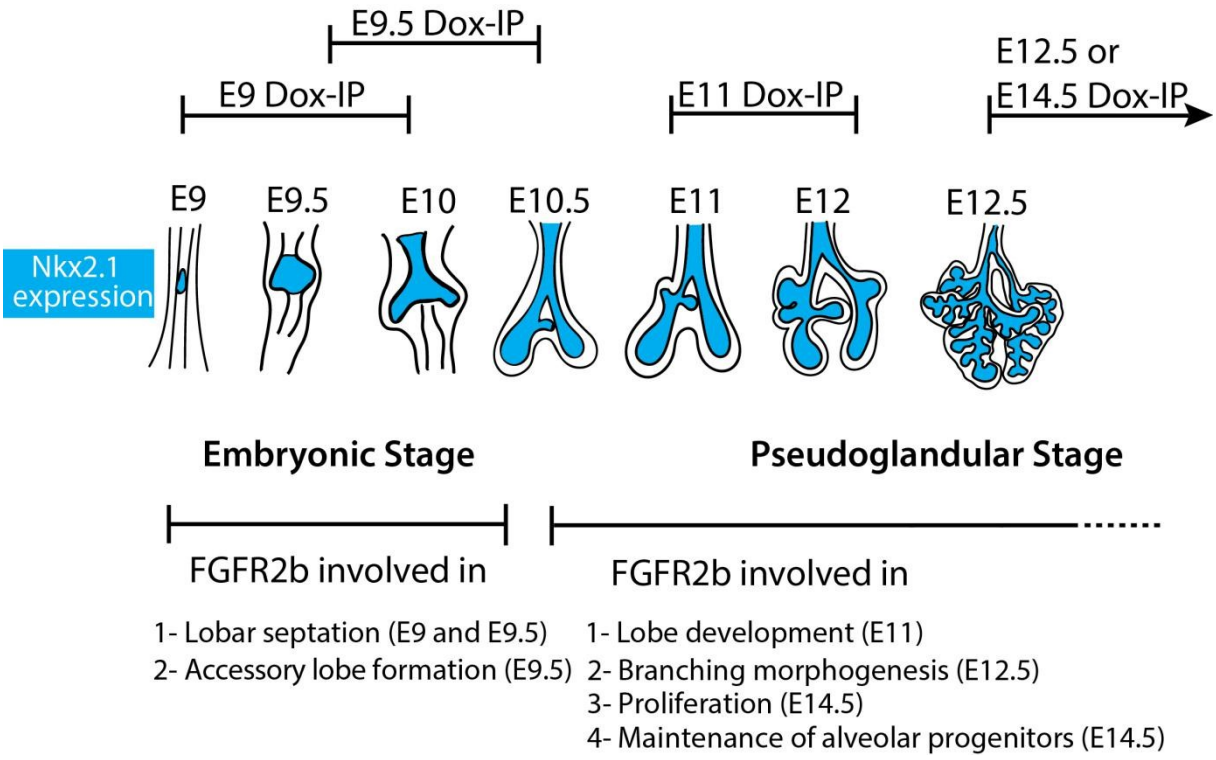

Figure 28 – Schematic summary of FGFR2b signalling regulation during embryonic (E9.5) and early (E12.5) to mid-pseudoglandular (E14.5) lung development. The impacts of attenuating FGFR2b ligand activity at different developmental timepoints (E9, E9.5, E11, E12.5, and E14.5) illustrates the shifting biological functions of FGFR2b signalling within a relatively short developmental timeframe. During the embryonic stage (E9-E10.5), FGFR2b regulates lobar septation, as well as the formation of the accessory lobe between E9.5 and E10.5. During the early pseudoglandular stage (E10.5-E12.5), lobar development depends on FGFR2b signalling between E11 and E12, while branching morphogenesis is highly regulated at E12.5 The primary role of FGFR2b signalling shifts to cellular proliferation at E14.5, while impacts on the alveolar lineages are increasingly pronounced at this stage as well.

5.6 Late pseudoglandular stage lung development (E16.5)

Our work at E14.5 suggested that the differentiation of AT1 and AT2 progenitors is impacted by loss of FGFR2b signalling at this stage. By using cell-autonomous models to delete *Fgfr2b* and label targeted cells, we were able to directly assess at E18.5 the role of FGFR2b signalling in alveolar progenitors between E14.5 and E16.5 (E14.5 and E15.5 Tam-IP). We found that both AT1 and AT2 progenitors show a level of inter-lineage flexibility, in that around 20%-30% of labelled progenitors will give rise to the opposing lineage at E18.5 (Fig. 21). This was shown to be controlled in part by FGFR2b signalling. In the case of AT2 progenitors, loss of *Fgfr2b* led to an increase in the commitment of labelled cells to the AT1 lineage (Figs. 22 and 23). This was supported by gain-of-function of FGFR signalling, whereby less cells committed to the opposing lineage (Fig. S8). In the case of AT1 progenitors, the opposing results were observed; loss of *Fgfr2b* in labelled AT1 progenitors led to an increase in committed AT2 cells (Fig. 23). Thus, FGFR2b signalling maintains the stability of both the committed AT1 and AT2 cell lineages during late pseudoglandular stage lung development. These results are summarized in the model in Figure 29.

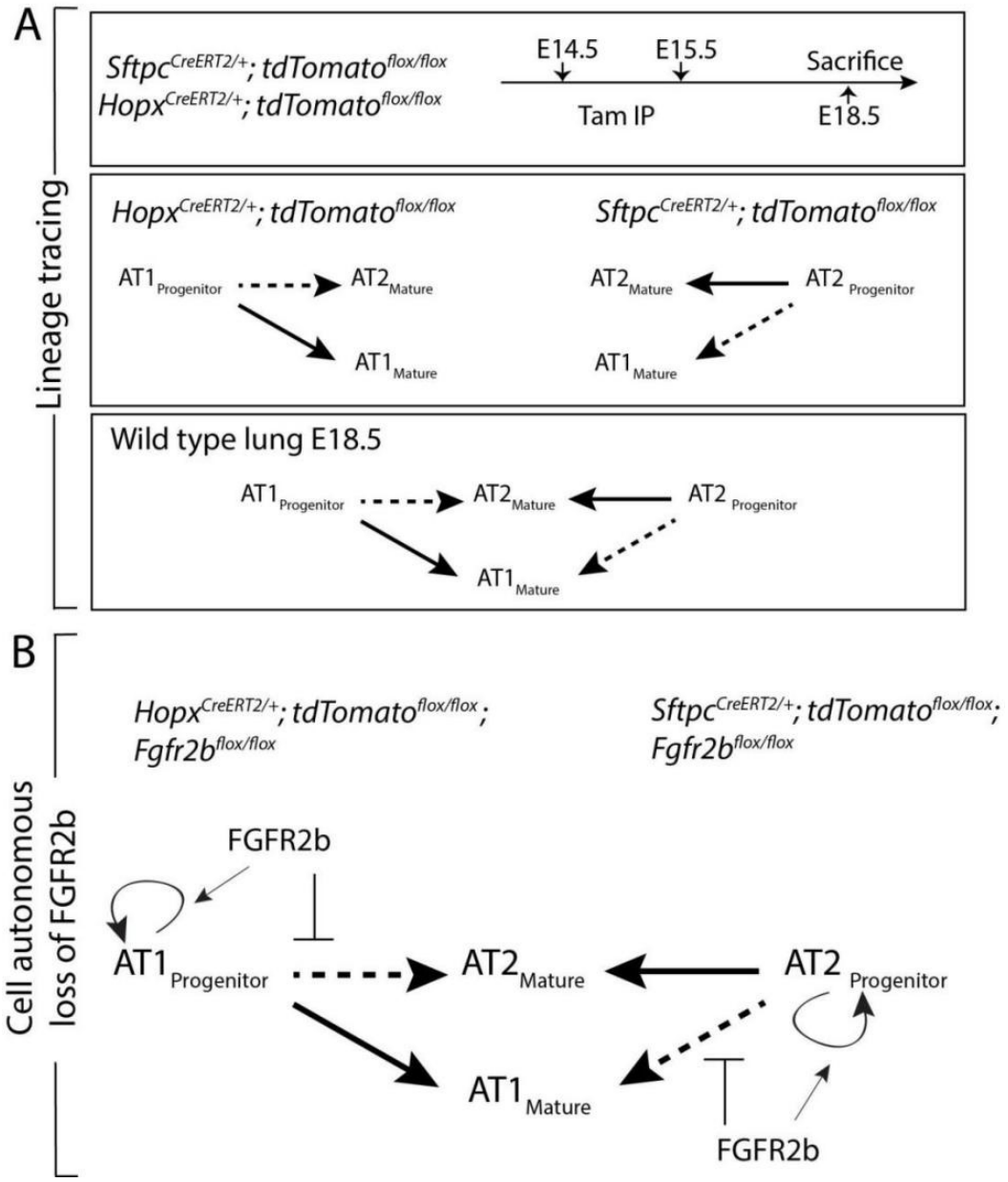

Figure 29 – Model of FGFR2b regulation of alveolar epithelial lineage formation. (A) Lineage tracing at E14.5 and E15.5 (late pseudoglandular/early canalicular) (first panel) shows that labelled AT1 progenitors give rise primarily to mature AT1s at E18.5 (solid arrow) and contribute a significant minority to the AT2 lineage (dashed arrow), while the reverse is true for labelled AT2 progenitors (second panel). Taking the lineage tracing data together, we propose the model in the third panel of alveolar epithelial progenitor contribution to mature alveolar epithelial cells in wild type lungs at E18.5. **(B)** Cell autonomous deletion of *Fgfr2b* experiments suggest that, apart from the expected impacts of FGFR2b signalling on alveolar epithelial progenitor proliferation, FGFR2b prevents alveolar epithelial progenitors from actively transdifferentiating to the opposing lineage.

Furthermore, to obtain a set of FGFR2b targets likely involved in alveolar lineage formation during E16.5 development, we used our well-established dominant negative mouse model to inhibit FGFR2b signalling in E16.5 lungs for 9 hrs. From this, we identified a set of downregulated genes which we termed the 'E16.5 FGFR2b signature' (Fig. 24). This signature, along with the signatures we had previously found at E12.5 and at E14.5, was used to data-mine published scRNA-seq datasets. We found that FGFR2b responsive genes cluster at E17.5 into a subcategory of previously classified 'mature AT2s' (Figs. 25, S11 and S12). Finally, we found that in a model of lung repair after injury in adult mice, the FGFR2b signature genes are effectively lost in AT2 cells transdifferentiating to AT1 cells (Figs. 26 and S13). This finding supports the evidence found during development that FGFR2b signalling prevents AT2 cells from differentiating to AT1s.

5.6.1 Cross contribution of AT1 and AT2 progenitors to the opposite lineages

The relative contribution of the early alveolar progenitors to the AT1 and AT2 lineages remains controversial. What proportion of mature alveolar epithelial cells pass through a bipotential progenitor, for example? Do bipotential cells represent a major progenitor pool, as was earlier argued (Treutlein et al., 2014), or a minor subsidiary contributor to mature alveolar epithelial cells, as was later proposed (Frank et al., 2019)? While the work presented in this thesis does not directly address the question of bipotential progenitors, it does suggest that a significant proportion (around 20%-30%) of committed (at E18.5) AT1 and AT2 cells derive from lineage-flexible progenitors expressing an opposing alveolar epithelial cell marker. This calls into doubt the model of early alveolar lineage specification, which posits that the vast majority of alveolar cells are lineage committed as early as E13.5 (Frank et al., 2019). Furthermore, the paper from Frank et al. (Frank et al., 2019) shows that around 63% of dual-traced ($HOPX^{pos}$ $SFTPC^{pos}$) progenitors give rise to mature AT1 or AT2 cells at P0. Due to the few cells labelled in their dual-lineage tracing model (which might be from a lack of labelling efficiency), these bipotent progenitors represented a minority of the total alveolar progenitors labelled at E15.5. Were these bipotent progenitors labelled at E13.5, perhaps the evidence would suggest a much larger contribution to the mature pools of alveolar cells. While the question of the relative importance of bipotent progenitors remains open, the data presented in this thesis does show

a significant minority of mature alveolar epithelial cells do arise from lineage-flexible progenitors. More work, therefore, needs to be conducted to accurately determine the relative ratios of progenitor types and their eventual fates during pseudoglandular stage development.

5.6.2 Role of FGFR2b signalling on alveolar epithelial lineage formation and maintenance

Little is known concerning the role of FGFR2b signalling on the development and maintenance of alveolar cells. Most of the research on this topic has looked at AT2 cells in the context of adult homeostasis and repair after injury. For example, using the bleomycin-induced lung fibrosis model, it was reported that mice with specific deletion of *Fgfr2* in SFTPC-positive AT2 cells were less able to repair after injury, showed increased mortality, and had fewer AT2 cells overall (Dorry et al., 2020). This study also showed that even in the absence of injury, *Fgfr2b* deletion resulted in enlarged airspaces and increased collagen deposition, as well as a decrease in the number of AT2 cells, suggesting that FGFR2 signalling is required for AT2 maintenance.

These results support earlier work which looked at the loss of *Etv5* in AT2 cells during homeostasis and repair after bleomycin-induced lung injury (Zhang et al., 2017). Here, it was shown that ETV5 is required to maintain AT2 cells, for in its absence, AT2 cells transdifferentiated to AT1s. Furthermore, loss of *Etv5* in AT2 cells drastically impaired the repair process of the epithelium after lung injury, resulting in fewer AT2 cells altogether. It is well established that ETV5 is regulated by FGFR2b signalling (Herriges et al., 2015; Jones et al., 2019b), and it was suggested that ETV5 protein stability in AT2 cells is controlled by Ras-mediated Erk signalling (Zhang et al., 2017).

Interestingly, we recently described that miR-142 is critical for the formation of the alveolar lineage and more particularly for the formation of AT1 cells (Shrestha et al., 2019). In the absence of *miR-142*, a proportion of alveolar progenitors differentiate towards the AT2 lineage in an Ep300-dependent manner while overexpression of *miR-142* in alveolar progenitors leads to their differentiation towards the AT1 lineage. Furthermore, early

evidence suggests a role for FGFR2b in this process, because when *miR-142* is knocked-out, FGFR2 is upregulated and increased Erk signalling is observed in experimental lungs. It remains unclear how exactly FGFR2b signalling and miR-142 are related. Of note, the proportion of alveolar epithelial progenitors which showed a response to *miR-142* knock-out was small, yet highly significant. This mirrors the findings of the current study, wherein only a fraction of progenitors seems to respond to FGFR2b signalling, underscoring the extensive heterogeneity of progenitor populations.

The differentiation of alveolar epithelial cells depends not only on ligand-receptor interactions, but also on mechanical forces. For example, it was demonstrated that AT1 cell differentiation is dependent on the mechanical stretching of AT1 progenitors from fetal breathing movements (Li et al., 2018). In the same study, it was shown that some progenitors avoid an AT1 fate due to an FGF10/FGFR2b mediated build-up of myosin in the apical region of a proportion of the cells. This increase in myosin is related to the protrusion of these progenitors from the monolayer epithelium, thereby sparing them from the mechanical forces experienced by the cells lining the lumen. These protruded cells adopt an AT2 fate.

There is limited research concerning the regulation of alveolar epithelial lineage formation by FGFR2b signalling during development. However, what is emerging supports the evidence seen during homeostasis and repair after injury, namely, that FGFR2b signalling maintains AT2 cell identity. It seems clear that even during early pseudoglandular development, FGFR2b signalling primarily affects AT2 lineage formation. As early as E12.5, for example, just after nine hours FGFR2b ligand inhibition or *Fgfr2* conditional inactivation, the AT2 signature found in distal tip progenitors was significantly decreased (Jones et al., 2019a; Yin and Ornitz, 2020). However, this is only part of the story. The data presented in the current thesis strongly suggests that FGFR2b signalling not only affects the AT2 lineage, but the AT1 lineage as well. The cell autonomous loss of *Fgfr2b* in labelled $SFTPC^{Pos}$ AT2 progenitors or in $HOPX^{Pos}$ AT1 progenitors leads to an *increase* in the ratio of labelled cells belonging to the alternate lineage (Fig. 23). These findings are independent of possible differential proliferative or apoptotic effects (Figs. S6 and S7), and therefore represent impacts on cellular differentiation. In summary, FGFR2b signalling, while acting primarily on the AT2 lineage at later stages of

development, does appear to maintain the lineage commitment of both AT2 and AT1 progenitors during late pseudoglandular and early saccular lung development.

5.6.3 Narrowing of FGFR2b signalling to an AT2 sub-population over embryonic development highlights the heterogeneity of AT2 cells

Assessing, at a fixed stage of development (e.g., E17.5), the expression patterns of the FGFR2b signatures from earlier embryonic stages revealed that the closer these signatures came to the fixed timepoint, the more narrowly confined their expression became. The earlier in embryonic development one looks, the less differentiated the FGFR2b-responding progenitors will be. Thus, at E12.5, for example, the distal tip epithelial progenitors are largely uncommitted multipotent cells; consequently, FGFR2b signalling at earlier stages affects the differentiation of an increasing number of cell lineages. However, as development progresses, distal progenitors become more lineage-restricted, not only as a consequence of ligand-receptor interactions and tissue geometry, but also in response to mechanical and physical forces (Jones et al., 2021).

Our data indicate that as alveolar cell lineages emerge and develop (beginning as early as E12.5), the role of FGFR2b signalling shifts, eventually concentrating in a sub-population of the AT2 lineage (Fig. 25). This highlights an increasingly appreciated fact that cellular populations are heterogeneous, and points to the need to identify and further classify these sub-populations of cells (Wang et al., 2018; Chen and Liu, 2020; Ahmadvand et al., 2021). Indeed, recent work from our lab has identified two major sub-populations of AT2 cells in adult mice: those expressing high levels of *Sftpc* and *Fgfr2b*, and those expressing low levels of both markers in addition to high expression of a cell surface protein called PD-L1 (Ahmadvand et al., 2021). It was shown that this latter immature sub-population of AT2s is quiescent during homeostasis, but is activated during compensatory growth after pneumonectomy, eventually expanding to replenish the mature AT2 population. These cells were termed 'injury activated alveolar progenitors' (IAAPs), and were also found to be enriched in precision cut lung slices of human fibrotic samples (Ahmadvand et al., 2022a), as well as in the context of *Fgfr2b* deletion in SFTPC^{Pos} cells during homeostasis in the mouse (Ahmadvand et al., 2022b). The engagement of this quiescent population in response to injury

likely depends on FGFR2b signalling. In line with this idea, the evidence presented in this thesis suggests that AT2 cells can be sub-classified according to responsiveness to FGFR2b signalling. Whether this responsiveness is a consequence of geographic proximity to zones of active FGFR2b ligand activity, or whether a subset of cells is no longer capable at a molecular level to respond to FGFR2b ligands, is yet to be determined. What is evident from the current data, however, is that a subset of AT2 cells, which is activated after injury to replenish the AT1 population, highly expresses E16.5 FGFR2b signature genes (Fig. 26). By mechanisms still unknown, as these activated AT2s transition to AT1s through a $KRT8^{Pos}$ airway differentiation intermediate state, the FGFR2b signature is effectively shut off.

One possible mechanism regulating FGFR2b signalling in injury-activated AT2 cells is inflammatory signalling present in the lung during injury. A recent paper has posited that a subset of AT2s expressing *interleukin 1 receptor type 1* (*Il1r1*) is primed to respond to acute inflammation to transition to AT1s during repair after injury (Choi et al., 2020). Whether these *Il1r1*-positive AT2s also express *Krt8* and shut off FGFR2b signalling remains to be determined. In our gene array data from the loss of FGFR2b signalling in AT2 progenitors, *Il1r1* expression is upregulated in the RFP-labelled AT1 pool at E18.5 (data not shown). This supports the argument that a subset of labelled AT2 cells transition to AT1 cells upon loss of FGFR2b signalling. However, the main message to consider here is that the varying responsiveness of alveolar cells demarcates subpopulations critical for repair after injury, and likely during development. This fact should be considered for more accurate alveolar cell type classification schemes.

In conclusion, we have presented evidence to support a model of alveolar lineage specification and differentiation which highlights the lineage-flexibility of alveolar progenitors. The decision of progenitors to commit to a particular lineage is in part regulated by FGFR2b signalling, which is also likely instructive for the transdifferentiation of progenitors in the adult lung during repair after injury. We also have made a case, given the extensive heterogeneity present in currently accepted broad classifications, for a more nuanced designation of alveolar epithelial cell types.

6 Conclusions

This thesis reports the research we conducted on the role of FGFR2b signalling during embryonic (E9.5-E10.5), early pseudoglandular (E10.5-E12.5), mid-pseudoglandular (E14.5), and late pseudoglandular (E16.5) stage lung development in mice. We addressed three main aims: 1) to characterize the biological impacts and transcriptional targets of FGFR2b signalling during these stages of development; 2) to assess the role played by FGFR2b signalling on alveolar lineage formation and differentiation; and 3) to identify populations of cells responding to FGFR2b signalling during development, homeostasis, and repair after injury. We made use of a dominant negative mouse model to conditionally inhibit FGFR2b ligand activity in a global manner (to address aim 1), as well as a model to delete *Fgfr2b* cell-autonomously from specific cell populations whilst labelling those cells (to address aim 2). Finally, we mined published scRNA-seq datasets to investigate the populations responding to the FGFR2b signatures we found at E12.5, E14.5, and at E16.5 (to address aim 3). The main findings are summarized in Figure 30.

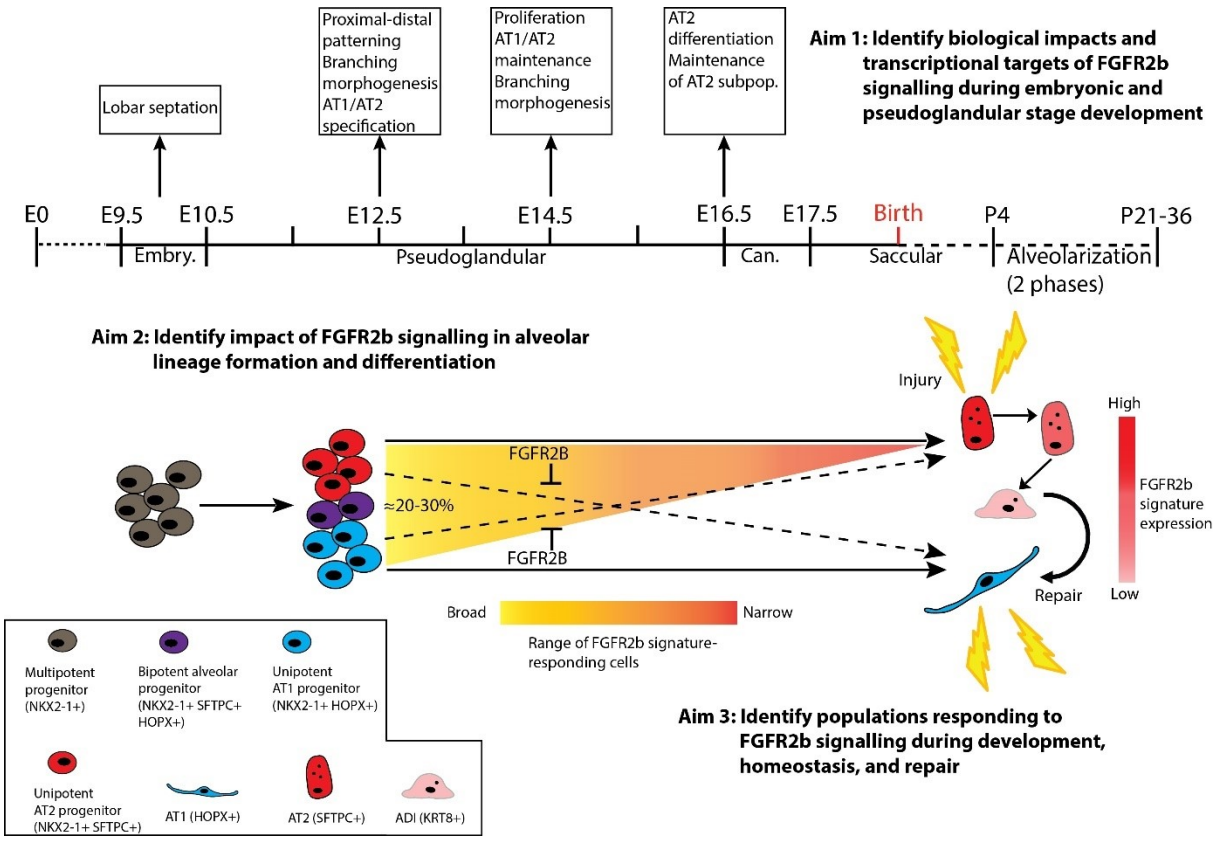

Figure 30 – Summary of the three aims of the thesis. Aim 1 – Using the dominant negative mouse model to inhibit FGFR2b signalling during the embryonic and pseudoglandular stages

of lung development, the indicated biological impacts of FGFR2b signalling were discovered, as well as an FGFR2b signature at E12.5, E14.5, and at E16.5. **Aim 2 –** Using cell autonomous mouse models to label AT1 and AT2 progenitors between E14.5 and E16.5 (E14.5 and E15.5 Dox-IP), we found that between 20% and 30% of progenitors are lineage-flexible. When *Fgfr2b* is knocked-out of these progenitors, an increase in cross-lineage commitment is observed, suggesting FGFR2b signalling restricts cross-lineage commitment. Furthermore, the results from our global inhibition model suggests that FGFR2b signalling impacts most of the distal multipotent epithelial cells at E12.5 and at E14.5, regulating both AT1 and AT2 lineage formation. **Aim 3 –** Using scRNA-seq datasets, we discovered that FGFR2b signalling narrows over development to a subpopulation of mature AT2s. Furthermore, in a model of lung injury in adult mice, evidence suggests that mature AT2 cells maintain relatively high levels of FGFR2b signalling during homeostasis but lose the signalling during the transition through a $KRT8^{pos}$ alveolar differentiation intermediate to replace damaged AT1 cells.

Two major themes emerged in this work. First, the biological roles of FGFR2b signalling on distal tip epithelial progenitors during early lung development reveal a shifting spectrum of emphasis within a short timeframe, from lobar genesis and septation, to branching morphogenesis, to cellular proliferation and the maintenance of alveolar progenitors. Our research has potentially provided valuable foundational datasets for further analyses of each of these stages, which will not only provide better knowledge of mouse lung development, but critically inform translational research. Second, our investigation into the cell populations responding to FGFR2b during development, homeostasis, and repair after injury illustrate an increasingly appreciated fact: cell populations are heterogenous. This fact is often lost in currently broad classification schemes. This not only potentially clouds one's interpretation of results, but also the clear and effective formulation of new hypotheses and experimental designs.

In the end, the general themes of this thesis are unsurprising. Biological organs, such as the mammalian lung, are complex systems; neat categorizations are imposed by human researchers and are only helpful insofar as they allow us to conceptualize, hypothesize, and interpret data. Sometimes, however, categories hide critical facts and prevent valuable insights. Since a main goal of scientific research is not only the pursuit, but also the application, of knowledge to help solve the world's problems, the conceptual categories we employ must fit, as far as possible, the questions we ask.

7 Summary

Murine lung development depends on an intricate interplay of molecular, cellular, and physical factors. An active area of research is on molecular signalling between the mesenchyme and adjacent airway epithelium. One such pathway involves fibroblast growth factors (FGFs), secreted in the distal mesenchyme, binding to fibroblast growth factor receptor 2b (FGFR2b) on adjacent epithelium. The primary FGF during early lung development is FGF10. In mouse models where either *Fgf10* or *Fgfr2b* was constitutively knocked-out, complete lung agenesis was observed. However, nearly 25 years from these original observations, little is known concerning the direct transcriptional and biological targets of FGFR2b signalling during lung development.

Our research has begun to address this lack of knowledge. Using conditional *in vivo* mouse models to globally inhibit FGFR2b ligands or inactivate *Fgfr2b* gene expression in target cells, we addressed the broad roles played by FGFR2b signalling throughout embryonic (embryonic day I 9.5-E10.5), early pseudoglandular (E10.5-E12.5), mid-pseudoglandular (E14.5), and late pseudoglandular stage (E16.5) lung development in mice. We had three main aims: 1) to characterize the biological impacts and identify transcriptional signatures of FGFR2b signalling during these stages of development; 2) to assess the role played by FGFR2b signalling on alveolar lineage formation and differentiation; and 3) to use the gene signatures obtained from 'aim 1' to identify, *in silico*, populations of cells responding to FGFR2b signalling during development, homeostasis, and repair after injury.

Results indicate that FGFR2b signalling regulates lobar septation and accessory lobe formation during embryonic stage lung development; branching morphogenesis and cellular proliferation during early- and mid-pseudoglandular stage development; and alveolar lineage specification and differentiation from the late pseudoglandular stage. Interestingly, data suggest that during early alveolar lineage formation, where alveolar type 1 and 2 (AT1 and AT2) progenitors are specified, FGFR2b signalling prevents progenitors from committing to the opposing lineage. Finally, *in silico* data mining revealed that the gene signatures from E12.5, E14.5, and E16.5., converged on a subpopulation of AT2 cells during late lung

development and homeostasis. Upon repair after injury, these signatures were effectively lost in AT2 cells transitioning to AT1 cells; this supports the finding that FGFR2b is required to prevent alveolar cross-lineage transdifferentiation.

The results reported in this thesis offer a broad foundation for future work on the role of FGFR2b signalling during lung development. We have provided sets of target genes at multiple embryonic timepoints, which can form the basis for more exhaustive investigation. Furthermore, we have presented compelling evidence for a novel interpretation of FGFR2b signalling on the lineage-commitment of alveolar progenitor cells. Specifically, that FGFR2b signalling prevents alveolar progenitors from committing to the opposing lineage. Finally, our *in silico* results support an increasingly appreciated fact in the field of lung development, namely, that populations of cells are extremely heterogenous. Accurately classifying a population of interest is critical for effective hypothesis formulation, experimental design, and interpretation of results.

8 Zusammenfassung

Die Entwicklung der Lunge von Mäusen hängt von einem komplizierten Zusammenspiel molekularer, zellulärer und physikalischer Faktoren ab. Ein aktives Forschungsgebiet ist die molekulare Signalübertragung zwischen dem Mesenchym und dem angrenzenden Atemwegsepithel. Ein solcher Signalweg beinhaltet Fibroblasten-Wachstumsfaktoren (FGFs), die im distalen Mesenchym sezerniert werden und an den Fibroblasten-Wachstumsfaktor-Rezeptor 2b (FGFR2b) auf dem angrenzenden Epithel binden. Der wichtigste FGF während der frühen Lungenentwicklung ist FGF10. In Mausmodellen, bei denen entweder Fgf10 oder Fgfr2b konstitutiv ausgeschaltet wurde, wurde eine vollständige Lungenagenese beobachtet. Fast 25 Jahre nach diesen ursprünglichen Beobachtungen ist jedoch wenig über die direkten transkriptionellen und biologischen Ziele der FGFR2b-Signalübertragung während der Lungenentwicklung bekannt.

Unsere Forschung hat damit begonnen, diesen Wissensmangel zu beheben. Mit Hilfe von konditionalen in vivo Mausmodellen zur globalen Hemmung von FGFR2b-Liganden oder zur Inaktivierung der Fgfr2b-Genexpression in den Zielzellen untersuchten wir die umfassende Rolle, die der FGFR2b-Signalweg während der embryonalen (Embryonaltag (E) 9,5-E10,5), frühen pseudoglandulären (E10,5-E12,5), mittleren (E14,5) und späten (E16,5) Lungenentwicklung bei Mäusen spielt. Wir verfolgten drei Hauptziele: 1) Charakterisierung der biologischen Auswirkungen und Identifizierung von Transkriptionssignaturen der FGFR2b-Signalgebung während dieser Entwicklungsstadien; 2) Bewertung der Rolle, die die FGFR2b-Signalgebung bei der Bildung und Differenzierung der alveolären Abstammungslinie spielt; und 3) Verwendung der Gensignaturen aus Ziel 1“ zur In-silico-Identifizierung von Zellpopulationen, die auf die FGFR2b-Signalgebung während der Entwicklung, Homöostase und Reparatur nach Verletzungen reagieren.

Die Ergebnisse zeigen, dass der FGFR2b-Signalweg die Lappenseptation und die Bildung von Nebenlappen während der embryonalen Lungenentwicklung, die Verzweigungsmorphogenese und die Zellproliferation während der frühen und mittleren pseudoglandulären Entwicklung sowie die alveoläre Abstammung und Differenzierung ab dem

späten pseudoglandulären Stadium reguliert. Interessanterweise deuten die Daten darauf hin, dass die FGFR2b-Signalisierung während der frühen Alveolarstammbildung, bei der Vorläufer des Alveolartyps 1 und 2 (AT1 und AT2) spezifiziert werden, verhindert, dass sich die Vorläufer für die entgegengesetzte Linie entscheiden. Schließlich ergab das In-silico-Data-Mining, dass die Gensignaturen von E12,5, E14,5 und E16,5 während der späten Lungenentwicklung und Homöostase auf eine Subpopulation von AT2-Zellen konvergieren. Bei der Reparatur nach einer Verletzung gingen diese Signaturen in AT2-Zellen, die sich in AT1-Zellen umwandeln, effektiv verloren; dies unterstützt die Feststellung, dass FGFR2b erforderlich ist, um eine alveoläre Transdifferenzierung zwischen den Linien zu verhindern.

Die in dieser Arbeit berichteten Ergebnisse bieten eine breite Grundlage für zukünftige Arbeiten zur Rolle der FGFR2b-Signalübertragung während der Lungenentwicklung. Wir haben eine Reihe von Zielgenen zu verschiedenen embryonalen Zeitpunkten identifiziert, die die Grundlage für umfassendere Untersuchungen bilden können. Darüber hinaus haben wir überzeugende Beweise für eine neuartige Interpretation der FGFR2b-Signalgebung bei der Festlegung der Zelllinien von alveolären Vorläuferzellen vorgelegt. Genauer gesagt, dass FGFR2b-Signale die alveolären Vorläuferzellen daran hindern, sich für die gegnerische Linie zu entscheiden. Schließlich unterstützen unsere In-silico-Ergebnisse eine zunehmend anerkannte Tatsache auf dem Gebiet der Lungenentwicklung, nämlich dass Zellpopulationen extrem heterogen sind. Die genaue Klassifizierung einer Population von Interesse ist entscheidend für die Formulierung von Hypothesen, die Versuchsplanung und die Interpretation der Ergebnisse.

9 Bibliography

Abler, L. L., Mansour, S. L., and Sun, X. (2008). Conditional gene inactivation reveals roles for Fgf10 and Fgfr2 in establishing a normal pattern of epithelial branching in the mouse lung. *Dev. Dyn.* 238, 1999–2013. doi:10.1002/dvdy.22032.

Ahmadvand, N., Carraro, G., Jones, M. R., Shalashova, I., Noori, A., Wilhelm, J., et al. (2022a). Cell-Surface Programmed Death Ligand-1 Expression Identifies a Sub-Population of Distal Epithelial Cells Enriched in Idiopathic Pulmonary Fibrosis. *Cells* 11, 1593. doi:10.3390/cells11101593.

Ahmadvand, N., Khosravi, F., Lingampally, A., Wasnick, R., Vazquez-Armendariz, I., Carraro, G., et al. (2021). Identification of a novel subset of alveolar type 2 cells enriched in PD-L1 and expanded following pneumonectomy. *Eur. Respir. J.* 58, 2004168. doi:10.1183/13993003.04168-2020.

Ahmadvand, N., Lingampally, A., Khosravi, F., Vazquez-Armendariz, A. I., Rivetti, S., Jones, M. R., et al. (2022b). Fgfr2b signaling is essential for the maintenance of the alveolar epithelial type 2 lineage during lung homeostasis in mice. *Cell. Mol. Life Sci.* 79, 2022.01.26.477823. doi:10.1007/s00018-022-04327-w.

Al Alam, D., El Agha, E., Sakurai, R., Kheirollahi, V., Moiseenko, A., Danopoulos, S., et al. (2015). Evidence for the involvement of fibroblast growth factor 10 in lipofibroblast formation during embryonic lung development. *Dev.* 142, 4139–4150. doi:10.1242/dev.109173.

Andy Bunn, M. K. (2017). A language and environment for statistical computing. *R Found. Stat. Comput.* 10, 11–18. Available at: http://www.gnu.org/copyleft/gpl.html.%0Ahttp://www.r-project.org/%0Ahttp://www.r-project.org.

Armelin, H. A. (1973). Pituitary extracts and steroid hormones in the control of 3T3 cell growth (mouse fibroblasts/growth factor). *Proc. Natl. Acad. Sci. U. S. A.* 70, 2702–2706. doi:10.1073/pnas.70.9.2702.

Bellusci, S., Grindley, J., Emoto, H., Itoh, N., and Hogan, B. L. M. (1997). Fibroblast Growth Factor 10 (FGF10) and branching morphogenesis in the embryonic mouse lung. *Development* 124, 4867–4878. doi:10.1242/dev.124.23.4867.

Bird, A. D., Flecknoe, S. J., Tan, K. H., Olsson, P. F., Antony, N., Mantamadiotis, T., et al. (2011). cAMP response element binding protein is required for differentiation of respiratory epithelium during murine development. *PLoS One* 6, 17843. doi:10.1371/journal.pone.0017843.

Blanc, P., Coste, K., Pouchin, P., Azaïs, J. M., Blanchon, L., Gallot, D., et al. (2012). A role for mesenchyme dynamics in mouse lung branching morphogenesis. *PLoS One* 7. doi:10.1371/journal.pone.0041643.

Bokka, K. K., Jesudason, E. C., Lozoya, O. A., Guilak, F., Warburton, D., and Lubkin, S. R. (2015a). Morphogenetic implications of peristalsis-driven fluid flow in the embryonic lung. *PLoS One* 10. doi:10.1371/journal.pone.0132015.

Bokka, K. K., Jesudason, E. C., Warburton, D., and Lubkin, S. R. (2015b). Morphogenetic implications of peristaltic fluid-tissue dynamics in the embryonic lung. *J. Theor. Biol.* 382, 378–385. doi:10.1016/j.jtbi.2015.06.022.

Bokka, K. K., Jesudason, E. C., Warburton, D., and Lubkin, S. R. (2016). Quantifying cellular and subcellular stretches in embryonic lung epithelia under peristalsis: Where to look for mechanosensing. *Interface Focus* 6. doi:10.1098/rsfs.2016.0031.

Cardoso, W. V., Itoh, A., Nogawa, H., Mason, I., and Brody, J. S. (1997). FGF-1 and FGF-7 induce distinct patterns of growth and differentiation in embryonic lung epithelium. *Dev. Dyn.* 208, 398–405. doi:10.1002/(SICI)1097-0177(199703)208:3<398::AID-AJA10>3.0.CO;2-X.

Cardoso, W. V., and Lü, J. (2006). Regulation of early lung morphogenesis: Questions, facts and controversies. *Development* 133, 1611–1624. doi:10.1242/dev.02310.

Chang, D. R., Alanis, D. M., Miller, R. K., Ji, H., Akiyama, H., McCrea, P. D., et al. (2013). Lung epithelial branching program antagonizes alveolar differentiation. *Proc. Natl. Acad. Sci. U. S. A.* 110, 18042–18051. doi:10.1073/pnas.1311760110.

Chao, C. M., Yahya, F., Moiseenko, A., Tiozzo, C., Shrestha, A., Ahmadvand, N., et al. (2017). Fgf10 deficiency is causative for lethality in a mouse model of bronchopulmonary dysplasia. *J. Pathol.* 241, 91–103. doi:10.1002/path.4834.

Chen, Q., and Liu, Y. (2020). Heterogeneous groups of alveolar type II cells in lung homeostasis and repair. *Am. J. Physiol. - Cell Physiol.* 319, C991–C996. doi:10.1152/ajpcell.00341.2020.

Choi, J., Park, J. E., Tsagkogeorga, G., Yanagita, M., Koo, B. K., Han, N., et al. (2020). Inflammatory Signals Induce AT2 Cell-Derived Damage-Associated Transient Progenitors that Mediate Alveolar Regeneration. *Cell Stem Cell* 27, 366-382.e7. doi:10.1016/j.stem.2020.06.020.

Cilvik, S. N., Wang, J. I., Lavine, K. J., Uchida, K., Castro, A., Gierasch, C. M., et al. (2013). Fibroblast growth factor receptor 1 signaling in adult cardiomyocytes increases contractility and results in a hypertrophic cardiomyopathy. *PLoS One* 8, 82979. doi:10.1371/journal.pone.0082979.

Clément, R., Blanc, P., Mauroy, B., Sapin, V., and Douady, S. (2012). Shape self-regulation in early lung morphogenesis. *PLoS One* 7. doi:10.1371/journal.pone.0036925.

Danopoulos, S., Parsa, S., Al Alam, D., Tabatabai, R., Baptista, S., Tiozzo, C., et al. (2013). Transient Inhibition of FGFR2b-Ligands Signaling Leads to Irreversible Loss of Cellular β-Catenin Organization and Signaling in AER during Mouse Limb Development. *PLoS One* 8. doi:10.1371/journal.pone.0076248.

Danopoulos, S., Thornton, M. E., Grubbs, B. H., Frey, M. R., Warburton, D., Bellusci, S., et al. (2019). Discordant roles for FGF ligands in lung branching morphogenesis between human and mouse. *J. Pathol.* 247, 254–265. doi:10.1002/path.5188.

De Langhe, S. P., Carraro, G., Warburton, D., Hajihosseini, M. K., and Bellusci, S. (2006). Levels of mesenchymal FGFR2 signaling modulate smooth muscle progenitor cell commitment in the lung. *Dev. Biol.* 299, 52–62. doi:10.1016/j.ydbio.2006.07.001.

De Langhe, S. P., Sala, F. G., Del Moral, P. M., Fairbanks, T. J., Yamada, K. M., Warburton, D., et al. (2005). Dickkopf-1 (DKK1) reveals that fibronectin is a major target of Wnt signaling in branching morphogenesis of the mouse embryonic lung. *Dev. Biol.* 277, 316–331. doi:10.1016/j.ydbio.2004.09.023.

De Moerlooze, L., Spencer-Dene, B., Revest, J. M., Hajihosseini, M., Rosewell, I., and Dickson, C. (2000). An important role for the IIIb isoform of fibroblast growth factor receptor 2 (FGFR2) in mesenchymal-epithelial signalling during mouse organogenesis. *Development* 127, 483–492. doi:10.1242/dev.127.3.483.

Dilai, S. (2020). Characterization of the role of fibroblast growth factor 10 (Fgf10) and its receptor Fgfr2b on multipotent epithelial progenitor cells during early lung development. Available at: http://geb.uni-giessen.de/geb/volltexte/2020/15256.

Dorry, S. J., Ansbro, B. O., Ornitz, D. M., Mutlu, G. M., and Guzy, R. D. (2020). FGFR2 is required for AEC2 homeostasis and survival after bleomycin-induced lung injury. *Am. J. Respir. Cell Mol. Biol.* 62, 608–621. doi:10.1165/RCMB.2019-0079OC.

El Agha, E., Al Alam, D., Carraro, G., MacKenzie, B. A., Goth, K., de Langhe, S. P., et al. (2012). Characterization of a novel Fibroblast growth factor 10 (Fgf10) knock-in mouse line to target mesenchymal progenitors during embryonic development. *PLoS One* 7, 38452. doi:10.1371/journal.pone.0038452.

El Agha, E., and Bellusci, S. (2014). Walking along the Fibroblast Growth Factor 10 Route: A Key Pathway to Understand the Control and Regulation of Epithelial and Mesenchymal Cell-Lineage Formation during Lung Development and Repair after Injury. *Scientifica (Cairo).* 2014, 1–20. doi:10.1155/2014/538379.

Frank, D. B., Penkala, I. J., Zepp, J. A., Sivakumar, A., Linares-Saldana, R., Zacharias, W. J., et al. (2019). Early lineage specification defines alveolar epithelial ontogeny in the murine lung. *Proc. Natl. Acad. Sci. U. S. A.* 116, 4362–4371. doi:10.1073/pnas.1813952116.

Fumoto, K., Takigawa-Imamura, H., Sumiyama, K., Kaneiwa, T., and Kikuchi, A. (2017). Modulation of apical constriction by Wnt signaling is required for lung epithelial shape transition. *Dev.* 144, 151–162. doi:10.1242/dev.141325.

George, U. Z., Bokka, K. K., Warburton, D., and Lubkin, S. R. (2015). Quantifying stretch and secretion in the embryonic lung: Implications for morphogenesis. *Mech. Dev.* 138, 356–363. doi:10.1016/j.mod.2015.07.003.

Glenny, R. W. (2011). Emergence of matched airway and vascular trees from fractal rules. *J. Appl. Physiol.* 110, 1119–1129. doi:10.1152/japplphysiol.01293.2010.

Gospodarowicz, D. (1975). Purification of a fibroblast growth factor from bovine pituitary. *J. Biol. Chem.* 250, 2515–2520. doi:10.1016/s0021-9258(19)41631-1.

Gospodarowicz, D., Bialecki, H., and Greenburg, G. (1978). Purification of the fibroblast growth factor activity from bovine brain. *J. Biol. Chem.* 253, 3736–3743. doi:10.1016/s0021-9258(17)34863-9.

Habermehl, D., Parkitna, J. R., Kaden, S., Brügger, B., Wieland, F., Gröne, H. J., et al. (2011). Glucocorticoid activity during lung maturation is essential in mesenchymal and less in alveolar epithelial cells. *Mol. Endocrinol.* 25, 1280–1288. doi:10.1210/me.2009-0380.

Herriges, J. C., Verheyden, J. M., Zhang, Z., Sui, P., Zhang, Y., Anderson, M. J., et al. (2015). FGF-Regulated ETV Transcription Factors Control FGF-SHH Feedback Loop in Lung Branching. *Dev. Cell* 35, 322–332. doi:10.1016/j.devcel.2015.10.006.

Herriges, J. C., Yi, L., Hines, E. A., Harvey, J. F., Xu, G., Gray, P. A., et al. (2012). Genome-scale study of transcription factor expression in the branching mouse lung. *Dev. Dyn.* 241, 1432–1453. doi:10.1002/dvdy.23823.

Hokuto, I., Perl, A. K. T., and Whitsett, J. A. (2003). Prenatal, but not postnatal, inhibition of fibroblast growth factor receptor signaling causes emphysema. *J. Biol. Chem.* 278, 415–421. doi:10.1074/jbc.M208328200.

Iber, D., and Menshykau, D. (2013). The control of branching morphogenesis. *Open Biol.* 3. doi:10.1098/rsob.130088.

Jin, L., Wu, J., Bellusci, S., and Zhang, J. S. (2019). Fibroblast growth factor 10 and vertebrate limb development. *Front. Genet.* 10. doi:10.3389/fgene.2018.00705.

Jones, M., and Bellusci, S. (2019). "Imaging and analysis of mouse embryonic whole lung, isolated tissue, and lineage-labelled cell culture," in *Methods in Molecular Biology*, 109–127. doi:10.1007/978-1-4939-9086-3_8.

Jones, M. R., Chong, L., and Bellusci, S. (2021). Fgf10/Fgfr2b Signaling Orchestrates the Symphony of Molecular, Cellular, and Physical Processes Required for Harmonious Airway Branching Morphogenesis. *Front. Cell Dev. Biol.* 8, 620667. doi:10.3389/fcell.2020.620667.

Jones, M. R., Dilai, S., Lingampally, A., Chao, C. M., Danopoulos, S., Carraro, G., et al. (2019a). A comprehensive analysis of fibroblast growth factor receptor 2b signaling on epithelial tip progenitor cells during early mouse lung branching morphogenesis. *Front. Genet.* 10. doi:10.3389/fgene.2018.00746.

Jones, M. R., Lingampally, A., Ahmadvand, N., Chong, L., Wu, J., Wilhem, J., et al. (2022). FGFR2b signalling restricts lineage-flexible alveolar progenitors during mouse lung development and converges in mature alveolar type 2 cells. *Cell. Mol. Life Sci.* 79, 609. doi:10.1007/s00018-022-04626-2.

Jones, M. R., Lingampally, A., Dilai, S., Shrestha, A., Stripp, B., Helmbacher, F., et al. (2019b). Characterization of Tg(Etv4-GFP)and Etv5RFP reporter lines in the context of fibroblast growth factor 10 signaling during mouse embryonic lung development. *Front. Genet.* 10. doi:10.3389/fgene.2019.00178.

Jones, M. R., Lingampally, A., Wu, J., Sedighi, J., Ahmadvand, N., Wilhelm, J., et al. (2020). Evidence for Overlapping and Distinct Biological Activities and Transcriptional Targets Triggered by Fibroblast Growth Factor Receptor 2b Signaling between Mid- and Early Pseudoglandular Stages of Mouse Lung Development. *Cells* 9. doi:10.3390/cells9051274.

Jones, M., Zhang, J.-S., and Bellusci, S. (2019c). Bronchioalveolar stem cells vindicated! *Biotarget* 3, 4–4. doi:10.21037/biotarget.2019.04.01.

Kalinina, J., Dutta, K., Ilghari, D., Beenken, A., Goetz, R., Eliseenkova, A. V., et al. (2012). The alternatively spliced acid box region plays a key role in FGF receptor autoinhibition.

Structure 20, 77–88. doi:10.1016/j.str.2011.10.022.

Kim, H. Y., Pang, M. F., Varner, V. D., Kojima, L., Miller, E., Radisky, D. C., et al. (2015). Localized Smooth Muscle Differentiation Is Essential for Epithelial Bifurcation during Branching Morphogenesis of the Mammalian Lung. *Dev. Cell* 34, 719–726. doi:10.1016/j.devcel.2015.08.012.

Kim, H. Y., Varner, V. D., and Nelson, C. M. (2013). Apical constriction initiates new bud formation during monopodial branching of the embryonic chicken lung. *Dev.* 140, 3146–3155. doi:10.1242/dev.093682.

Lang, C., Conrad, L., and Iber, D. (2021). Organ-Specific Branching Morphogenesis. *Front. Cell Dev. Biol.* 9, 1–17. doi:10.3389/fcell.2021.671402.

Lang, C., Conrad, L., and Michos, O. (2018). Mathematical Approaches of Branching Morphogenesis. *Front. Genet.* 9. doi:10.3389/fgene.2018.00673.

Lebeche, D., Malpel, S., and Cardoso, W. V. (1999). Fibroblast growth factor interactions in the developing lung. *Mech. Dev.* 86, 125–136. doi:10.1016/S0925-4773(99)00124-0.

Li, J., Wang, Z., Chu, Q., Jiang, K., Li, J., and Tang, N. (2018). The Strength of Mechanical Forces Determines the Differentiation of Alveolar Epithelial Cells. *Dev. Cell* 44, 297-312.e5. doi:10.1016/j.devcel.2018.01.008.

Liem, K. F. (1988). Form and function of lungs: The evolution of air breathing mechanisms. *Integr. Comp. Biol.* 28, 739–759. doi:10.1093/icb/28.2.739.

Lü, J., Izvolsky, K. I., Qian, J., and Cardoso, W. V. (2005). Identification of FGF10 targets in the embryonic lung epithelium during bud morphogenesis. *J. Biol. Chem.* 280, 4834–4841. doi:10.1074/jbc.M410714200.

Mailleux, A. A., Kelly, R., Veltmaat, J. M., De Langhe, S. P., Zaffran, S., Thiery, J. P., et al. (2005). Fgf10 expression identifies parabronchial smooth muscle cell progenitors and is required for their entry into the smooth muscle cell lineage. *Development* 132, 2157–2166. doi:10.1242/dev.01795.

Makarenkova, H. P., Hoffman, M. P., Beenken, A., Eliseenkova, A. V., Meech, R., Tsau, C., et al. (2009). Differential interactions of FGFs with heparan sulfate control gradient formation and branching morphogenesis. *Sci. Signal.* 2, 1–21. doi:10.1126/scisignal.2000304.

Manwani, N., Gagnon, S., Post, M., Joza, S., Muglia, L., Cornejo, S., et al. (2010). Reduced viability of mice with lung epithelial-specific knockout of glucocorticoid receptor. *Am. J. Respir. Cell Mol. Biol.* 43, 599–606. doi:10.1165/rcmb.2009-0263OC.

Martis, P. C., Whitsett, J. A., Xu, Y., Perl, A. K. T., Wan, H., and Ikegami, M. (2006). C/EBPα is required for lung maturation at birth. *Development* 133, 1155–1164. doi:10.1242/dev.02273.

Metzger, D. E., Stahlman, M. T., and Shannon, J. M. (2008a). Misexpression of ELF5 disrupts lung branching and inhibits epithelial differentiation. *Dev. Biol.* 320, 149–160. doi:10.1016/j.ydbio.2008.04.038.

Metzger, D. E., Xu, Y., and Shannon, J. M. (2007). Elf5 is an epithelium-specific, fibroblast

growth factor-sensitive transcription factor in the embryonic lung. *Dev. Dyn.* 236, 1175–1192. doi:10.1002/dvdy.21133.

Metzger, R. J., Klein, O. D., Martin, G. R., and Krasnow, M. A. (2008b). The branching programme of mouse lung development. *Nature* 453, 745–750. doi:10.1038/nature07005.

Morrisey, E. E., and Hogan, B. L. M. (2010). Preparing for the First Breath: Genetic and Cellular Mechanisms in Lung Development. *Dev. Cell* 18, 8–23. doi:10.1016/j.devcel.2009.12.010.

Nelson, C. M., Gleghorn, J. P., Pang, M. F., Jaslove, J. M., Goodwin, K., Varner, V. D., et al. (2017). Microfluidic chest cavities reveal that transmural pressure controls the rate of lung development. *Dev.* 144, 4328–4335. doi:10.1242/dev.154823.

Ochoa-Espinosa, A., and Affolter, M. (2012). Branching morphogenesis: From cells to organs and back. *Cold Spring Harb. Perspect. Biol.* 4. doi:10.1101/cshperspect.a008243.

Ohtsuka, N., Urase, K., Momoi, T., and Nogawa, H. (2001). Induction of bud formation of embryonic mouse tracheal epithelium by fibroblast growth factor plus transferrin in mesenchyme-free culture. *Dev. Dyn.* 222, 263–272. doi:10.1002/dvdy.1206.

Ornitz, D. M., and Itoh, N. (2001). Protein family review: Fibroblast growth factors. *Genome Biol.* 2, reviews3005.1-3005.12. Available at: http://genomebiology.com/2001/2/3/reviews/3005.

Ornitz, D. M., and Itoh, N. (2015). The fibroblast growth factor signaling pathway. *Wiley Interdiscip. Rev. Dev. Biol.* 4, 215–266. doi:10.1002/wdev.176.

Ornitz, D. M., and Itoh, N. (2022). New developments in the biology of fibroblast growth factors. *WIREs Mech. Dis.* 14. doi:10.1002/wsbm.1549.

Ostrin, E. J., Little, D. R., Gerner-Mauro, K. N., Sumner, E. A., Ríos-Corzo, R., Ambrosio, E., et al. (2018). B-Catenin Maintains Lung Epithelial Progenitors After Lung Specification. *Dev.* 145. doi:10.1242/dev.160788.

Park, W. Y., Miranda, B., Lebeche, D., Hashimoto, G., and Cardoso, W. V. (1998). FGF-10 is a chemotactic factor for distal epithelial buds during lung development. *Dev. Biol.* 201, 125–134. doi:10.1006/dbio.1998.8994.

Patel, V. N., Pineda, D. L., and Hoffman, M. P. (2017). The function of heparan sulfate during branching morphogenesis. *Matrix Biol.* 57–58, 311–323. doi:10.1016/j.matbio.2016.09.004.

Perl, A. K. T., Kist, R., Shan, Z., Scherer, G., and Whitsett, J. A. (2005). Normal lung development and function after Sox9 inactivation in the respiratory epithelium. *Genesis* 41, 23–32. doi:10.1002/gene.20093.

Quaggin, S. E., Schwartz, L., Cui, S., Igarashi, P., Deimling, J., Post, M., et al. (1999). The basic-helix-loop-helix protein Pod1 is critically important for kidney and lung organogenesis. *Development* 126, 5771–5783. doi:10.1242/dev.126.24.5771.

Ramasamy, S. K., Mailleux, A. A., Gupte, V. V., Mata, F., Sala, F. G., Veltmaat, J. M., et al. (2007). Fgf10 dosage is critical for the amplification of epithelial cell progenitors and for

the formation of multiple mesenchymal lineages during lung development. *Dev. Biol.* 307, 237–247. doi:10.1016/j.ydbio.2007.04.033.

Ritchie, M. E., Phipson, B., Wu, D., Hu, Y., Law, C. W., Shi, W., et al. (2015). Limma powers differential expression analyses for RNA-sequencing and microarray studies. *Nucleic Acids Res.* 43, e47. doi:10.1093/nar/gkv007.

Rockich, B. E., Hrycaj, S. M., Shih, H. P., Nagy, M. S., Ferguson, M. A. H., Kopp, J. L., et al. (2013). Sox9 plays multiple roles in the lung epithelium during branching morphogenesis. *Proc. Natl. Acad. Sci. U. S. A.* 110, E4456–E4464. doi:10.1073/pnas.1311847110.

Schindelin, J., Arganda-Carreras, I., Frise, E., Kaynig, V., Longair, M., Pietzsch, T., et al. (2012). Fiji: An open-source platform for biological-image analysis. *Nat. Methods* 9, 676–682. doi:10.1038/nmeth.2019.

Schittny, J. C. (2017). Development of the lung. *Cell Tissue Res.* 367, 427–444. doi:10.1007/s00441-016-2545-0.

Schittny, J. C., Miserocchi, G., and Sparrow, M. P. (2000). Spontaneous peristaltic airway contractions propel lung liquid through the bronchial tree of intact and fetal lung explants. *Am. J. Respir. Cell Mol. Biol.* 23, 11–18. doi:10.1165/ajrcmb.23.1.3926.

Sekine, K., Ohuchi, H., Fujiwara, M., Yamasaki, M., Yoshizawa, T., Sato, T., et al. (1999). Fgf10 is essential for limb and lung formation. *Nat. Genet.* 21, 138–141. doi:10.1038/5096.

Shrestha, A., Carraro, G., Nottet, N., Vazquez-Armendariz, A. I., Herold, S., Cordero, J., et al. (2019). A critical role for miR-142 in alveolar epithelial lineage formation in mouse lung development. *Cell. Mol. Life Sci.* 76, 2817–2832. doi:10.1007/s00018-019-03067-8.

Shrestha, A., Mukhametshina, R. T., Taghizadeh, S., Vásquez-Pacheco, E., Cabrera-Fuentes, H., Rizvanov, A., et al. (2017). MicroRNA-142 is a multifaceted regulator in organogenesis, homeostasis, and disease. *Dev. Dyn.* 246, 285–290. doi:10.1002/dvdy.24477.

Spurlin, J. W., and Nelson, C. M. (2017). Building branched tissue structures: From single cell guidance to coordinated construction. *Philos. Trans. R. Soc. B Biol. Sci.* 372. doi:10.1098/rstb.2015.0527.

Strunz, M., Simon, L. M., Ansari, M., Kathiriya, J. J., Angelidis, I., Mayr, C. H., et al. (2020). Alveolar regeneration through a Krt8+ transitional stem cell state that persists in human lung fibrosis. *Nat. Commun.* 11. doi:10.1038/s41467-020-17358-3.

Swarr, D. T., and Morrisey, E. E. (2015). Lung Endoderm Morphogenesis: Gasping for Form and Function. *Annu. Rev. Cell Dev. Biol.* 31, 553–573. doi:10.1146/annurev-cellbio-100814-125249.

T. Das, A., Tenenbaum, L., and Berkhout, B. (2016). Tet-On Systems For Doxycycline-inducible Gene Expression. *Curr. Gene Ther.* 16, 156–167. doi:10.2174/1566523216666160524144041.

Taghizadeh, S., Jones, M. R., Olmer, R., Ulrich, S., Danopoulos, S., Shen, C., et al. (2020). Fgf10 Signaling-Based Evidence for the Existence of an Embryonic Stage Distinct From the Pseudoglandular Stage During Mouse Lung Development. *Front. Cell Dev. Biol.* 8.

doi:10.3389/fcell.2020.576604.

Tang, N., Marshall, W. F., McMahon, M., Metzger, R. J., and Martin, G. R. (2011). Control of mitotic spindle angle by the RAS-regulated ERK1/2 pathway determines lung tube shape. *Science (80-.).* 333, 342–345. doi:10.1126/science.1204831.

Tang, Z., Hu, Y., Wang, Z., Jiang, K., Zhan, C., Marshall, W. F., et al. (2018). Mechanical Forces Program the Orientation of Cell Division during Airway Tube Morphogenesis. *Dev. Cell* 44, 313-325.e5. doi:10.1016/j.devcel.2017.12.013.

Tao, Y. X. (2020). Molecular chaperones and G protein-coupled receptor maturation and pharmacology. *Mol. Cell. Endocrinol.* 511, 110862. doi:10.1016/j.mce.2020.110862.

Tirosh, I., Izar, B., Prakadan, S. M., Wadsworth, M. H., Treacy, D., Trombetta, J. J., et al. (2016). Dissecting the multicellular ecosystem of metastatic melanoma by single-cell RNA-seq. *Science (80-.).* 352, 189–196. doi:10.1126/science.aad0501.

Treutlein, B., Brownfield, D. G., Wu, A. R., Neff, N. F., Mantalas, G. L., Espinoza, F. H., et al. (2014). Reconstructing lineage hierarchies of the distal lung epithelium using single-cell RNA-seq. *Nature* 509, 371–375. doi:10.1038/nature13173.

Unbekandt, M., del Moral, P. M., Sala, F. G., Bellusci, S., Warburton, D., and Fleury, V. (2008). Tracheal occlusion increases the rate of epithelial branching of embryonic mouse lung via the FGF10-FGFR2b-Sprouty2 pathway. *Mech. Dev.* 125, 314–324. doi:10.1016/j.mod.2007.10.013.

Varma, S., Cao, Y., Tagne, J. B., Lakshminarayanan, M., Li, J., Friedman, T. B., et al. (2012). The transcription factors grainyhead-like 2 and NK2-homeobox 1 form a regulatory loop that coordinates lung epithelial cell morphogenesis and differentiation. *J. Biol. Chem.* 287, 37282–37295. doi:10.1074/jbc.M112.408401.

Varner, V. D., and Nelson, C. M. (2014). Cellular and physical mechanisms of branching morphogenesis. *Dev.* 141, 2750–2759. doi:10.1242/dev.104794.

Volckaert, T., Campbell, A., Dill, E., Li, C., Minoo, P., and De Langhe, S. (2013). Localized Fgf10 expression is not required for lung branching morphogenesis but prevents differentiation of epithelial progenitors. *Dev.* 140, 3731–3742. doi:10.1242/dev.096560.

Wang, Y., Tang, Z., Huang, H., Li, J., Wang, Z., Yu, Y., et al. (2018). Pulmonary alveolar type I cell population consists of two distinct subtypes that differ in cell fate. *Proc. Natl. Acad. Sci. U. S. A.* 115, 2407–2412. doi:10.1073/pnas.1719474115.

Warburton, D., Bellusci, S., De Langhe, S., Del Moral, P. M., Fleury, V., Mailleux, A., et al. (2005). Molecular Mechanisms of Early Lung Specification and Branching Morphogenesis. *Pediatr. Res.* 57, 26R-37R. doi:10.1203/01.PDR.0000159570.01327.ED.

Weaver, M., Batts, L., and Hogan, B. L. M. (2003). Tissue interactions pattern the mesenchyme of the embryonic mouse lung. *Dev. Biol.* 258, 169–184. doi:10.1016/S0012-1606(03)00117-9.

Weaver, M., Dunn, N. R., and Hogan, B. L. M. (2000). Bmp4 and Fgf10 play opposing roles during lung bud morphogenesis. *Development* 127, 2695–2704. doi:10.1242/dev.127.12.2695.

White, A. C., Xu, J., Yin, Y., Smith, C., Schmid, G., and Ornitz, D. M. (2006). FGF9 and SHH signaling coordinate lung growth and development through regulation of distinct mesenchymal domains. *Development* 133, 1507–1517. doi:10.1242/dev.02313.

Wolf, F. A., Angerer, P., and Theis, F. J. (2018). SCANPY: Large-scale single-cell gene expression data analysis. *Genome Biol.* 19, 15. doi:10.1186/s13059-017-1382-0.

Wong, C. H., Siah, K. W., and Lo, A. W. (2019). Estimation of clinical trial success rates and related parameters. *Biostatistics* 20, 273–286. doi:10.1093/biostatistics/kxx069.

Yang, J., and Chen, J. (2014). Developmental programs of lung epithelial progenitors: A balanced progenitor model. *Wiley Interdiscip. Rev. Dev. Biol.* 3, 331–347. doi:10.1002/wdev.141.

Yin, Y., and Ornitz, D. M. (2020). FGF9 and FGF10 activate distinct signaling pathways to direct lung epithelial specification and branching. *Sci. Signal.* 13. doi:10.1126/scisignal.aay4353.

Young, R. E., Jones, M. K., Hines, E. A., Li, R., Luo, Y., Shi, W., et al. (2020). Smooth Muscle Differentiation Is Essential for Airway Size, Tracheal Cartilage Segmentation, but Dispensable for Epithelial Branching. *Dev. Cell* 53, 73-85.e5. doi:10.1016/j.devcel.2020.02.001.

Zepp, J. A., and Morrisey, E. E. (2019). Cellular crosstalk in the development and regeneration of the respiratory system. *Nat. Rev. Mol. Cell Biol.* 20, 551–566. doi:10.1038/s41580-019-0141-3.

Zhang, Z., Newton, K., Kummerfeld, S. K., Webster, J., Kirkpatrick, D. S., Phu, L., et al. (2017). Transcription factor Etv5 is essential for the maintenance of alveolar type II cells. *Proc. Natl. Acad. Sci. U. S. A.* 114, 3903–3908. doi:10.1073/pnas.1621177114.

10 Supplementary figures

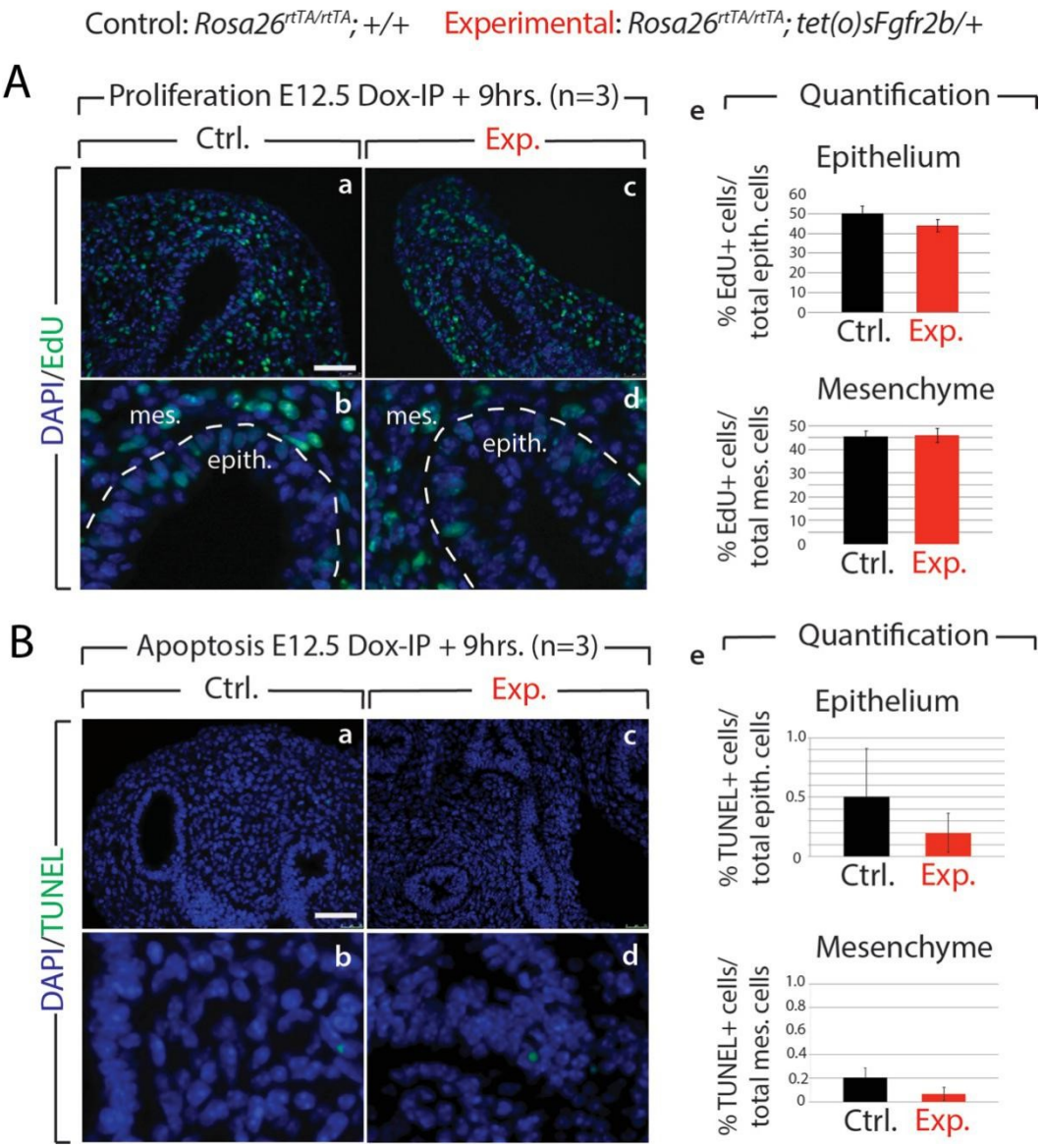

Figure S1 – Proliferation and apoptosis in control and experimental E12.5 lungs. (A) Proliferation analysis following EdU injection to pregnant females in control and experimental (Dox-IP +9 hrs.) E12.5 lungs. Quantification indicates no major difference in the number of proliferating cells in control vs. experimental lungs. (n=3) *Scale bar:* (a, c) 50µm; (b, d) 17 µm. **(B)** Apoptosis analysis by TUNEL showing no major difference in the number of apoptotic cells in control vs. experimental lungs. (n=3) *Scale bar:* (a, c) 50µm; (b, d) 17 µm.

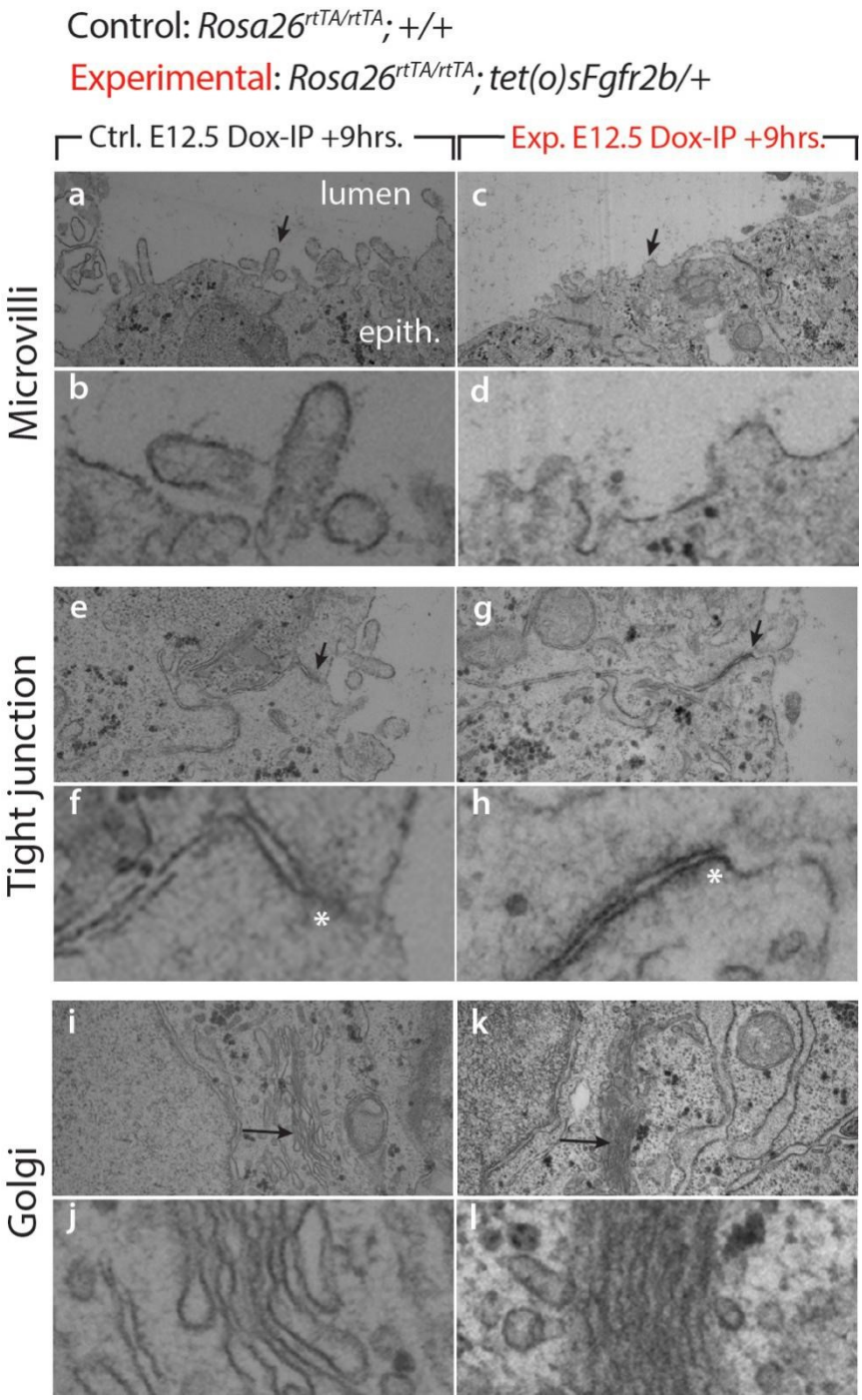

Figure S2 – Transmission electron microscopy of E12.5 distal lung buds. Compared to controls, experimental lungs (Dox-IP + 9hrs.) show reduced numbers and stunted microvilli (see black arrows, a-d), opened tight junctions (see black arrows in e and g; white asterisks in f and h), and flattened Golgi with increased staining (see black arrows, i-l). epith.=epithelium. *Magnification:* (a, c, e, g, i, k) 27800x; (b, d, f, h, j, l) 139000x.

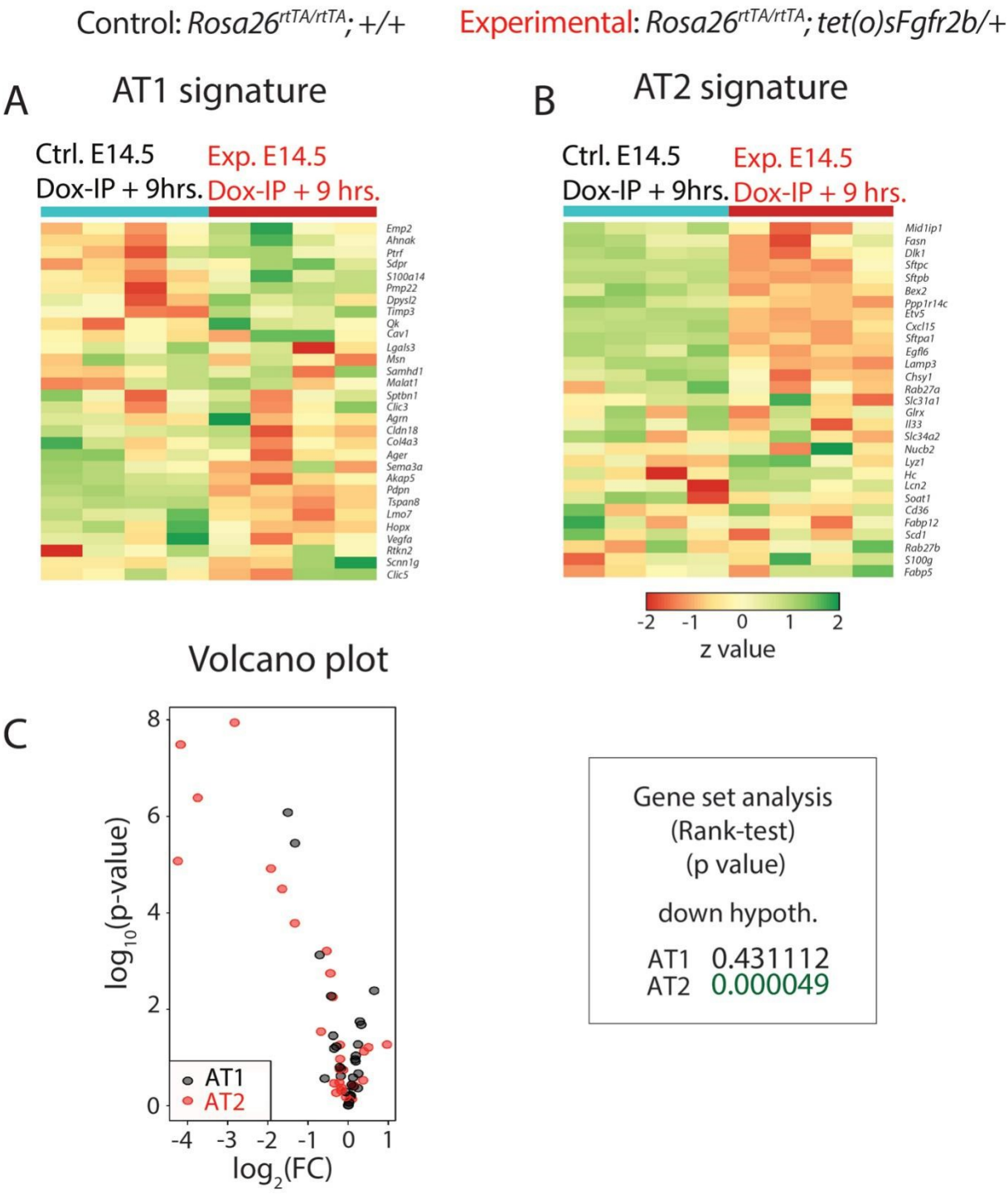

Figure S3 – Experimental lungs (E14.5 + 9 hrs.) display impaired AT2, but not AT1, differentiation. (A) Heatmap for the AT1 and **(B)** AT2 gene signature using the E14.5 + 9 hrs. experimental and control lungs. **(C)** Corresponding volcano plot and **(D)** gene set analysis showing a significant downregulation of the AT2 (p=0.000049), but not the AT1, signature.

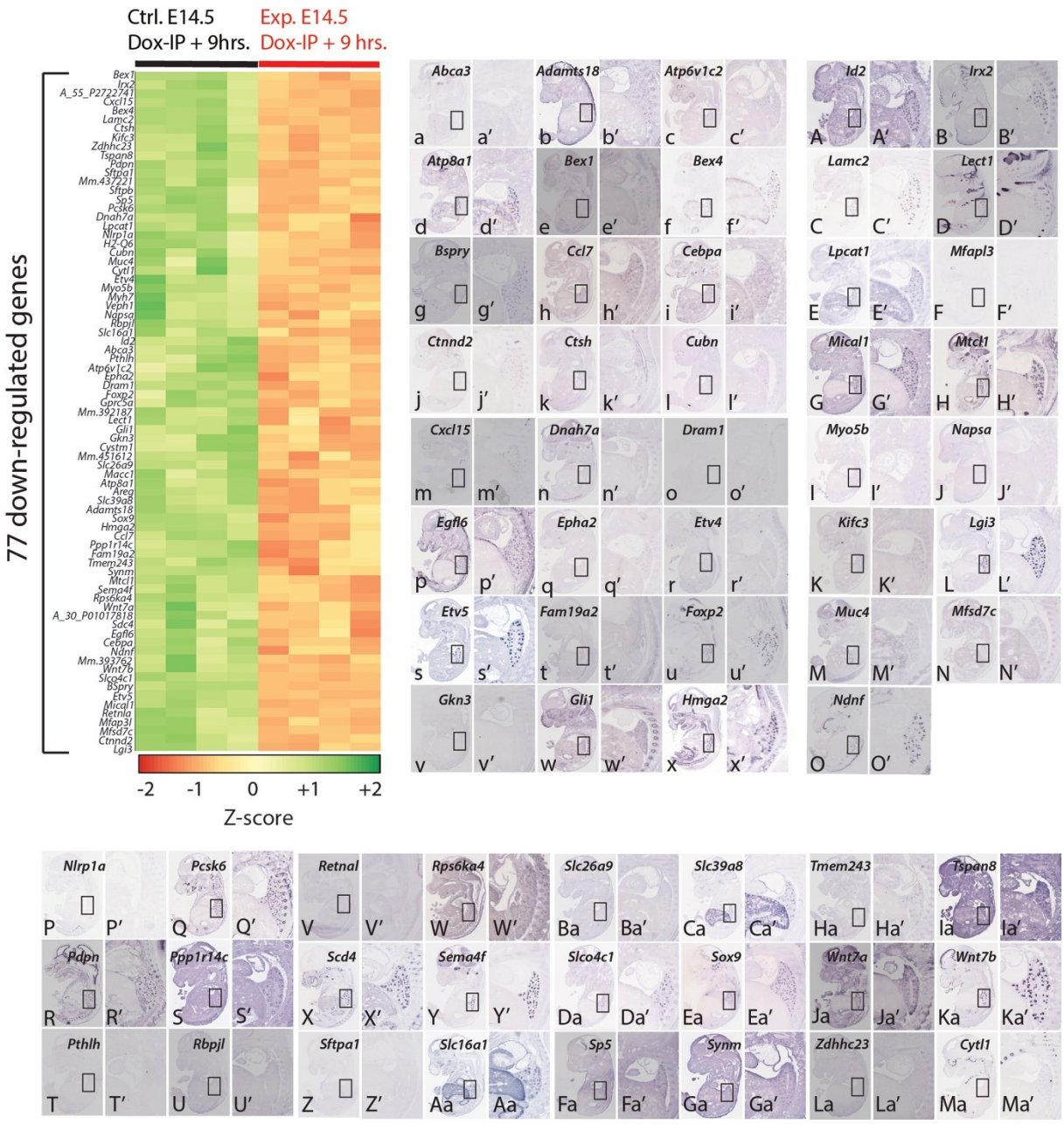

Figure S4 – The FGFR2b signature at E14.5. (A) Heatmap for the 77 genes downregulated from the top 100 regulated genes, constituting the FGFR2b signature at E14.5. **(B)** Corresponding *in situ* hybridization expression patterns for the identified genes (from 'Genepaint').

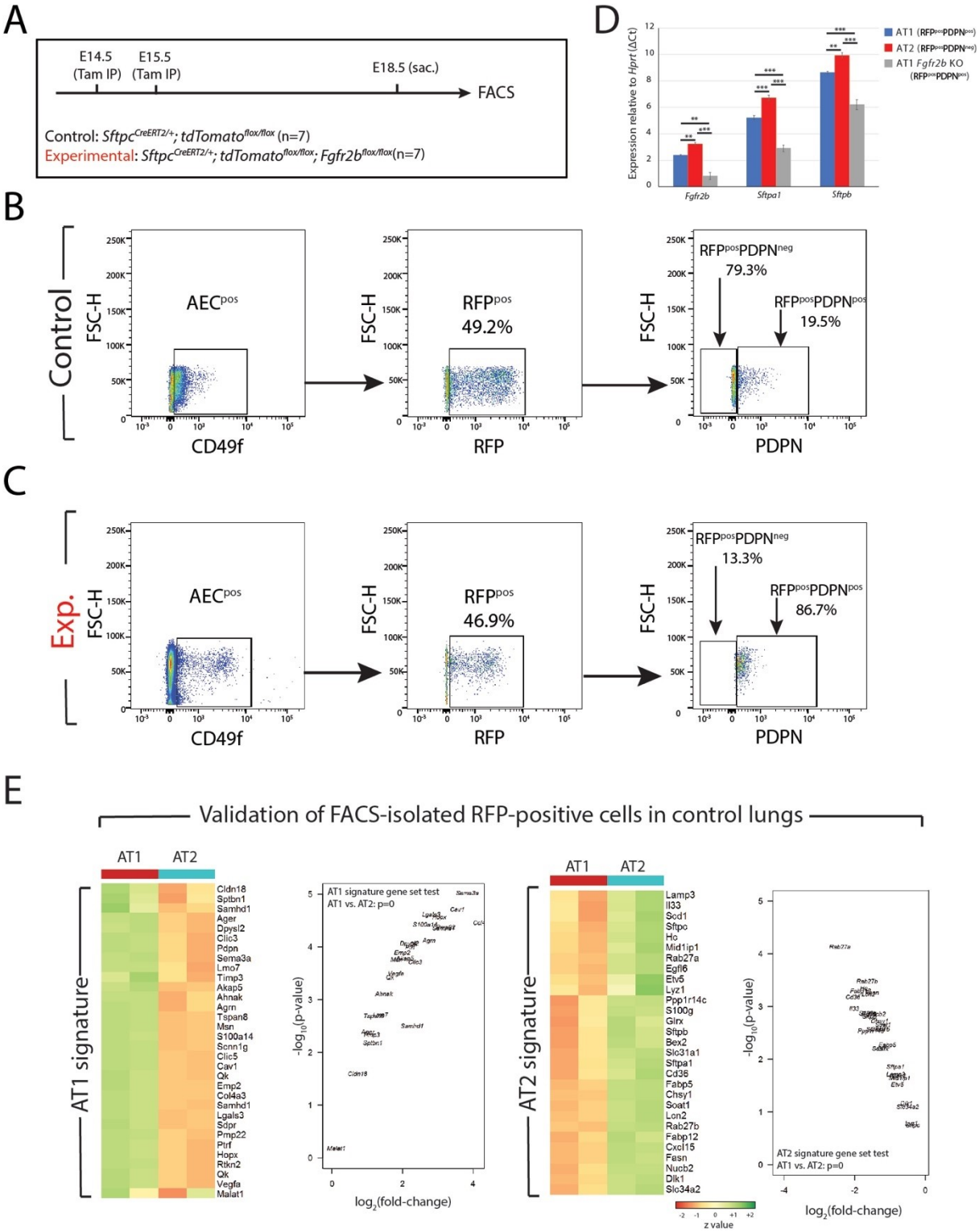

Figure S5 – FACS-isolated RFP-labelled AT1 and AT2 cells in *Sftpc*^{CreERT2} driver lines shows an increase in labelled AT1 cells in experimental (*Fgfr2b*$^{flox/flox}$) lungs. (A) Experimental design. Pregnant females carrying control and littermate experimental embryos were Tam-IP injected at E14.5 and at E15.5. Lungs were harvested at E18.5 and prepared for FACS. **(B and C)** FACS gating strategy to isolate RFP-labelled AT1 and AT2 cells. First, EpCAM^{pos} CD49f^{pos} cells were captured. These correspond to the alveolar epithelial cell (AEC) population. Then RFP^{pos} cells were isolated from RFP^{neg} cells, and finally, PDPN^{pos} cells, corresponding to the AT1^{pos} pool,

were isolated from the PDPN^{neg} population representing the AT2^{pos} pool. **(D)** qPCR data showing the expressions of *Fgfr2b*, *Sftpa1*, and *Sftpb* relative to *Hprt* in FACS-isolated control AT1 and AT2 cells (blue and red bars, respectively) and in isolated experimental AT1 cells (grey bars). The significant reduction of *Fgfr2b* expression in experimental RFP-labelled AT1 cells confirms that our model to knock-out *Fgfr2b* expression works. Note also that *Fgfr2b* mRNA is expressed in both control AT1 and AT2 cells. (n=4; *Fgfr2b* ΔCt in control AT1 is 2.37 ± 0.05, in control AT2 is 3.24 ± 0.10, and in experimental AT1 is 0.81 ± 0.26; *Sftpa1* ΔCt in control AT1 is 5.21 ± 0.16, in control AT2 is 6.72 ± 0.21, and in experimental AT1 is 2.91 ± 0.25; *Sftpb* ΔCt in control AT1 is 8.64 ± 0.07, in control AT2 is 9.94 ± 0.18, and in experimental AT1 is 6.21 ± 0.37. **p-value < 0.01, ***p-value < 0.001). **I** Heatmaps and volcano plots showing AT1 and AT2 signature gene expressions in FACS-isolated RFP-labelled AT1 and AT2 cells from control lungs (pooled from n=7 samples). Gene-set tests confirm that isolated AT1 and AT2 cells are highly enriched in their canonical signature genes.

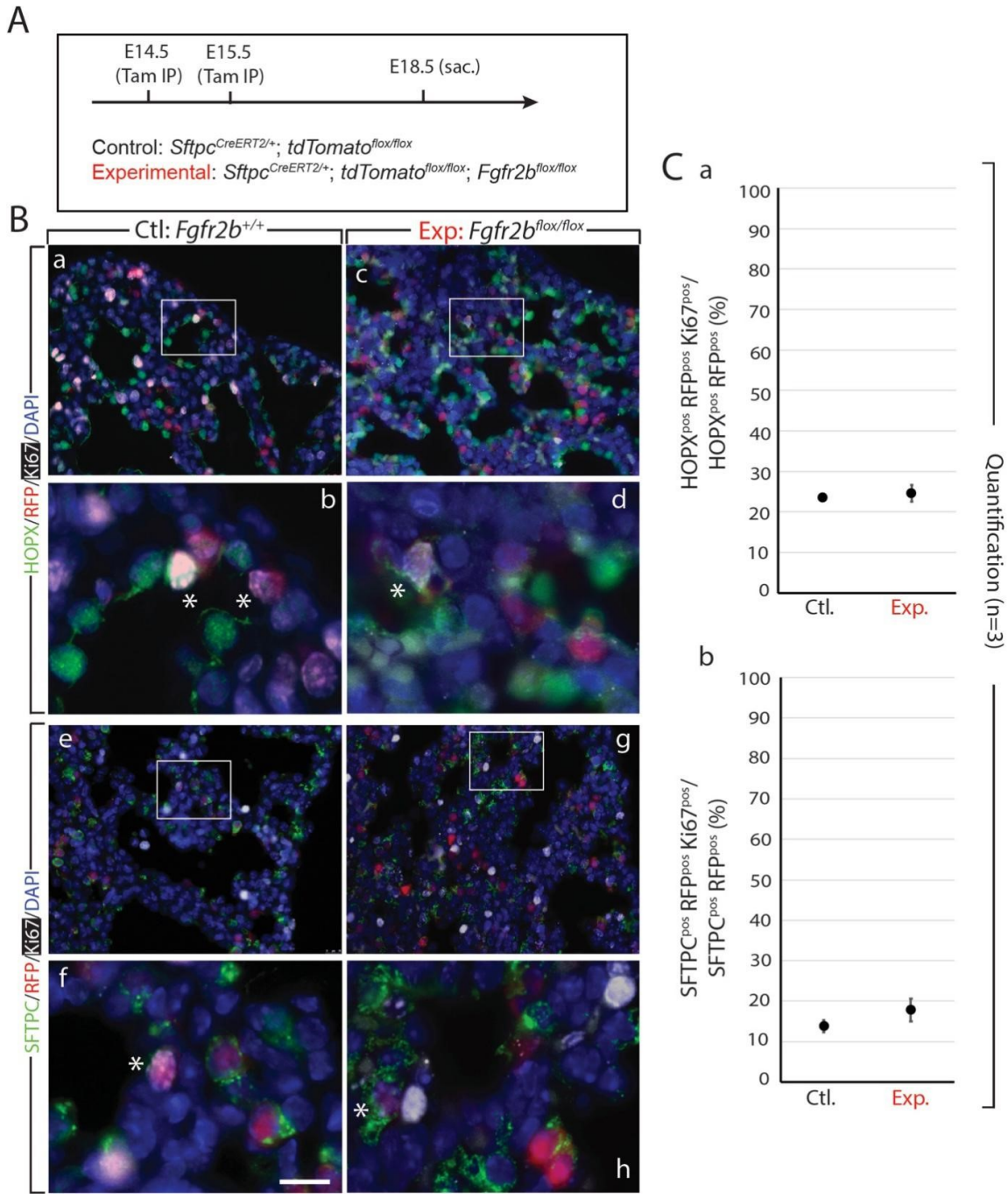

Figure S6 – Proliferation in RFP-labelled AT2 cells. (A) Experimental design. Timed-pregnant females carrying control and experimental animals were Tam-IP injected at E14.5 and at E15.5 and then sacrificed at E18.5. **(B)** Proliferation was assessed by labeling samples with Ki67. HOPX^{pos} (a-d) or SFTPC^{pos} (e-h) lineage-labelled RFP^{pos} Ki67^{pos} cells were manually quantified and divided by the total HOPX^{pos} or SFTPC^{pos} RFP^{pos} pool to determine the percentage of proliferating lineage-labelled alveolar cell. Asterisks depict triple positive cells (HOPX or SFTPC, RFP, and Ki67). *Scale bar:* (a, c, e, g) 30 µm, (b, d, f, h) 7.5 µm. **(C)** Graphs show no significant difference in proliferating lineage-labelled HOPX^{pos} cells (a) (control: 23.9% ± 0.28%; experimental: 25.92% ± 2.19%) or SFTPC^{pos} cells (b) (control: 13.62% ± 1.53%; experimental: 17.75% ± 2.82%) between control and experimental groups (n=3).

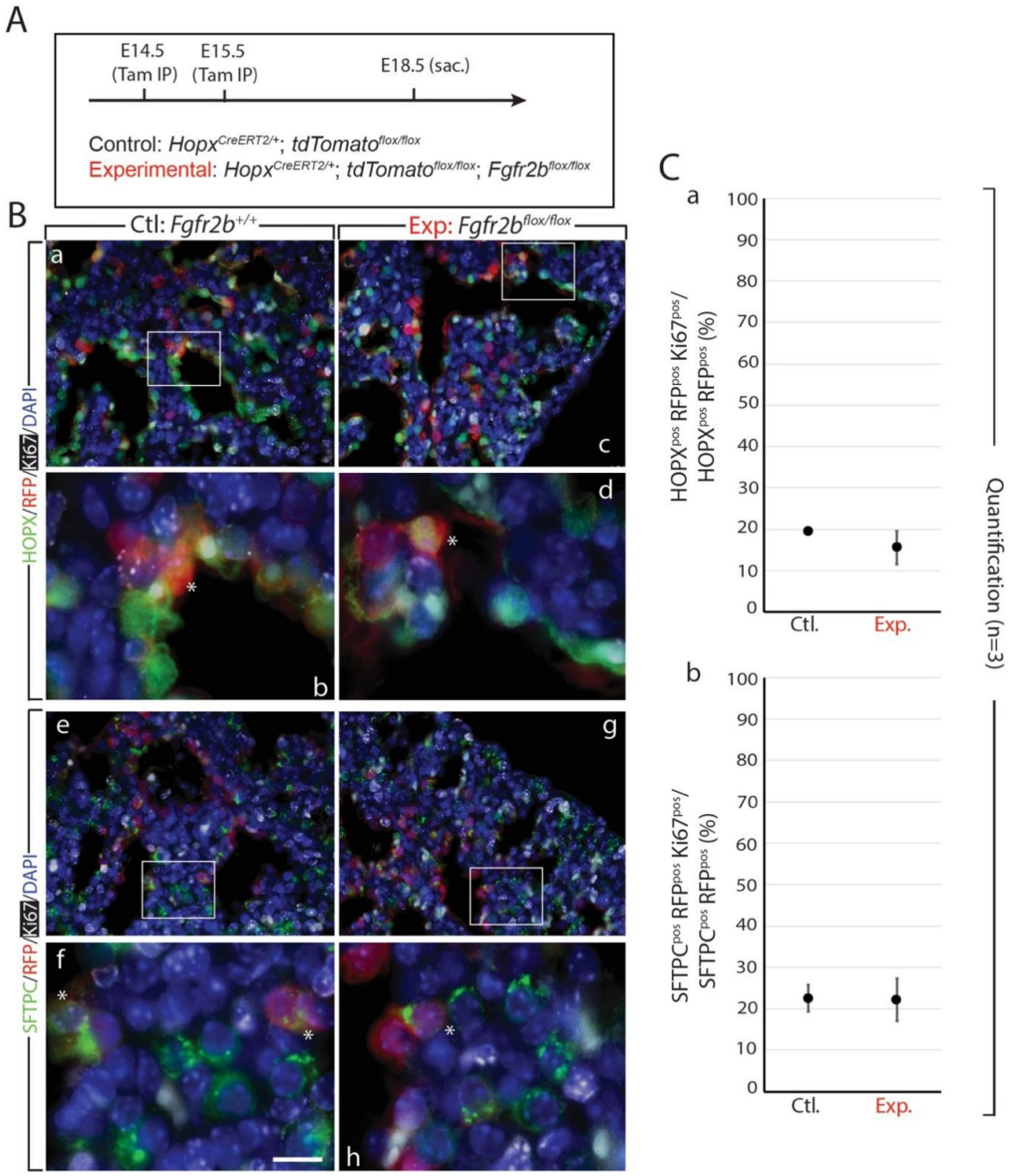

Figure S7 – Proliferation in RFP-labelled AT1 cells. (A) Experimental design. Timed-pregnant females carrying control and experimental animals were Tam-IP injected at E14.5 and at E15.5 and then sacrificed at E18.5. **(B)** Proliferation was assessed by labeling samples with Ki67. HOPX^{pos} (a-d) or SFTPC^{pos} (e-h) lineage-labelled RFP^{pos} Ki67^{pos} cells were manually quantified and divided by the total HOPX^{pos} or SFTPC^{pos} RFP^{pos} pool to quantify the percentage of proliferating lineage-labelled alveolar cell. Asterisks depict triple positive cells (HOPX or SFTPC, RFP, and Ki67). *Scale bar:* (a, c, e, g) 30 µm, (b, d, f, h) 7.5 µm. **(C)** Graphs show no significant difference in proliferating lineage-labelled HOPX^{pos} cells (a) (control: 19.96% ± 0.56%; experimental: 15.61% ± 3.95%) or SFTPC^{pos} cells (b) (control: 22.56% ± 3.21%; experimental: 22.16% ± 5.22%) between control and experimental groups (n=3).

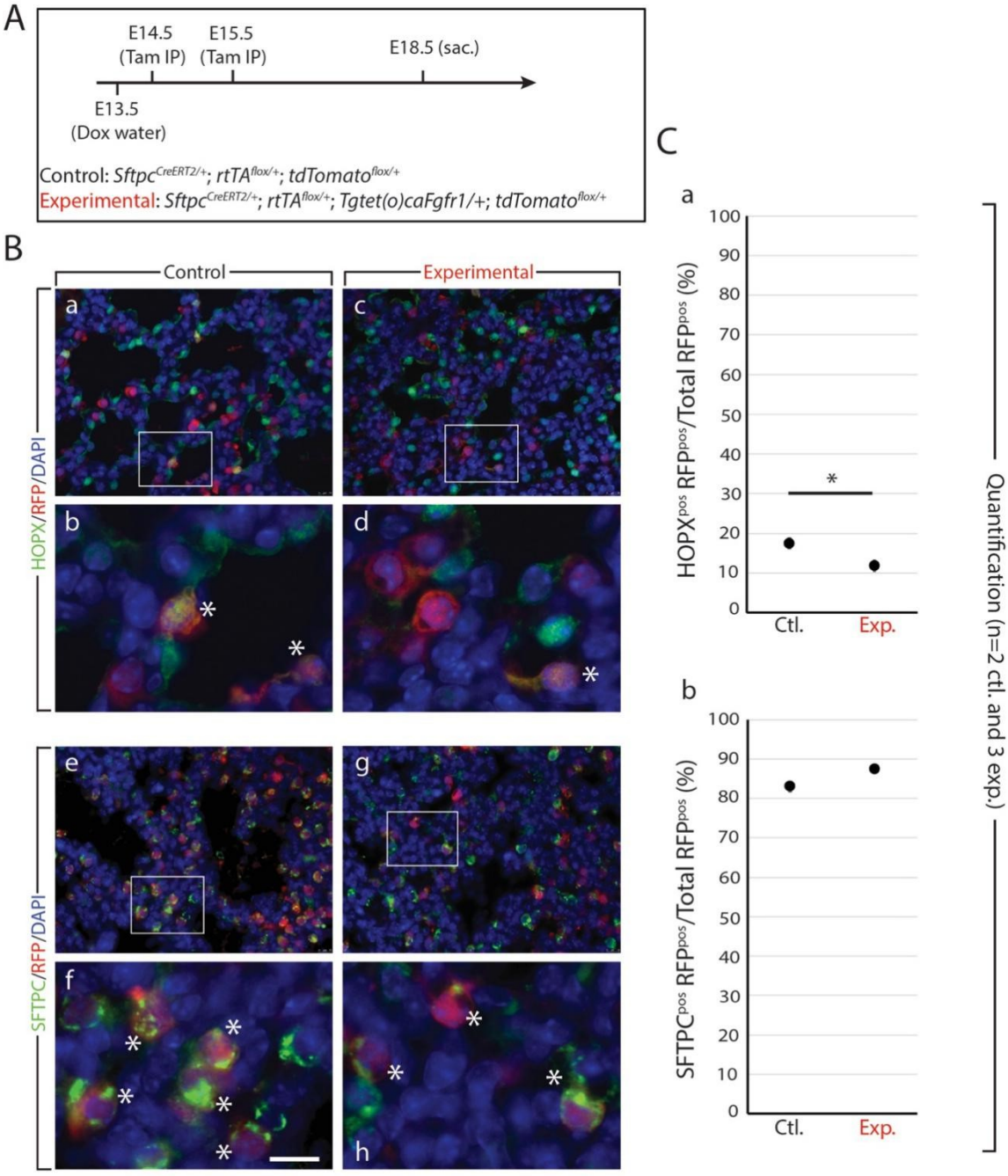

Figure S8 – Constitutive expression of FGFR1 in AT2 progenitors limits transition to AT1 cell fate. (A) Experimental design. Timed-pregnant females carrying control (*Sftpc*$^{CreERT2/+}$*; rtTA*$^{flox/+}$*; Tomato*$^{flox/+}$) and experimental (*Sftpc*$^{CreERT2/+}$*; rtTA*$^{flox/+}$*; Tg(tet(o)caFgfr1/+); Tomato*$^{flox/+}$) embryos were fed doxycycline water from E13.5 onward. At E14.5 and at E15.5, females were Tam-IP injected. After tamoxifen injection, Cre-based recombination of the floxed *TdTomato* reporter, as well as the floxed *rtTA*, was achieved in AT2 progenitor cells. In experimental embryos, rtTA/doxycycline induces the expression of a constitutively active form of *Fgfr1*, which, when expressed in alveolar epithelial cells, mimics the activity of FGFR2b signalling. Embryos were sacrificed and lungs harvested at E18.5. **(B)** Immunofluorescence staining of either AT1 cells (HOPX; panels a-d) or AT2 cells (SFTPC; panels e-h) in control (a, b and e, f) and experimental (c, d and g, h) lineage-labelled (RFP) samples. Asterisks indicate

double positive cells. *Scale bar:* 30 µm (a, c, e, g); 7.5 µm (b, d, f, h). **(C)** Quantification of samples from (B) (n=2 control and 3 experimental). (a) Graph showing the percentage of $HOPX^{pos}$ lineage-labelled RFP^{pos} cells over total RFP^{pos} cells. There is a significant decrease from around 17.5% ± 1.27% to 11.92% ± 1.31% in these cells after constitutive FGFR1 activity. (b) Graph showing a slight upward trend in the percentage of $SFTPC^{pos}$ lineage-labelled RFP^{pos} cells over the total of RFP^{pos} cells (control: 82.99% ± 1.27%; experimental: 87.36% ± 0.86%). (*p-value < 0.05).

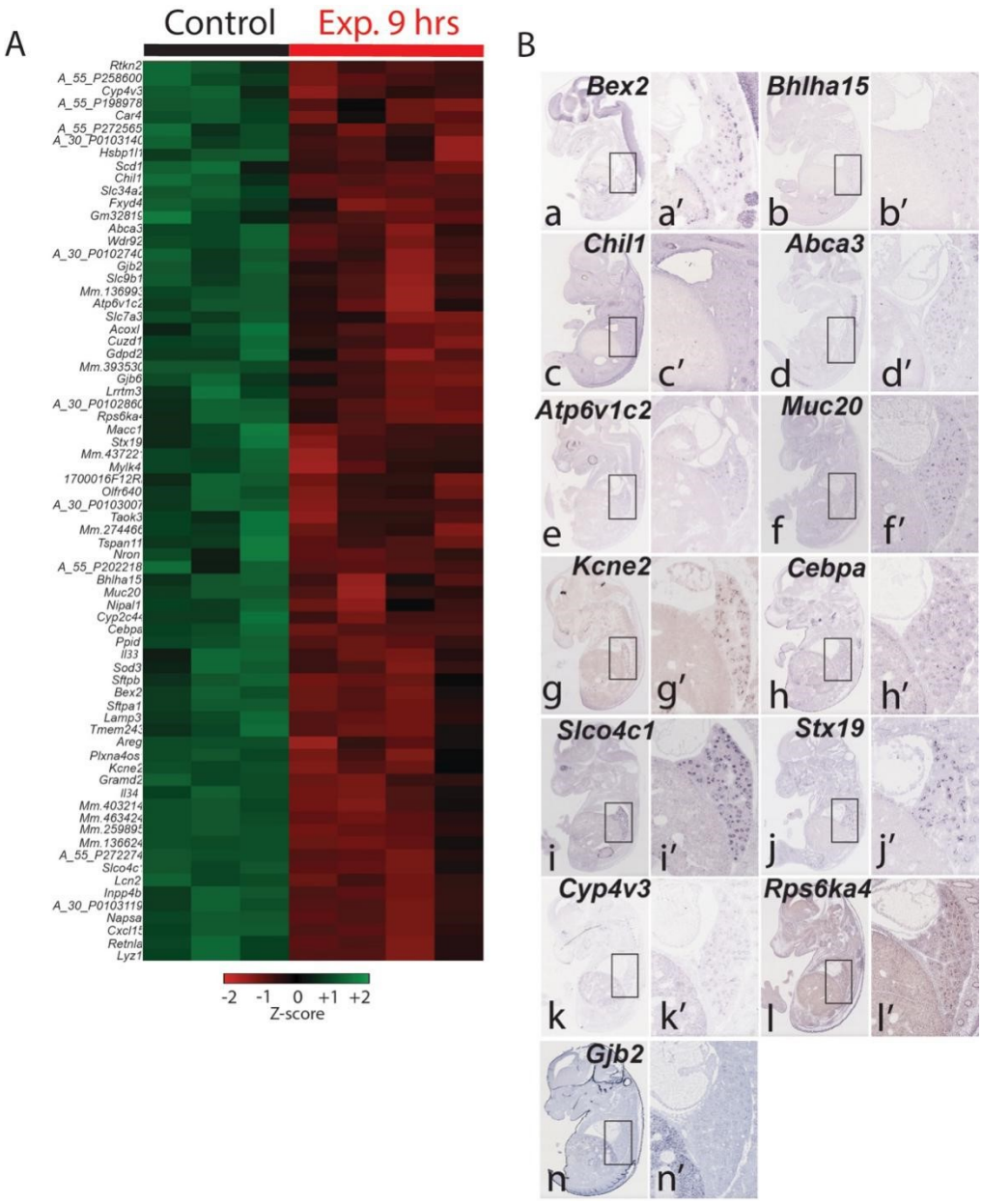

Figure S9 – FGFR2b signature genes at E16.5. (A) Heatmap, from Figure 1, showing the 72 downregulated genes after 9 hrs. FGFR2b ligand inhibition. These genes comprise the FGFR2b signature at this time-point. **(B)** Epithelial-specific *in situ* hybridization expression patterns from E14.5 embryonic sections retrieved from the Genepaint database (https://gp3.mpg.de/). Only a small number of the 72 regulated genes were found in the database, and of those only 13 showed clear epithelial expression patterns.

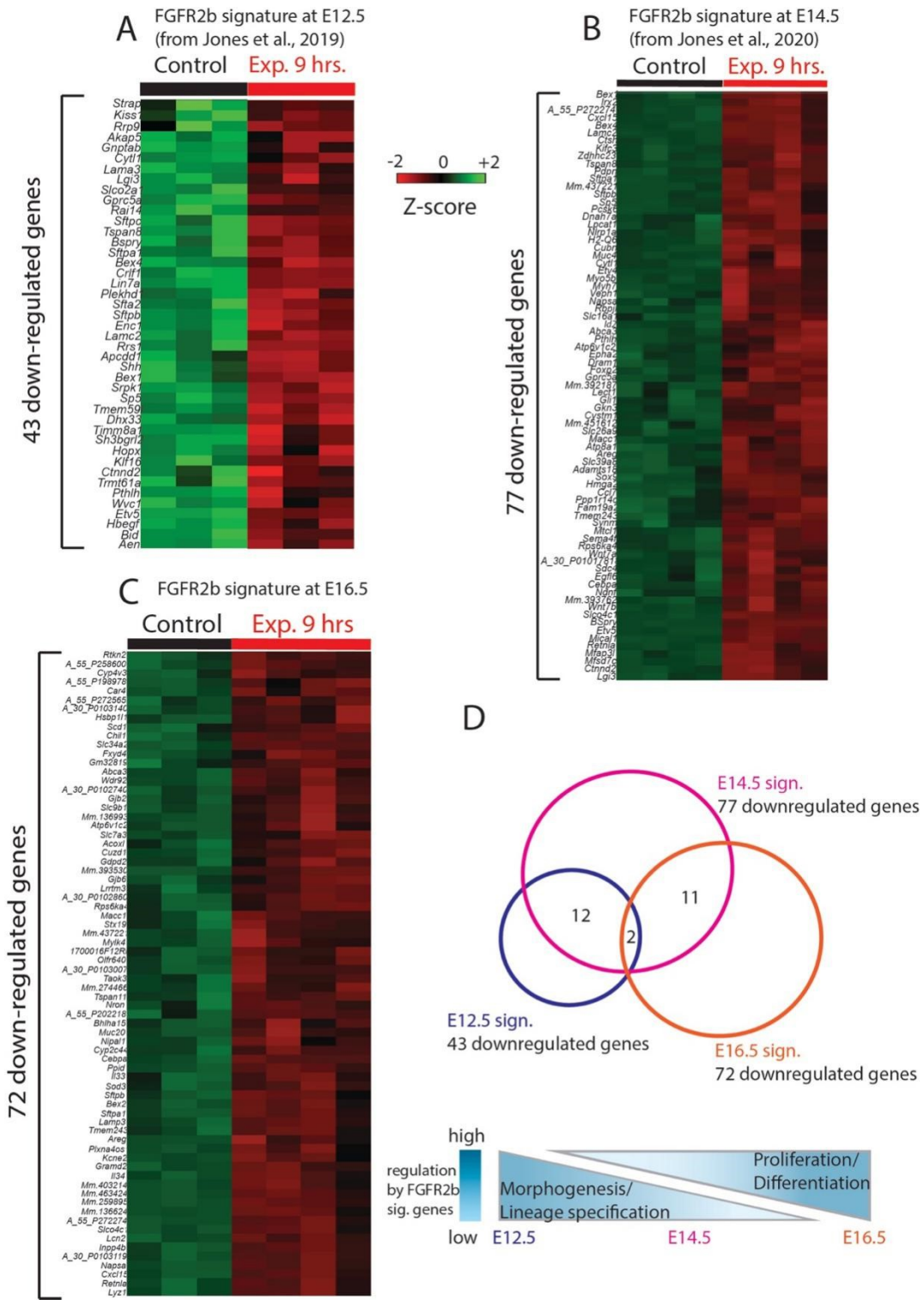

Figure S10 – Transcriptional targets of FGFR2b signalling during early and mid-pseudoglandular development. (A) Heatmap of the 43 downregulated genes at E12.5 after 9 hours FGFR2b ligands inhibition, constituting the E12.5 FGFR2b signature. **(B)** Heatmap of the 77 downregulated genes at E14.5 after 9 hours FGFR2b ligands inhibition, constituting the E14.5 FGFR2b signature. **(C)** Heatmap of the 72 downregulated genes at E16.5 after 9 hours FGFR2b ligands inhibition, constituting the E16.5 FGFR2b signature. **(D)** Venn diagram showing the shared genes among the three gene signatures. The E12.5 signature shares 12 genes with

the E14.5 signature. The E14.5 signature shares 11 genes with the E16.5 signature. Two genes (*Sftpa1* and *Sftpb*) are shared among the three signatures. These three signatures regulate shifting and overlapping biological activities over pseudoglandular development: branching morphogenesis and lineage specification which gives way to proliferation and differentiation later on.

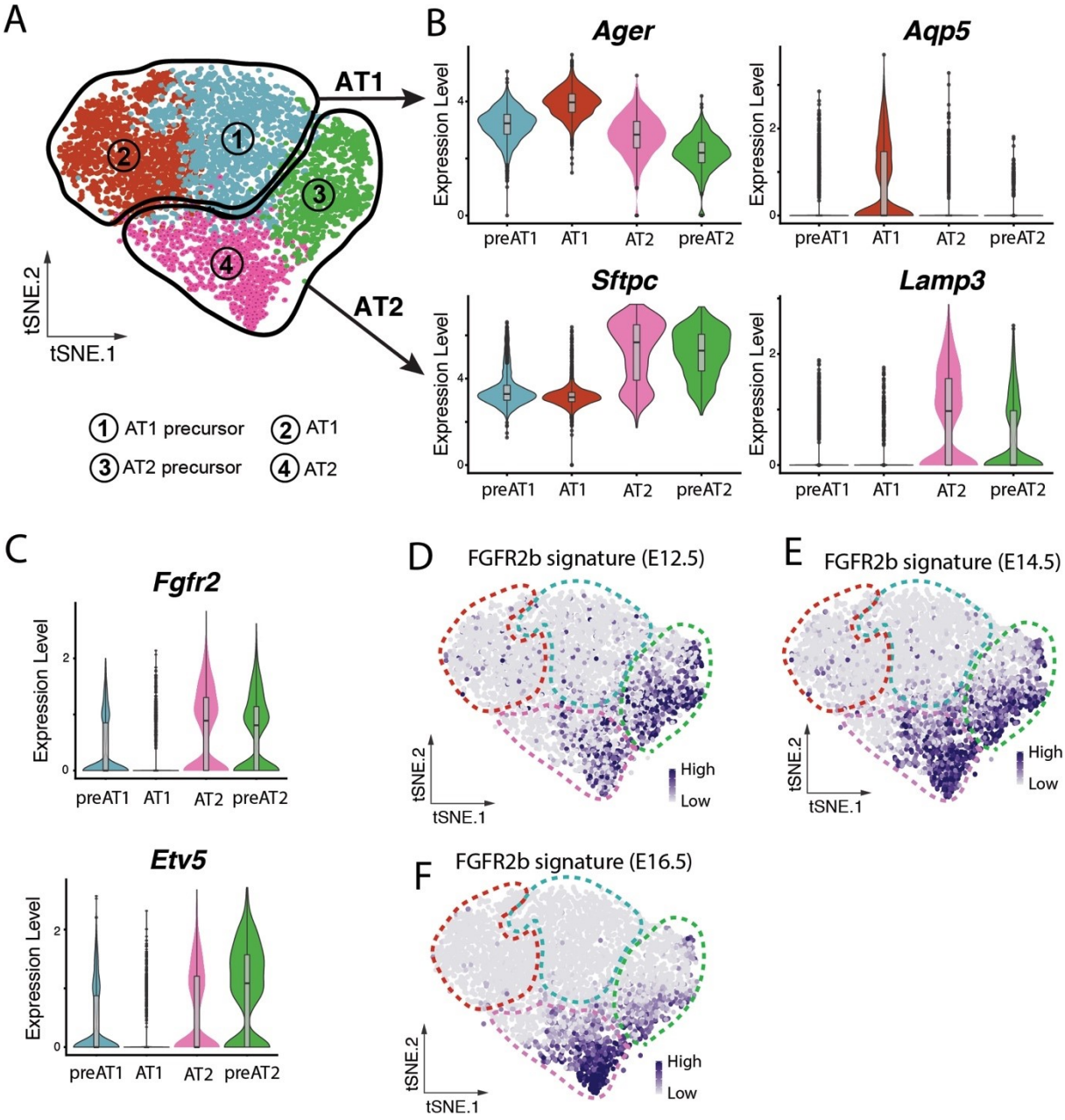

Figure S11 – Data-mining of scRNA-seq data from isolated E17.5 Nkx2-1-positive cells shows a narrowing of embryonic FGFR2b signatures to a subcluster of AT2 cells. (A) Four clusters reproduced from Frank et al. (2019) , GEO GSE113320: 1, blue – AT1 precursor; 2, red – mature AT1 cells; 3, green – AT2 precursor; 4, pink – mature AT2 cells. **(B)** Violin plots depict the expressions of AT2 (*Sftpc* and *Lamp3*) and AT1 markers (*Ager* and *Aqp5*) in the four clusters. **(C)** Violin plots of *Fgfr2* and the canonical downstream effector of FGFR2b signalling, *Etv5*, show that the two AT2 clusters, as well as to a lesser extent the AT1 precursors, show expression of these genes. **(D-G)** Reorientation of the four clusters from 'A' for ease of analysis. Expressions of FGFR2b signature genes at E12.5 I, E14.5 (F), and E16.5 (G) reveal a narrowing of FGFR2b responsive cells to a subcluster of mature AT2 cells (cluster 4) and AT2 precursors (cluster 3).

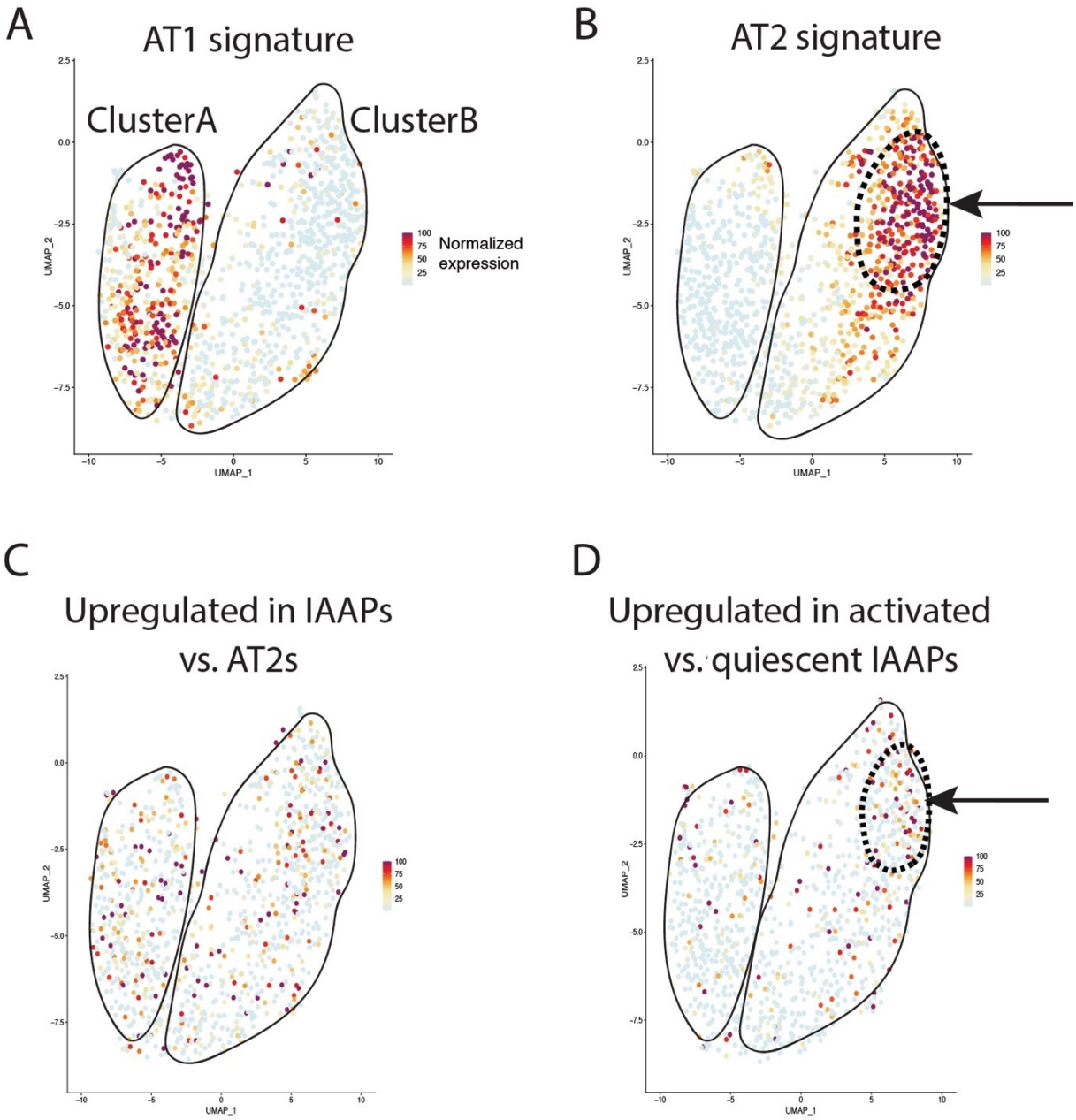

Figure S12 – Gene signatures delimit subclusters within mature AT2s. Subclustering of the mature AT2 cluster from Frank et al. (Frank et al., 2019) reveals two subclusters, A and B. **(A)** AT1 signature genes are expressed almost exclusively by cluster A cells. **(B)** AT2 signature genes concentrate in a portion of cluster B cells (arrow and hashed line). **(C)** Genes upregulated in IAAPs compared to mature AT2 cells as provided by Ahmadvand et al. (2021) are scattered throughout both clusters in our analysis. **(D)** Genes upregulated in activated IAAPs vs. quiescent IAAPs also scatter in both clusters, however, there seems to be a concentration of expression in a portion of cluster B, which overlaps with the cells expressing the AT2 signature (black arrows and hashed lines).

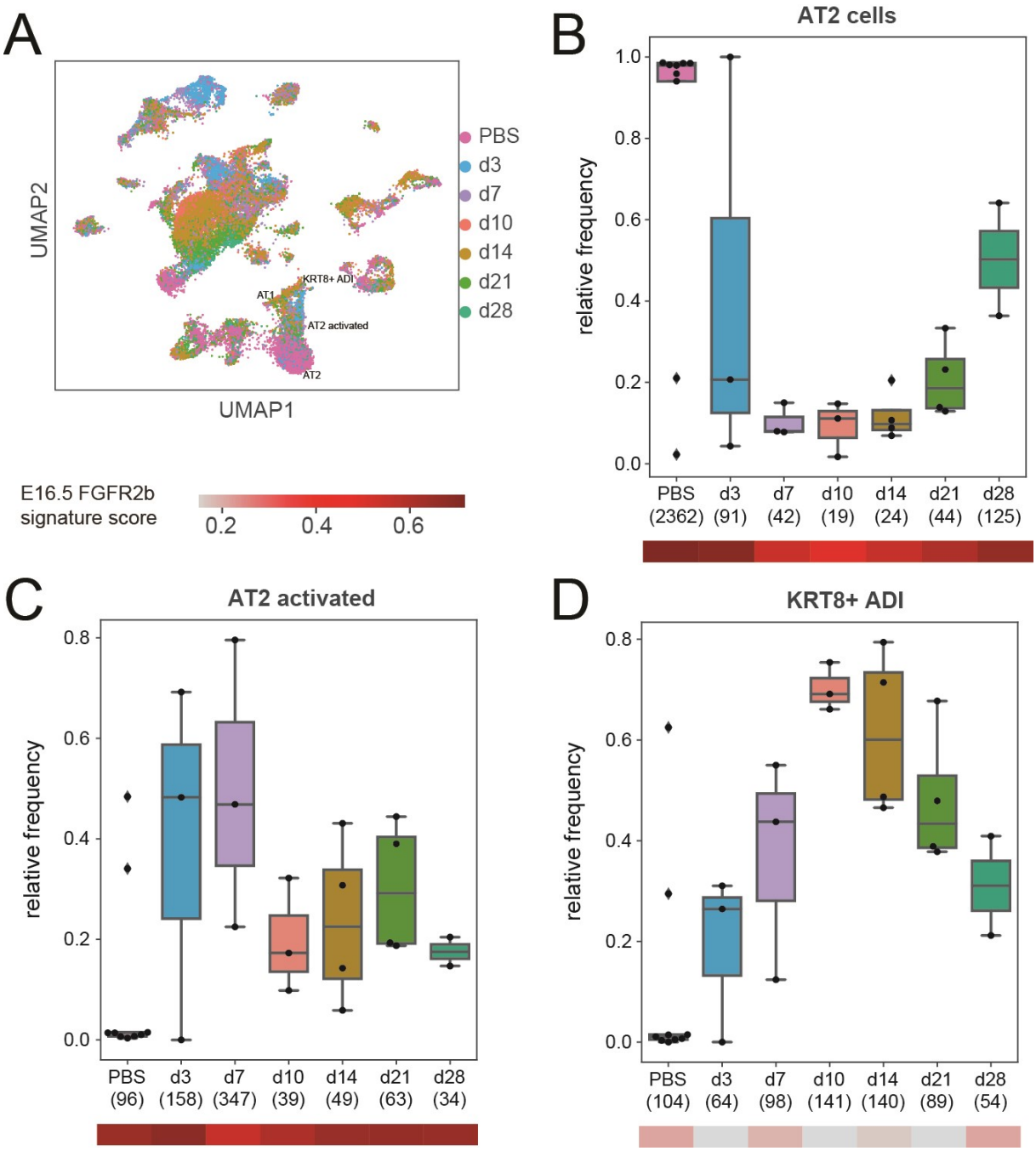

Figure S13 – The E16.5 FGFR2b signature is nearly lost in KRT8+ ADI cells during repair after bleomycin-induced lung injury. (A) UMAP showing the single-cell data set from Strunz et al. (2020), with the alveolar lineage labelled (AT2, AT2 activated, KRT8+ ADI, and AT1 populations). **(B-D)** Box and whisker plots showing the frequency of each cell type (B: AT2 cells; C: AT2 activated cells; D: KRT8+ ADI cells) relative to the entire alveolar cell population over time. Numbers In brackets represent absolute cell numbers. Heatmaps show the expression scores of the E16.5 FGFR2b signature for each cell type at each timepoint.

11 Acknowledgements

To my parents, you were always there for me. You were my lifeline in so many ways. Mom, I am sorry you didn't live to see me graduate. I know you would be proud.

To my children, Enan and Anyo, your crazy dad is growing up. Sorry for the stress! Commit to openness and honesty, with yourself and with others, and good things will happen. I love you both more than you can imagine.

To my partner in this rollercoaster adventure, Ilka. You stabilize me. You challenge me. You inspire me. Thank you for sharing your heart with me.

To each member of the lab, past and present, you have been like family to me. Each one of you has had a positive impact on my life. I would like to especially thank Kerstin and Saverio. You brought me in, gave me a second home and a wonderful chance, and you have both always shown heroic patience and understanding with a difficult personality! I wish to thank Heike and Negah, as well. Along with Kerstin and Saverio, you both were always there to listen and discuss as I navigated through many tough times. To each of you, time and again your professional and personal guidance provided a much-needed compass when I was lost.

I am blessed to have so many loving and supportive people in my life. I couldn't have taken this journey without any of you. Thank you!